

# Design of Stable and Broadband Remote Vibration Controllers



The  
University  
Of  
Sheffield.

Ubaid Ubaid

Department of Automatic Control and Systems Engineering

University of Sheffield

A thesis submitted for the degree of

*Doctor of Philosophy*

February 2013

---

## **Abstract**

The majority of active vibration control problems are tackled by mounting sensors and actuators at the location where vibration attenuation is desired. But for some special vibration attenuation problems, the constraint due to space and weight prohibit positioning of sensors and actuators at these points. This necessitates development of control design methods that overcomes these stringent limitations. One such method makes use of remotely located sensor actuator pair to counteract the problematic excitation. A novel control design methodology based on a geometric approach for remotely located sensor actuator pair had previously been developed to address this issue. It was experimentally tested to attenuate vibration for a harmonic or tonal excitation. It gives better physical insight as compared to alternative control design techniques. The final compensator implementation for controlling vibration due to broadband excitation involves model inversion of the local control path dynamics. So, the controller itself is unstable if the local control path is non-minimum phase. Although collocated sensor and control actuator pair can be employed here, it is difficult to avoid non-minimum phase transfer function due to non-ideal practical conditions. A stable controller design using a similar geometric approach is developed in this work such that even if the local control path transfer function is non-minimum phase, the controller will be stable.

A solution is provided by means of a modified design procedure which is necessary but not sufficient for the final controller to be stable and stabilising. The sufficiency conditions for stability of controller are presented in terms of the new design freedom parameter. Furthermore, robustness to unmodelled high frequency dynamics is taken into account as part of the modified design procedure. The controller implementation using the

modified approach enjoys the advantage of robustness to control spillover at unmodelled high frequencies without deteriorating the performance in the disturbance frequency bandwidth. The applicability of this method to address spatially global reduction requirements is also investigated. A sequential loop closing control design for multiple local feedback loops is also shown using this design for each individual control loops.

## **Acknowledgements**

At the outset, I would like to sincerely thank Professor Steve Daley for giving me the opportunity to pursue this PhD. I benefitted immensely from the discussions during the time spent working with him. I am also very indebted to him for all the provisions of the experimental work that he arranged.

I would also like to thank Dr. Simon Pope for his guidance and constructive feedback of my work, which has been very useful to further improve it. His supervisory support has made the PhD experience a pleasant and smooth one.

I would also like to thank Dr. Ilias Zazas for assisting me with setting up and running the experiments in the laboratory. His words of encouragement during the difficult experimentation period is appreciated. Also, Dr. Donald Nyawako's assistance with the civil side of experiments is gratefully acknowledged. I would also like to thank Michael Pelegrinis for the nice conversations in the office.

# Contents

<b>Contents</b>	<b>iv</b>
<b>List of Figures</b>	<b>vii</b>
<b>List of Tables</b>	<b>xiv</b>
<b>1 Introduction</b>	<b>1</b>
1.1 Brief review of active control . . . . .	2
1.2 Motivation . . . . .	5
1.2.1 Some examples . . . . .	6
1.3 Description of problem . . . . .	8
1.4 Achievements . . . . .	11
1.5 Outline of thesis and contribution . . . . .	12
<b>2 Remote Vibration Control Design Using Geometric Approach</b>	<b>17</b>
2.1 Introduction . . . . .	17
2.2 Preliminary design procedure . . . . .	19
2.3 Practical Considerations . . . . .	24
2.3.1 Time Delay and Phase Lag . . . . .	25
2.3.2 Unstable Controller - Testing and Implementation . . . . .	28
2.4 Summary . . . . .	30
<b>3 Design of Strongly Stabilising Controllers</b>	<b>31</b>
3.1 Introduction . . . . .	31
3.2 Design of Stable and Broadband Controller . . . . .	32
3.3 Robust Performance . . . . .	35

3.3.1	Control Spillover and Observation Spillover . . . . .	35
3.3.2	Control Design for Robust Performance . . . . .	36
3.4	Stability Analysis . . . . .	39
3.5	Numerical example . . . . .	42
3.5.1	Model of beam . . . . .	42
3.5.2	Selection of optimal $\gamma$ . . . . .	43
3.5.3	Interpolation of $\gamma$ values . . . . .	44
3.5.3.1	Reduced interpolation data set . . . . .	46
3.5.3.2	Modification of $\gamma_i$ to satisfy controller stability . . . . .	47
3.5.4	Controller Implementation . . . . .	47
3.5.5	Alternative Controller Implementation . . . . .	51
3.6	Summary . . . . .	54
<b>4</b>	<b>Remote Vibration Attenuation at a Non-resonating Point</b>	<b>57</b>
4.1	Introduction . . . . .	57
4.2	Experimental set-up . . . . .	58
4.3	Description using Relative Gain Array . . . . .	60
4.4	Control design . . . . .	63
4.4.1	Interpolation of optimal $\gamma$ data values . . . . .	65
4.5	Experimental implementation . . . . .	67
4.5.1	Sinusoidal excitation of frequency 247 Hz . . . . .	67
4.5.2	Reduction of peak in controller FRF . . . . .	69
4.5.3	Broad frequency band random excitation . . . . .	72
4.6	Summary . . . . .	72
<b>5</b>	<b>Active Damping at Resonance</b>	<b>74</b>
5.1	Introduction . . . . .	74
5.2	Active Damping . . . . .	75
5.3	Design parameter at resonance . . . . .	76
5.4	Active damping of a beam structure . . . . .	79
5.4.1	Experimental set-up . . . . .	80
5.4.2	Control design . . . . .	81
5.4.3	Interpolation of optimal $\gamma$ data values . . . . .	85

5.4.4	Experimental results . . . . .	87
5.5	Summary . . . . .	91
<b>6</b>	<b>Global Vibration Reduction</b>	<b>93</b>
6.1	Introduction . . . . .	93
6.2	Design parameter for direct velocity feedback control . . . . .	95
6.3	Control design for kinetic energy reduction . . . . .	96
6.4	Summary . . . . .	100
<b>7</b>	<b>Sequential Loop Closing Control Design</b>	<b>101</b>
7.1	Introduction . . . . .	101
7.2	Sequential Loop Closing Control Design . . . . .	102
7.2.1	Control system design for the first loop . . . . .	103
7.2.2	Control system design for the second feedback loop . . . . .	106
7.2.3	Integrity when inner feedback loop fails . . . . .	108
7.3	Summary . . . . .	114
<b>8</b>	<b>Experimental Verification of Sequential Loop Closing Control Design</b>	<b>116</b>
8.1	Introduction . . . . .	116
8.2	Experimental Implementation . . . . .	117
8.2.1	Selection of suitable measurement and performance test points . . . . .	117
8.2.2	Control Design for first feedback loop at TP19 . . . . .	118
8.2.3	Control Design for second feedback loop at TP10 . . . . .	122
8.2.4	Experimental Results . . . . .	126
8.3	Summary . . . . .	131
<b>9</b>	<b>Conclusions</b>	<b>132</b>
9.1	Contributions . . . . .	134
9.2	Scope for further work . . . . .	135
<b>Appendix A</b>		<b>140</b>
<b>Appendix B</b>		<b>142</b>
<b>References</b>		<b>144</b>

# List of Figures

1.1	Vibration due to unsteady force loading on a propeller blade . . . . .	6
1.2	Linear Fractional Transformation representation of the remote vibration controller design problem. The controller is designed to minimise the level of the performance output based on feedback of measurement output	10
2.1	Circles in $\alpha$ -plane for discrete frequencies which signify reduction in output at local (dashed) and remote (solid) points, and their centres which denote maximum attenuation at the local ( $\diamond$ ) and remote ( $\star$ ) points	21
2.2	The sensor and actuator dynamics included in the open loop transfer function . . . . .	26
2.3	(a) Nyquist diagram of open loop system for nominal gain (blue dashed) encircles the critical point and is closed loop stable if the controller itself is unstable but as the dc gain reduces below 60% nominal value (green solid) the closed loop system becomes unstable as is seen in the corresponding (b) time response of closed loop simulation outputs for nominal gain (blue) and 60% of it (green) . . . . .	29
3.1	The constraint regions for discrete frequencies in $\gamma$ -plane which signify reduction in output at local (dashed) and remote (solid) points and their centres that represent maximum attenuation at local ( $\diamond$ ) and remote ( $\star$ ) points . . . . .	34
3.2	Feedback system with multiplicative uncertainty . . . . .	37
3.3	Circles representing reduction in vibration at the local (blue) and remote (red) points on the beam, $U_c(j\omega_i)$ - $\diamond$ , $U_p(j\omega_i)$ - $\star$ . . . . .	44
3.4	Variation in $\kappa$ for different cut on and cut off frequencies of $W_\gamma(s)$ . . . . .	48

3.5	Initial set of optimal selected $\gamma$ values ( $\circ$ ), set of $\gamma$ values used for interpolation ( $\star$ ), operating $\gamma$ values shown as $\diamond$ is the frequency response of identified $\gamma(j\omega)$ , which is interpolated using a value of $\sigma = 50$ . . . . .	49
3.6	Nyquist diagram of $\gamma(j\omega)B_{cc}(j\omega)W_{\gamma}(j\omega)$ for $\gamma(j\omega)$ interpolated using a value of $\sigma = 50$ . . . . .	50
3.7	Nyquist plot of $\gamma(s)B_{cc}(s)W_{\gamma}(s)$ for $\gamma(j\omega)$ interpolated using a value of $\sigma = 6.5$ , also shown are the values of $\gamma(j\omega_i)B_{cc}(j\omega_i)W_{\gamma}(j\omega_i)$ corresponding to the initial set of optimal selected $\gamma$ values ( $\circ$ ) and its reduced set used for interpolation ( $\square$ ) . . . . .	50
3.8	Nyquist plot of $\gamma(s)B_{cc}(s)W_{\gamma}(s)$ for $\gamma(j\omega)$ interpolated from the modified set of $\gamma$ data values using a value of $\sigma = 6.5$ and $M = 1.54$ , also shown are the values of $\gamma(j\omega_i)B_{cc}(j\omega_i)W_{\gamma}(j\omega_i)$ corresponding to the initial set of optimal selected $\gamma$ values ( $\circ$ ), modified set of $\gamma$ values ( $\star$ ) and its reduced set used for interpolation ( $\square$ ) . . . . .	51
3.9	Initial set of optimal selected $\gamma$ values ( $\circ$ ), modified set of $\gamma$ values ( $+$ ), set of $\gamma$ values used for interpolation ( $\star$ ), final operating $\gamma$ values shown as $\diamond$ is the frequency response of identified $\gamma(j\omega)$ , which is interpolated using a value of $\sigma = 6.5$ and $M = 1.54$ . . . . .	52
3.10	Magnitude FRF of primary disturbance input to local sensor with (solid) and without (dashed) feedback control . . . . .	53
3.11	Magnitude FRF of primary disturbance input to remote output with (solid) and without (dashed) feedback control . . . . .	53
3.12	Magnitude FRF of controller, $ k(j\omega) $ . . . . .	54
3.13	Magnitude FRF of primary disturbance input to local sensor with (solid) and without (dashed) feedback control, $\hat{k}(j\omega)$ . . . . .	55
3.14	Magnitude FRF of primary disturbance input to remote output with (solid) and without (dashed) feedback control, $\hat{k}(j\omega)$ . . . . .	55
3.15	Magnitude FRF of controller, $ \hat{k}(j\omega) $ . . . . .	56
4.1	Top view of the experimental facility . . . . .	58
4.2	Magnitude frequency response of primary excitation input to (a) thrust block vibration output and (b) blade vibration output . . . . .	60

## LIST OF FIGURES

---

4.3	Magnitude and phase frequency response of the local control path from control shaker input to thrust block accelerometer measurements (solid) and an identified model (dashed) . . . . .	63
4.4	Portrayal of constraint regions in $\gamma$ -plane that denote attenuation in blade vibration for discrete frequencies between 200 Hz and 300 Hz. Unit radius circles corresponding to reduction of vibration at the thrust block appear as a cylinder passing through the origin . . . . .	64
4.5	The reduction in vibration at the thrust block ( $\circ$ ) and blade end portrayed as regions inside circles in $\gamma$ -plane. The frequency response of the interpolated $\gamma(j\omega)$ ( $\square$ ) and the optimal selected values for interpolation ( $\odot$ ) . . . . .	66
4.6	Magnitude frequency spectrum of the synthesized controller . . . . .	67
4.7	Power spectral density of accelerometer output on thrust block when disturbance shakers on the blade are excited by a sinusoidal of 247 Hz . . . . .	68
4.8	Power spectral density of the summation of accelerometer outputs on blade end when disturbance shakers on the blade are excited by a sinusoidal of 247 Hz . . . . .	68
4.9	Estimated magnitude frequency response of the path from primary excitation input to thrust block output with (solid) and without (dashed) feedback control . . . . .	69
4.10	Estimated magnitude frequency response of the path from primary excitation input to blade vibration output with (solid) and without (dashed) feedback control . . . . .	70
4.11	Power spectral density of accelerometer output on thrust block when disturbance shakers on the blade are excited by a sinusoidal of 247 Hz, and the controller is implemented in series with a notch filter . . . . .	71
4.12	Power spectral density of the summation of accelerometer outputs on blade end when disturbance shakers on the blade are excited by a sinusoidal of 247 Hz, and the controller is implemented in series with a notch filter . . . . .	71
4.13	Power spectral density of accelerometer output on thrust block when disturbance shakers on the blade are excited by a random white noise input, controller is implemented in series with a notch filter . . . . .	72

4.14	Power spectral density of the summation of accelerometer outputs on blade end when disturbance shakers on the blade are excited by a random white noise input, controller is implemented in series with a notch filter . . . . .	73
5.1	(a) the point frequency response plot showing a discrete frequency relative to the peak of resonant frequency highlighted by red dashed line and (b) the circles corresponding to reduction in output at 10 different locations on the beam for this discrete frequency . . . . .	78
5.2	(a) resonant frequency highlighted by red dashed line and (b) the circles corresponding to reduction in output at 10 different locations on the beam for this discrete frequency . . . . .	78
5.3	(a) a discrete frequency near the peak of resonant frequency and (b) the circles corresponding to reduction in output at 10 different locations on the beam for this discrete frequency . . . . .	79
5.4	Experimental test rig consists of a beam mounted on passive mounts . . .	81
5.5	Schematic illustration of the experimental set-up . . . . .	82
5.6	Magnitude frequency response of output (a) on top of the beam and (b) at the base of beam near the mounts, for disturbance excitation input . . .	83
5.7	Magnitude and phase frequency response of output on top of the beam and control input plotted using data from measurements (solid) and an identified model (dashed) . . . . .	83
5.8	Portrayal of vibration attenuation at the local (blue) and remote (red) points as circles in $\gamma$ -plane and its centres ( $\square$ and $\star$ , respectively) which denote maximum attenuation at the respective points . . . . .	84
5.9	Portrayal of vibration attenuation at the local (blue) and remote (red) points as circles in $\gamma$ -plane, initial set of optimal $\gamma$ values ( $\circ$ ) and $\gamma$ values used for interpolation after modification ( $\star$ ). The set of final operating $\gamma$ values shown as $\diamond$ is the frequency response of identified $\gamma(s)$ which is interpolated using a value of $\sigma = 20$ and $M = 1$ . . . . .	86
5.10	Nyquist plot of $\gamma(s)B_{cc}(s)W_\gamma(s)$ interpolated using a value of $\sigma = 20$ , also shown are the values of $\gamma(j\omega_i)B_{cc}(j\omega_i)W_\gamma(j\omega_i)$ corresponding to the initial set of selected $\gamma$ values ( $\circ$ ) and the final operating $\gamma$ values ( $\square$ )	86

**LIST OF FIGURES**

---

5.11	Magnitude frequency response of the designed controller . . . . .	87
5.12	Theoretical estimation of the magnitude of the frequency response from primary excitation input to local output with (solid) and without (dashed) feedback control . . . . .	88
5.13	Theoretical estimation of the magnitude of the frequency response from primary excitation input to remote output with (solid) and without (dashed) feedback control . . . . .	89
5.14	Power spectral density of the output on top of the beam for a sinusoidal excitation input with (solid) and without (dashed) feedback control . . .	89
5.15	Power spectral density of the output at the base of the beam for a sinusoidal excitation input with (solid) and without (dashed) feedback control	90
5.16	Power spectral density of the output on top of the beam for a random excitation input with (solid) and without (dashed) feedback control . . .	90
5.17	Power spectral density of the output at the base of the beam for a random excitation input with (solid) and without (dashed) feedback control . . .	91
6.1	Kinetic energy spectrum of the beam with no control (green dotted), direct velocity feedback control with maximum stable gain (blue dashed) and geometric based control design (solid red) . . . . .	98
6.2	Value of $\gamma$ that corresponds to minimum kinetic energy ( $\star$ ), the selected values for geometric control design ( $\diamond$ ) and the centre of circles for local vibration reduction ( $\circ$ ) plotted for (a) the first resonant frequency of 47 Hz and (b) second resonant frequency 187 Hz . . . . .	99
6.3	Value of $\gamma$ that corresponds to minimum kinetic energy ( $\star$ ), the selected values for geometric control design ( $\diamond$ ) and the centre of circles for local vibration reduction ( $\circ$ ) plotted for the frequency of (a) the first complex zeros 95 Hz and (b) the second zeros 316 Hz . . . . .	99
7.1	The perpendicular bisector in $\gamma_{a_1}$ -plane for $M_{b_2} = 1$ . . . . .	114
7.2	Circles for increasing value of $M_{b_2}$ in $\gamma_{a_1}$ -plane . . . . .	115

8.1	Schematic of the concrete slab showing location of excitation shakers ( $f_{p_1}$ and $f_{p_2}$ ) and control shakers ( $f_{c_1}$ and $f_{c_2}$ ) on the structure, acceleration is also measured at test point 6 (TP06) for remote performance evaluation . . . . .	118
8.2	View of the laboratory set-up from one end . . . . .	119
8.3	Control Shaker, piezo-electric Endevco accelerometer used to capture shaker dynamics, and QA accelerometer used for feedback measurement	120
8.4	Magnitude and Phase of the actuator dynamics . . . . .	120
8.5	Magnitude of the FRF between the acceleration output at TP06, TP02, TP19 and the primary excitation at TP02 . . . . .	121
8.6	Magnitude of the FRF between the acceleration output at TP06, TP11, TP10 and the primary excitation at TP11 . . . . .	121
8.7	Regions in $\gamma_a$ -plane in the design frequency band describing the reduction in output at TP06 (centre of circle $\circ$ ), TP02 (centre of circle $\star$ ) and TP19 (centre of circle $\square$ ) . . . . .	123
8.8	Comparison of the predicted magnitude of FRF between output at TP06 and disturbance excitation at TP02, with and without (dashed) feedback control at TP19 . . . . .	123
8.9	Comparison of the predicted magnitude of FRF between output at TP02 and disturbance excitation at TP02, with and without (dashed) feedback control at TP19 . . . . .	124
8.10	Comparison of the predicted magnitude of FRF between output at TP19 and disturbance excitation at TP02, with and without (dashed) feedback control at TP19 . . . . .	124
8.11	Regions in $\gamma_{b_2}$ -plane in the frequency band near first natural frequency describing the reduction in output at TP06 (centre $\star$ ), TP11 (centre $\circ$ ) and TP10 (centre $\square$ ) . . . . .	126
8.12	Regions in $\gamma_{b_2}$ -plane in the frequency band near second natural frequency describing the reduction in output at TP06 (centre $\star$ ), TP11 (centre $\circ$ ) and TP10 (centre $\square$ ) . . . . .	127
8.13	Nyquist plot of the term (7.30) which determines robustness of second loop when inner loop fails . . . . .	128

- 8.14 Power spectral density of the output at TP06, open loop (thick shaded), partial closed loop with control action at only TP19 (dotted) and only TP10 (dashed), and both loops closed (thin solid) . . . . . 129
- 8.15 Power spectral density of the output at TP02, open loop (dotted), partial closed loop with control action at only TP19 (dash-dotted) and only TP10 (dashed), and both loops closed (solid) . . . . . 129
- 8.16 Power spectral density of the output at TP11, open loop (dotted), partial closed loop with control action at only TP19 (dash-dotted) and only TP10 (dashed), and both loops closed (solid) . . . . . 130
- 8.17 Power spectral density of the output at TP19, open loop (dotted), partial closed loop with control action at only TP19 (dash-dotted) and only TP10 (dashed), and both loops closed (solid) . . . . . 130
- 8.18 Power spectral density of the output at TP10, open loop (dotted), partial closed loop with control action at only TP19 (dash-dotted) and only TP10 (dashed), and both loops closed (solid) . . . . . 131
  
- 9.1 Flow chart showing the main steps of the geometric based control design 133
- 9.2 Flow chart showing the steps of the Nevanlinna Pick interpolation . . . 138

# List of Tables

3.1	Properties of the beam considered for simulation study in section 3.5	. 43
-----	---	------

# Chapter 1

## Introduction

The phenomenon of vibration as a consequence of moving parts and machinery in mechanical systems is undesirable since it causes wear and tear, thereby reducing operational life. It also adversely affects civil engineering structures and is uncomfortable for passengers on ships and aeroplanes. Passive methods have been used to alleviate some of such problems by adding mass or using dampers, absorbers and passive isolators [Mead and Meador, 1998; Motahari et al., 2007; Nakra, 1998; Rao, 2003]. But a major drawback of passive vibration control is that it is only effective at high frequencies and is sensitive to the exposed thermal environment. The weight of passive damping components and also the cost of overhauling structures to fit dampers makes passive methods unappealing for some applications. Advancement in actuator and sensor technologies together with faster signal processing capabilities makes active control an attractive proposition for sound and vibration problems. Several works have combined advanced control systems design for varied performance requirements with active noise and vibration control problems [Meirovitch, 1990; Preumont, 2002; Tokhi and Hossain, 1996].

The aim of Active Noise and Vibration Control (ANC/AVC) is to cancel out or minimise the noise or vibration output due to a primary excitation signal by the superposition of an externally applied control signal. There has been considerable advancement in the field of AVC/ANC for application in mechanical [Gawronski, 2004], aerospace [Viswamurthy and Ganguli, 2004], and civil engineering problems [Soong, 1988]. This is comprised of the development in sensor and actuator technologies along

with improved control design methods. The stringent constraints on weight and space in some applications necessitates development of smaller and lighter sensors and actuators with better operating bandwidth [Glazounov et al., 2000]. Unlike passive methods, AVC is dependent upon the uninterrupted supply of external power source. It is also not inherently stable which necessitates systematic design of control systems for AVC applications. Furthermore, superior performance can only be achieved using advanced control design with state-of-the-art transducers and instrumentation. Unfortunately, this does not justify the increased financial costs for many industrial applications.

### 1.1 Brief review of active control

The majority of AVC/ANC methods can be broadly grouped into feedback and feedforward architectures [Alkhatib and Golnaraghi, 2003]. The appeal of feedforward techniques especially for active noise control applications is due to its improved performance and ease of stability robustness. This is well suited for disturbance caused by excitations that are deterministic in nature such as harmonic and tonal excitations. It does not require an accurate model of the process and so is robust to uncertainties and error in model identification [Elliott, 1998]. However, major drawbacks of this method are that it does not ensure reduction in global response and is limited to a very narrow frequency band. A reference signal that is correlated with the primary disturbance signal is also necessary for such control paradigms. In order to track changes to the spatial distribution and frequency of the primary signal, the controller is usually made adaptive.

Adaptive feedforward control algorithms for active noise and vibration control have been extensively investigated in the literature, see for e.g. [Daley and Zazas, 2012; Elliott et al., 1987]. It has been utilised for practical applications, for example, the suppression of aeroplane interior noise [Borchers et al., 1992; Elliot et al., 1990; Johansson et al., 1999]. The filtered-x LMS algorithm, which is a type of adaptive feedforward control proposed in the early 80s [Burgess, 1981; Widrow and Stearns, 1985], updates the coefficients of an FIR filter to adapt it every sampling instant by an amount dictated using the least mean squares algorithm to achieve noise mitigation. A similar algorithm causing adjustments to the coefficients of an IIR filter is termed as filtered-u LMS algorithm [Eriksson et al., 1987]. However, the convergence rate of FxLMS and FuLMS algorithm is slow for broadband disturbances, such as those encountered during changes

in engine speed [Inoue et al., 2004]. For more academic research works on ANC based on feedforward control algorithms, readers are referred to [Kuo and Morgan, 1996; Nelson and Elliott, 1993].

Feedback control, on the other hand, is more suited when a reference signal is not readily available. Output feedback control involves sensing the vibration output and feeding it back to a controller which then drives an actuator to cancel or minimise the primary excitation. Unlike feedforward techniques, many feedback control methods can be employed to reduce random excitation perturbations. It has also been used in conjunction with feedforward control for active vibration control [Meurers and Veres, 2000]. The stability and performance analysis tools are well developed for feedback techniques and can be implemented using fixed parameter filters [Elliott, 2001; Hansen and Snyder, 1997]. However, the controllers are mostly designed off-line for pre-determined model of a plant. Hence, there is less possibility for adaptation to dynamical variations in the plant. In [Meurers et al., 2002], a feedback control design method for mitigation of discrete frequency excitations with a high degree of adaptability to dynamic changes in the plant is presented. Although it does not require a reference signal, vibration is attenuated only for predetermined discrete frequencies. Also, an initial model of the plant comprised of complex gains at those frequencies is required prior to implementation. The real time computation involves updating the control input instead of updating any filter coefficients for the controller, which renders it as a non-linear control algorithm.

The varied vibroacoustic attenuation requirements for many applications is considered using different cost functions as parameters to be minimised [Anthony and Elliott, 2000; Bardou et al., 1997; Nelson et al., 1985]. Basically, this performance is evaluated based on the magnitude of vibration output at the location of one or more error sensors. A typical example is the application of modern control theory tools such as  $\mathcal{H}_\infty$  and LQG design for vibration suppression [Bhattacharya et al., 2002]. However, the control of local outputs alone does not take into account the response of the whole structure for AVC. Active control of lightly damped structures in a narrow spatial region may lead to increased response away from the error sensor positions. Therefore, this requires a wide distribution of sensors which may not be sufficient to quantify global attenuation due to the response at the unmeasured locations. These type of new lightweight structures have recently become widespread in the construction of cars and aeroplanes due

to their improved strength and stiffness. This can cause discomfort to passengers due to an increase in sound transmission and radiation in the low to middle audio frequency spectrum [Gardonio, 2002].

Distributed sensors and actuators for decentralised control is another promising approach to tackle the global vibration response [Jiang and Li, 2010]. Direct velocity feedback for decentralised control usually finds favour due to its simplicity of implementation and better performance margins. The objective is often to reduce the radiation of noise from vibrating structures, such as flat panels. It so happens that particular modes contribute more effectively than others towards the overall sound radiation [Baumann et al., 1992]. This leads to an additional consideration instead of merely mitigating the global vibration response of the structure [Zilletti et al., 2012]. Active control of vibration with an aim to reduce the sound power radiated by the structure is termed as active structural acoustic control. Some of the limitations using direct velocity feedback for active control are discussed more extensively in chapter 6.

The control design in this thesis also makes comparison to other active damping methods, besides direct velocity feedback, within the objectives of remote vibration control. In state-space formulation for feedback control, the control gains are selected so as to assign the eigenvalues of the identified system to certain pre-desired closed loop values. Active damping methods achieve reduction in the amplitude at resonance by actively modifying the structural characteristics [Díaz and Gardonio, 2007]. It then becomes important to model the dynamics of the sensors and actuators accurately for stability and better performance margins [Paulitsch et al., 2006b]. Discussion on some of the active damping methods, that require knowledge of modal parameters, are more pertinent in chapter 5 to show the parameterisation of any control design close to resonance in terms of the formulated design freedom.

The sensor and actuator placement strategy also has a crucial role to play in the AVC/ANC success story. The location and quantity of sensors and actuators has performance implications for both global and local vibration reduction in many active sound and vibration control applications. These factors affect the design of any control system for desired vibration attenuation [Baek and Elliott, 2000]. It can be argued that the number and location of actuators and sensors in a practical system has to be analysed at the design stage to avoid excitation of harmful vibration away from error sensor location or increased energy at ‘non-descript’ frequencies. For instance, the location of the control

action on a beam and its position relative to the primary excitation affects the achievable kinetic energy reduction as is shown in [Engels and Elliott, 2008]. It is reported in [Nelson and Elliott, 1993] and [Johnson et al., 2003] that for effective control action, the actuators should be placed close to the source of the disturbance. It is also shown in the latter work that global vibration reduction performance can be greatly improved when more error sensors than actuators are used. When the same number of actuators and error sensors are used, deterioration away from the error sensors can limit global attenuation performance.

## 1.2 Motivation

Many of the active vibration control studies implicitly make the assumption that vibration reduction is desired at the output that is available for measurement. This is true for systems if the actuators and sensors can be mounted where vibration attenuation is desired. The requirement to reduce noise or vibration at specific points can then be achieved using active control systems designed by positioning sensors and actuators at the same location [Balas, 1979; Hong and Bernstein, 1998]. However, in many large and interconnected structures such as large machinery installation, the source of disturbance is not available for measurement or in some cases the sensitive component where vibration reduction is desired is not available for actuation due to practical limitations on sensor and actuator placement. Furthermore, in many cases a wide distribution of sensors and actuators is not a feasible option. The feasibility of positioning sensors or actuators locally is generally limited due to harsh environment, space constraints or cost limitations. In such circumstances, feedback control has to be employed at easily accessible locations and the performance of the closed loop system in such a case does not then simply correspond to the measurement at the error sensor location. Moreover, vibration attenuation at the error sensor location in some cases does not ensure reduction in global response of the structure. This is true for complex interconnected structure and also for disturbance loading from different sources that interact with each other. Also, the attenuation of vibration output at a point has the potential to enhance vibration output at other points through vibration transmission paths [Post and Silcox, 1990], thus leading to a deterioration in global performance. Therefore, there are application areas where a locally sub-optimal solution is necessary for global vibration reduction. Hence-

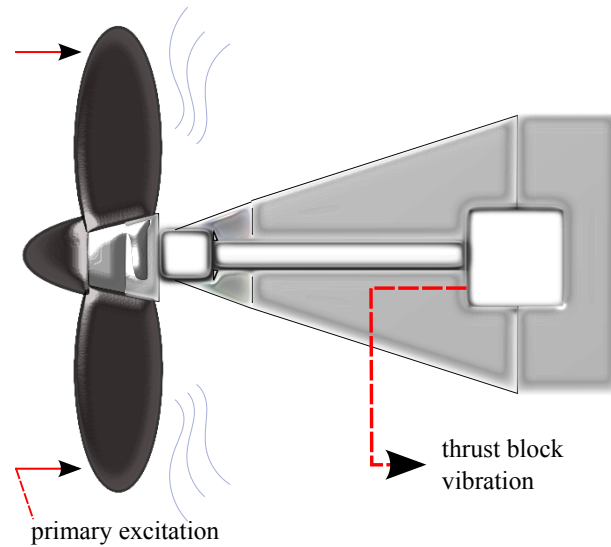


Figure 1.1: Vibration due to unsteady force loading on a propeller blade

forth in this thesis, the term *local point* or *local vibration* is used to refer to the location of error sensor and control actuator on the structure and the vibration measurement at this point, while *remote point* or *remote vibration* refers to any other location where disturbance excitation acts or where vibration reduction is desired.

### 1.2.1 Some examples

The generic nature of remote vibration control problem is illustrated with the help of few examples from the aerospace and maritime applications.

#### Rotary propulsion noise in aerospace

A typical example of such a problem is the vibration encountered due to aerodynamic loading on helicopter blades. The unsteady forces experienced by the rotor blades are generally transmitted at multiples of the blade passing frequency through the hub to the fuselage. This frequency depends on the rotational speed of the rotor multiplied by the number of blades. Although it is a discrete deterministic excitation of a particular frequency, the disturbance can be considered to sweep through a narrow frequency band as the speed of propeller rotor is increased initially from stationary position and

then consecutively run at different operating speeds. This can have detrimental effects such as passenger discomfort, increase in maintenance costs, lowering of component lifetime and limitations on maneuvering capabilities. Several experimental works have addressed the vibration problem due to helicopter rotor blades [Hall and Prechtel, 1999; Shaw et al., 1989].

Higher harmonic control uses swashplate oscillations to suppress the vibration force at the higher harmonics of rotor rotational speed. A swashplate is a mechanism that achieves flight command signals by changing the angle of the blades to which it is connected via control rods. In individual blade pitch control, sensors mounted on the blade feed information which is used to regulate the pitch of individual rotor blades. Traditionally, actuators are located at the swashplate or near the pitch links of the blades to act as close to the source of vibration as possible. Lately, with lighter actuator designs, there has been demonstrations using actuators that are mounted on the blades [Chopra, 2000]. These solutions are not cost effective and also suffer from limitations of small stroke which requires amplification [Giurgiutiu et al., 1997].

A related problem encountered in aerospace applications is concerned with the transmission and radiation of sound due to structure-borne noise. The vibration of working machinery causes excitation of low frequency structural resonances which radiates noise inside the aircraft cabin. Several control strategies actively dissipates the energy of these radiation modes by applying control force on the fuselage wall to reduce the interior noise, which is termed as active structural acoustic control [Fuller et al., 1992; Pearson et al., 1994; Simpson et al., 1991]. However, the control force applied on the fuselage does not take into account the vibration output on the rotor. It can lead to deterioration in global response due to the complex interactions between the different vibration loads on the hub [Nguyen, 1994]. A comprehensive review of passive and active approaches for aerospace vibro-acoustic control can be found in [Gardonio, 2002].

### **Propeller and machinery noise in marine vessels**

Equivalent problems in marine vessels occurs due to the oscillatory vibration caused by the propeller blades as they pass through a non-uniform wake velocity in the fluid field. The axial fluctuating forces generated by this vibration at the blade increases in amplitude at the resonant frequencies of the blades and it gets transmitted through the shaft to

the hull. The hull radiates noise very well which can generate acoustic noise leading to undesirable acoustic signature for naval and civil vessels. Besides the vibration caused by propulsion shafting systems, on-board machinery and equipment such as diesel engines are a major source of disturbance that propagates through the hull and radiates as structure borne noise in ships. One of its side effects is noise pollution that affects marine life and it also limits stealth capabilities of naval vessels. The raft supporting the working machinery is traditionally isolated using passive mounts to attenuate the transmissibility of forces to the hull [Crede, 1951]. However, due to resonances associated with structural components large forces are transmitted at these frequencies.

Active control methods which allows the machinery to be isolated from the hull by electromagnetically levitating the supporting raft received some attention from the defence and marine industry [Daley, 1998; Darbyshire and Kerry, 1997; Johnson and Swinbanks, 1996]. However, complete loss of vibration isolation during power failure is a major concern which motivated the development of active methods such as a hybrid active/passive solution [Daley et al., 2004, 2006, 2008]. Active control using magnetic levitation has also been reported for isolating precision instruments from microvibrations, which are critical for high resolution scanning applications and high-technology manufacturing at nanoscales [Hoque et al., 2010].

Figure 1.1 shows a pictorial representation of the fore and aft vibration along shaft connected to the propeller blades in ships. It gets transmitted to the hull through the thrust bearing which forms a rigid connection. Previous efforts focused on using passive methods to reduce the vibration transmission to the hull using a resonance changer [Dylejko and Kessissoglou, 2006; Goodwin, 1960]. A resonance changer is a hydraulic vibration absorber that dissipates the energy transmitted from the shaft to the thrust bearing.

### 1.3 Description of problem

The problems encountered in the applications briefly described in the previous section which use propeller or rotary blade system necessitates the development of control design methods that are cost effective, and can be implemented on a retrofit system. It is also imperative to have a degree of control and insight over the deterioration of vibration at the unmeasured outputs such as at the blade disk, in the above example. A similar

### 1.3. DESCRIPTION OF PROBLEM

---

problem is encountered in mechatronic positioning systems where the performance output is inferred from the measured output [Oomen et al., 2011]. If the performance output is not measured but the measured output has a dynamic relation to the performance output, then a model can be identified that is used to infer the effect of control on the unmeasured performance output. This is also called as inferential control or observer based control. It has been used for the control of lightly damped flexible modes using system identification techniques.

Another method [Halim and Cazzolato, 2006; Halim et al., 2008; Mazoni et al., 2011] uses a spatial performance index incorporated into the control design that achieves desired attenuation at different spatial regions. The spatial  $\mathcal{H}_\infty$  norm from the disturbance to a performance output that depends on both time and space [Skelton et al., 1997] is converted into an equivalent standard  $\mathcal{H}_\infty$  problem. This method is more comprehensive than the localised minimisation solutions. Therefore, it is particularly useful for large interconnected and flexible structures for which a model based controller would be computationally cumbersome. However, it is limited by the requirement for extensive distribution of sensors on the structure to measure as many vibration components at different points on the structure. Therefore, it is only suited for structures which have no weight or space constraints on sensor placement.

In order to fully understand the dynamic response of any structure or industrial machinery due to disturbance excitation, a detailed model of the plant is necessary. The source of disturbance excitation and its propagation at the receiving structure for the vibration problems encountered in marine and aerospace applications also requires the knowledge of a multitude of different factors such as hydrodynamics, acoustics, turbulence, temperature sensitivity etc. A simplified model of these processes with many assumptions can initially be utilised for the design of a control system. Any limitations and meaningful performance drawn from this controller is indicative of its practical viability and so it facilitates the design of a control system for the actual practical installation.

The experimental rig used in chapter 4, for example, is a simplified model that replicates the type of vibration encountered due to propeller blade excitation and so it facilitates the design and testing of control systems for such applications. Similarly, the experimental rig in chapter 8 is a mock-up installation to test the vibration forces due to human walking excitations on building floors. Both of these experimental facilities

### 1.3. DESCRIPTION OF PROBLEM

can be used to test the consequence of a SISO control design on one or more remote performance outputs using feedback from only a local measured output.

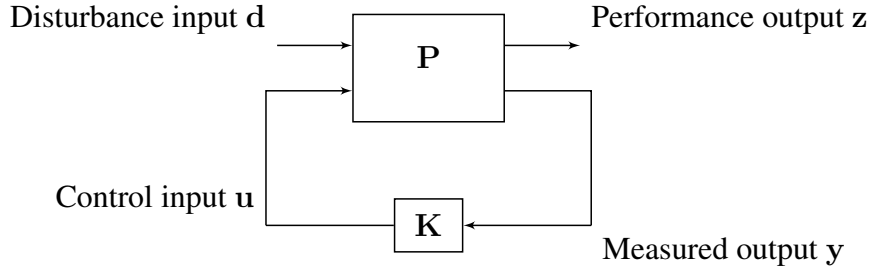


Figure 1.2: Linear Fractional Transformation representation of the remote vibration controller design problem. The controller is designed to minimise the level of the performance output based on feedback of measurement output

The remote vibration control problem can be cast in the framework of a general control configuration, which is widely used in the control literature for analysis and design, as shown in figure 1.2. Here,  $\mathbf{d}$  is the vector of exogenous inputs that act on the plant which in this case consists of all the disturbance excitation inputs,  $\mathbf{z}$  is the vector of exogenous outputs and represents vibration levels at all the locations that are desired to be minimised. This can include the measured as well as the remote vibration outputs. All the outputs available for measurement are included in  $\mathbf{y}$  and the set of control inputs is denoted by  $\mathbf{u}$ . The plant matrix,  $\mathbf{P}$ , relating the inputs to the outputs is denoted as

$$\begin{bmatrix} \mathbf{z} \\ \mathbf{y} \end{bmatrix} = \begin{bmatrix} \mathbf{P}_{11} & \mathbf{P}_{12} \\ \mathbf{P}_{21} & \mathbf{P}_{22} \end{bmatrix} \begin{bmatrix} \mathbf{d} \\ \mathbf{u} \end{bmatrix} \quad (1.1)$$

The local sensed output  $\mathbf{y}$  is fed back to a controller  $\mathbf{K}$ , which produces the control signal  $\mathbf{u}$ . The closed loop performance output  $\mathbf{z}$  from the disturbance input  $\mathbf{d}$  is the lower linear fractional transformation given as

$$\mathcal{F}_l(\mathbf{P}, \mathbf{K}) = \mathbf{P}_{11} + \mathbf{P}_{12}\mathbf{K}(\mathbf{I} - \mathbf{P}_{22}\mathbf{K})^{-1}\mathbf{P}_{21} \quad (1.2)$$

Feedback control design algorithms that reduce a desired norm of (1.2) have been widely discussed in the literature. If an accurate model of the process is available, then many of the modern control design methods, such as those that minimise the 2 norm  $\|\mathcal{F}_l(\mathbf{P}, \mathbf{K})\|_2$  and  $\infty$  norm  $\|\mathcal{F}_l(\mathbf{P}, \mathbf{K})\|_\infty$  can be safely used to regulate the measured

and unmeasured outputs of the system. But vital physical insight into the existence of solutions and the trade-off between the performance and measured outputs is not retained. It is thus desirable to develop a framework that takes into account conflicting performance requirements and gives better physical insight into the existence of vibration attenuation solutions than the traditional  $\mathcal{H}_2$  and  $\mathcal{H}_\infty$  optimal control design methods.

Therefore, the problem of remote vibration controller design can be described as the question of finding a controller that simultaneously minimises the remote vibration output  $z$  and the local sensed output  $y$ . As is illustrated using the examples in the preceding sections from the aerospace, maritime and other related areas, it is of practical significance to understand the effect of correcting action on the unmeasured vibration outputs. Furthermore, this knowledge can be utilised to design a suitable controller that achieves satisfactory response levels of the measured and unmeasured outputs. Additionally, this knowledge can be used as a design freedom to regulate the attenuation in vibration at the local and remote locations using a suitable controller.

### 1.4 Achievements

The primary aim of the work in this thesis is to advance the novel control design methodology that had previously been developed for the remote control of vibration [Daley and Wang, 2008; Wang and Daley, 2010]. The control design is based upon a parameterisation of all stabilising controllers in terms of a single design variable. The reduction in vibration output at several remote locations using a single pair of sensor and actuator can be parameterised in terms of this design freedom. It is specifically useful for the determination of performance limitations for vibration attenuation at remote locations. The portrayal of reduction in output at various locations as circular regions elucidates the feasibility of realising any controller that achieves simultaneous reduction in local and remote outputs. Although the original control design had been successfully implemented for discrete frequency or harmonic excitation, the broad band control of vibration is not practically viable in its original form.

A solution to the stable and stabilising controller problem for the geometric based control design is initially described. A detailed systematic procedure for the design of a stable controller that achieves reduction in remote output whilst simultaneously

mitigating the local output is presented in this thesis. This is motivated from the practical aspects of difficulties in unstable controller implementation. Also, the original control design does not guarantee suppression of control gain at out-of-band frequencies, thus causing a potentially destabilising control spillover. This problem is also addressed in this thesis. The modified control design retains the remarkable properties of the previous method that allows parameterisation of closed loop output at local and remote locations, using only a single design variable. The modified control design for broad band control of vibration is also experimentally validated using laboratory set-ups. It shows the practical viability of this geometric based control design.

Within the framework of this geometric approach, an important result is derived that proves the effect of local control action on the output at other remote locations, for frequencies close to resonance. This simplifies the active damping of resonance and is utilised to extend the control design for multimodal control.

The design parameter for local control is used to design multivariable decentralised controller. Decentralised control loops that interact with each other leads to instabilities when the controllers are implemented concurrently or individually. The design parameter is used to determine the integrity of individual feedback loops to the failure of other loops. A multivariable controller design is described in detail using this technique and the closed loop stability for interacting loops is also presented in terms of this design parameter.

## 1.5 Outline of thesis and contribution

The major contributions and description of the contents of the following chapters in this thesis is summarised below.

### Chapter 2

**Description:** This chapter introduces the geometric based design methodology for the remote control of vibration. The problems encountered in the experimental implementation of the original geometric based controller is initially detailed. The geometric approach for broad band control yields an unstable controller due to inversion of a non-minimum phase control path transfer function. The main issue of strong stabilisation

needs to be tackled before practical implementation for AVC problems. Various factors encountered in practical situations that contribute to a non-minimum phase system are also presented.

**Contribution:** The limitations of the previously developed geometric based control design are examined and the effect of practical issues on its real-world implementation are considered. Its advantages over other multivariable control design methods are also highlighted.

### Chapter 3

**Description:** A modified design procedure using the original geometric approach is formulated in this chapter such that the final compensator is stable and stabilising. Additionally, conditions to avoid control spillover are included as part of this design procedure. Weighting filters are used to shape the magnitude of this design parameter at out-of-band frequencies as its magnitude dictates the magnitude of complementary sensitivity function. Finally, the various steps in the design of a controller is detailed with the help of a numerical example problem.

**Contribution:** The main contribution in this chapter is the development of a systematic procedure based on the original geometric-based approach to design a stable controller that is also robust to excitation of unmodelled dynamics, whilst not compromising the performance in the desired frequency bandwidth. This design methodology safeguards performance of controller irrespective of sensor and actuator dynamics and also the time lags associated with the instrumentation.

Parts of this chapter on the design of a stable controller were presented at: Internoise 2011, Osaka, Japan [Ubaid et al., 2011a]. The systematic procedure to avoid control spillover was also presented at: Asia Pacific Vibration Conference 2011, Hong Kong [Ubaid et al., 2011b].

### Chapter 4

**Description:** The control design developed in chapter 3 is experimentally validated using a propeller blade test rig. Control force is applied on a non-resonating part

of the system which is connected to a resonating structure. It replicates to a limited extent the problem encountered in the control of vibration at the thrust block due to disturbance from the propeller blades in naval vessels. The controllability and observability issues using the geometric based controller are implicitly tackled by the portrayal of constraint regions in the design freedom plane. It is also shown that the design parameter has a direct correspondence to the Relative Gain Array. This is helpful to analyse the difficulty in reducing output at the remote location using control action solely at the thrust block. Very small elements of the RGA for input at thrust block to the output at blade end shows the very limited effect of control at design frequencies.

**Contribution:** This chapter confirms the practical viability of the control design method developed in chapter 3. A stable and robust controller is implemented using this geometric approach for a system that replicates the vibration problem encountered in naval vessels due to propeller blade excitations. The significance of the geometric based approach for complex interconnected structure becomes apparent. The relation between design parameter and Relative Gain Array simplifies portrayal of the efficiency of local control input on remote outputs.

The main experimental results with the complete design procedure were presented at: UKACC International Conference on Control 2012, Glamorgan, UK [Ubaid et al., 2012].

## Chapter 5

**Description:** The stable geometric design methodology developed in chapter 3 is analysed for active damping close to resonance. It is shown analytically that the value of design freedom that achieves reduction in output at the local point close to resonance will also achieve global attenuation. This is verified experimentally on a beam rig set-up and the resonance associated with its first bending mode is actively dampened.

**Contribution:** This chapter analytically proves the effect of active damping close to resonance on the global vibration reduction for a lightly damped structure. This result provides a significant mathematical proof for the performance of any controller that achieves reduction close to resonance at the local point. This is also validated using

an experimental beam rig facility for the control of vibration at frequencies close to its first bending mode.

Parts of this chapter excluding the experimental results has been submitted for publication in the Journal of Sound and Vibration.

### Chapter 6

**Description:** The limitations of direct velocity feedback control for global vibration reduction are highlighted. It is compared with a controller design based on the geometric approach but with similar objectives. The theory that underpins this design is presented in chapter 5, which facilitates the active damping of a simple structure close to resonance. The design freedom parameter approaches the centre of circle corresponding to local vibration reduction, as the direct velocity feedback gain is increased. This causes the onset of new modes at antiresonant frequencies because the region in the design freedom plane, corresponding to reduction at remote locations, does not contain the design freedom that corresponds to this gain.

**Contribution:** A novel design technique that utilises the optimal values for design parameter close to resonance is presented. It shows that the limitations arising from direct velocity feedback control can be addressed using this geometric method. As the design freedom is selected for different frequencies, a controller which dissipates energy at different levels for different frequencies is potentially achievable. The requirements to achieve this are clearly described in the  $\gamma$ -plane while designing a controller.

### Chapter 7

**Description:** Controller design for remote vibration attenuation using multiple feedback control loops is presented. The disadvantages of a centralised MIMO controller for vibration attenuation problems can be overcome using decentralised sequential loop closing technique. The geometric controller design methodology can be used for the design of individual feedback controllers for each control point. Robustness to instabilities due to the failure of inner feedback loops is presented in terms of the design freedom parameter.

**Contribution:** Closed loop stability considerations arising due to the interactions between individual feedback loops is determined using the design parameter. A design rule that guarantees the stability of sequentially designed feedback loop to the failure of inner loops is presented.

### Chapter 8

**Description:** The sequential loop closing control design for a decentralised multivariable implementation is experimentally validated using a laboratory facility. Two local feedback loops are designed for suppression of output at different test points on a 15 tonne slab structure. The interaction between the two feedback loops causes stability issues that is addressed in terms of the design parameter. The integrity of both feedback loops to the failure of the other loop is safeguarded inspite of strong interactions.

**Contribution:** Sequential loop closing control design using the geometric-based approach is experimentally validated using a laboratory facility.

The experimental results along with the sequential loop closing control design is to be presented at: International Congress on Sound and Vibration, 2013.

### Chapter 9

Concluding remarks with recommendations for future work to improve the proposed geometric based control design is presented.

## Chapter 2

# Remote Vibration Control Design Using Geometric Approach

### 2.1 Introduction

This chapter sets out the groundwork for the remainder of this thesis. An introduction to the original geometric based control design is first presented and then the limitations of the controller which restricts its implementation on a real-world practical installation will be established. Initially, some of the underlying factors that hamper the realisation of a stable controller are presented. Subsequently, the difficulty in the practical implementation of an unstable controller is exemplified with an example.

A novel geometric based methodology for control design presented in [Daley and Wang, 2006] addresses the problem of remote vibration attenuation. According to this method, vibration at any inaccessible *remote* point on a large interconnected structure is tackled using sensors and actuators placed *locally* at any other convenient location. Fundamentally the design approach enables a feedback controller to be implemented that satisfies the closed loop specifications to achieve desired vibration attenuation at both the *local* and *remote* points. A knowledge of the dynamics of the path from the disturbance excitation to the *local* point and vice versa is to be available for control design purposes.

It should be noted that vibration attenuation at the *local* output can be achieved using any controller that minimizes the sensitivity function. For *remote* vibration control

problem, a filter is needed that affects the gain and phase of this compensator so that in addition to attenuation at the *local* point, vibration output at certain predetermined *remote* points is also reduced. This filtering action is implemented in terms of a tuning parameter that portrays the conflicting performance requirements at the *local* and *remote* points on the structure. This tuning parameter encapsulates the design freedom which regulates the extent to which simultaneous attenuation at discrete frequencies in a certain desired frequency band can be achieved.

If it is assumed that the dynamics of the *local* control and *remote* disturbance paths are available during a commissioning stage and there are not any significant changes to the properties of the system/structure from the testing to the operational phase, the limitations on maximum attenuation of both *remote* and *local* vibration at the excitation frequency can be denoted in terms of this design parameter. By selecting an optimal value for the design freedom parameter at this frequency, which could (for example) represent maximum attenuation of *remote* vibration without enhancement in *local* vibration, or vice versa, a controller can be implemented in terms of this design freedom parameter. The limitations on simultaneous vibration reduction at different locations in a system can be easily deduced using this design methodology.

Vibration attenuation at a *remote* point for a discrete frequency is portrayed as a circle in a design freedom plane. Similar circles for *local* and other *remote* points can also be plotted on the same plane. This gives a physical insight into the extent of achievable simultaneous vibration attenuation at the *local* and *remote* points. Then the physical limitations on simultaneous vibration reduction at different locations on the structure is easily deduced from this plot. The values selected for the design freedom parameter from this plane regulates the extent of simultaneous vibration attenuation. Closed loop stability issues can also be cast in terms of the selection and interpolation of points on this design freedom plane.

## 2.2 Preliminary design procedure

In this section the original geometric design methodology for the broadband attenuation of vibration [Wang and Daley, 2007a,b] is revisited and the design freedom parameter is formulated. A system is considered where a SISO control loop design using a sensor actuator pair is developed for a single disturbance excitation. If the primary excitation and control inputs to the system are denoted as  $f_p(t)$  and  $f_c(t)$ , respectively, then the multivariable transfer function matrix relating the force inputs to the vibration outputs is given as

$$\begin{bmatrix} q_c(j\omega) \\ q_p(j\omega) \end{bmatrix} = \begin{bmatrix} g_{cc}(j\omega) & g_{cp}(j\omega) \\ g_{pc}(j\omega) & g_{pp}(j\omega) \end{bmatrix} \begin{bmatrix} f_c(j\omega) \\ f_p(j\omega) \end{bmatrix} \quad (2.1)$$

where  $q_c(j\omega)$  represents the vibration of a local point at which the control force acts and  $q_p(j\omega)$  represents the vibration output of some remote point where the primary excitation acts. It should be noted that the matrix in (2.1) represents receptance, mobility or accelerance functions depending on whether the output considered is the displacement, velocity or acceleration. In the absence of any control input, i.e.  $f_c(j\omega) = 0$ , the local and remote vibration outputs are given as

$$q_c(j\omega) = g_{cp}(j\omega)f_p(j\omega) \quad (2.2)$$

$$q_p(j\omega) = g_{pp}(j\omega)f_p(j\omega) \quad (2.3)$$

The measurement at the local control point  $q_c(j\omega)$  is fed back to the controller  $k(j\omega)$  in order to generate the control signal  $f_c(j\omega)$  according to

$$f_c(j\omega) = -k(j\omega)q_c(j\omega)$$

The closed loop vibration output at the local and remote points, in the presence of feedback control can respectively be written as

$$q_c(j\omega) = [1 + g_{cc}(j\omega)k(j\omega)]^{-1} g_{cp}(j\omega)f_p(j\omega) \quad (2.4)$$

## 2.2. PRELIMINARY DESIGN PROCEDURE

---

and

$$q_p(j\omega) = [1 - g_{pp}^{-1}(j\omega)g_{pc}(j\omega)k(j\omega) \{1 + g_{cc}(j\omega)k(j\omega)\}^{-1} g_{cp}(j\omega)] g_{pp}(j\omega)f_p(j\omega) \quad (2.5)$$

Comparing the open loop outputs given by (2.2) and (2.3) with the closed loop outputs given by (2.4) and (2.5), it is clear that for a discrete frequency  $\omega_0$ , simultaneous reduction in output at both the local and remote points can be achieved using a compensator  $k(j\omega)$  that satisfies both conditions

$$|[1 + g_{cc}(j\omega_0)k(j\omega_0)]^{-1}| < 1 \quad (2.6)$$

and

$$|1 - g_{pp}^{-1}(j\omega_0)g_{pc}(j\omega_0)k(j\omega_0) \{1 + g_{cc}(j\omega_0)k(j\omega_0)\}^{-1} g_{cp}(j\omega_0)| < 1 \quad (2.7)$$

The two algebraic inequalities given by (2.6) and (2.7) are linear in the unknown variable  $k(j\omega_0)$  and for suitable selection of this quantity the measured and unmeasured outputs can be regulated. The same task can be accomplished using many of the modern control design methods such as  $\mathcal{H}_\infty$  control. However, vital physical insight into the existence of solutions and the trade-off between the performance and measured outputs is not retained by these methods. It is thus desirable to develop a framework that straightforwardly reveals conflicting performance requirements when simultaneous reduction in output at the local and remote points is not achievable. The geometric methodology introduced in [Daley and Wang, 2006] achieves this by using a design parameter that translates the reduction in output at the local and remote points as constraint regions in a common plane. According to this method, the proposed design parameter  $\alpha$  is denoted as

$$\alpha(j\omega) = S(j\omega) - 1 = \frac{-g_{cc}(j\omega)k(j\omega)}{1 + g_{cc}(j\omega)k(j\omega)} \quad (2.8)$$

where  $S(j\omega)$  is the sensitivity function. The closed loop local and remote vibration outputs from (2.4) and (2.5) can then be denoted in terms of this design freedom variable as (2.9) and (2.10) respectively

$$q_c(j\omega) = [1 + \alpha(j\omega)] g_{cp}(j\omega)f_p(j\omega) \quad (2.9)$$

## 2.2. PRELIMINARY DESIGN PROCEDURE

$$q_p(j\omega) = \left[ 1 + \alpha(j\omega) \frac{g_{cp}(j\omega)g_{pc}(j\omega)}{g_{cc}(j\omega)g_{pp}(j\omega)} \right] g_{pp}(j\omega) f_p(j\omega) \quad (2.10)$$

At any arbitrary point  $x$  on the structure, the vibration output  $q_x(j\omega)$  due to this primary and control excitation can be generalised as

$$q_x(j\omega) = \left[ 1 + \alpha(j\omega) \frac{g_{cp}(j\omega)g_{xc}(j\omega)}{g_{cc}(j\omega)g_{xp}(j\omega)} \right] g_{xp}(j\omega) f_p(j\omega) \quad (2.11)$$

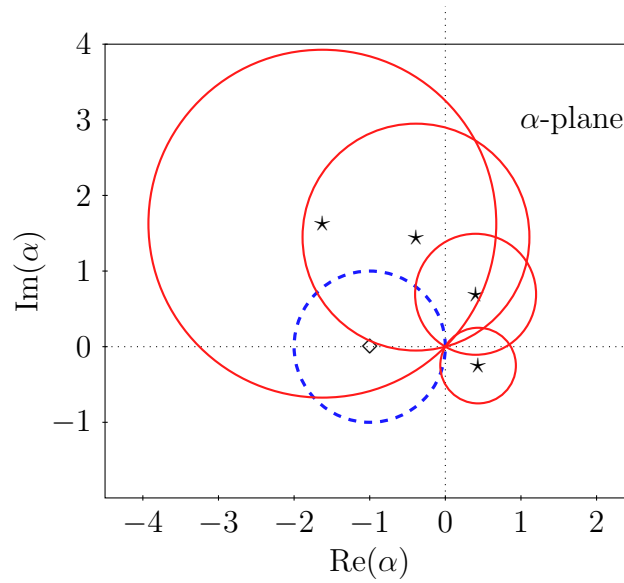


Figure 2.1: Circles in  $\alpha$ -plane for discrete frequencies which signify reduction in output at local (dashed) and remote (solid) points, and their centres which denote maximum attenuation at the local ( $\diamond$ ) and remote ( $\star$ ) points

Attenuation in the closed loop output at the local point for a discrete frequency  $\omega_0$  with feedback control results from a reduction in the closed loop gain in (2.9) relative to the uncontrolled state. This is determined by the magnitude of the expression inside the brackets in the RHS of this closed loop equation. The reduction in output at the local point for a discrete frequency  $\omega_0$  can therefore be expressed as

$$|\alpha(j\omega_0) + 1| < 1 \quad (2.12)$$

Inequality (2.12) at any particular frequency  $\omega_0$  is an algebraic constraint which describes the region inside a unit circle with centre  $(-1, 0)$  in a 2-D complex  $\alpha$ -plane.

## 2.2. PRELIMINARY DESIGN PROCEDURE

---

Similarly, attenuation in vibration output  $q_x(j\omega)$  at a remote point  $x$  for discrete frequency  $\omega_0$  with feedback control can be expressed as

$$\left| 1 + \frac{\alpha(j\omega_0)}{V_x(j\omega_0)} \right| < 1 \quad (2.13)$$

$$|\alpha(j\omega_0) + V_x(j\omega_0)| < |V_x(j\omega_0)| \quad (2.14)$$

where

$$V_x(j\omega_0) = \frac{g_{cc}(j\omega_0)g_{xp}(j\omega_0)}{g_{cp}(j\omega_0)g_{xc}(j\omega_0)} \quad (2.15)$$

Inequality (2.14) is an algebraic constraint in terms of the design parameter which describes the region inside a circle with centre  $-V_x(j\omega_0)$  and radius  $|V_x(j\omega_0)|$  in the same  $\alpha$ -plane. Figure 2.1 shows the circles representing (2.12) and (2.14) in a 2-D  $\alpha$ -plane which is a complex argand diagram. A value of  $\alpha(j\omega_0)$  at the centre of circle (2.14) corresponds to maximum attenuation of remote vibration at the disturbance frequency  $\omega_0$ .

Now the conditions of simultaneously reducing vibration at the local and remote points is defined as the problem of selecting values for  $\alpha$  from inside the intersecting region of the two circles (2.12) and (2.14) in the  $\alpha$ -plane. Based on the required degree of vibration reduction at the remote and local point,  $\alpha$  can be chosen nearer to the centre of either circle that corresponds to respectively remote or local vibration attenuation. The control of vibration across a broad frequency band  $[\omega_L, \omega_H]$  is implemented using a controller given by (2.16) such that  $\alpha(j\omega)$  is the transfer function obtained by the interpolation of  $\alpha(j\omega_i)$ ,  $i = 1, 2, \dots, n$ , at discrete intervals in the design frequency band. This interpolation procedure to form the transfer function from optimal values of design parameter is explained in detail in section 3.5.3.

$$k(j\omega) = \frac{-\alpha(j\omega)}{[1 + \alpha(j\omega)]g_{cc}(j\omega)} \quad (2.16)$$

The controller given in (2.16) then satisfies all the closed loop specifications defined within the design freedom  $\alpha(j\omega)$ . This approach does not require estimation of the mass, damping and stiffness matrices or the evaluation of modal parameters of the structure. The local control path transfer function for this method can be identified using any modelling/system identification technique available to the control designer. It is well accepted that experimental modal analysis of large complex structures is a cum-

## 2.2. PRELIMINARY DESIGN PROCEDURE

---

bersome process with varying degrees of success [Peeters et al., 2004], especially for highly damped structures. A clear advantage using this method is that it does not require very accurate identification of mode shapes, damping values or natural frequencies of the structure. Hence, it is particularly suited for complex structures for which it may not be easy to obtain the modal parameters related to only an individual component of the whole structure. This is the case when the vibration due to a resonating component of the structure gets transmitted to non resonating parts of the structure [Daley and Wang, 2008; Dylejko and Kessissoglou, 2006; Merz et al., 2010; Pearson and Emery, 2003; Ubaid et al., 2012]. The blade rig facility used for experimental verification of the geometric-based control design in chapter 4 illustrates the problem of attenuation at the receiving structure. The control force is applied on a region of structure which is rigidly connected to the resonating member. Due to the structural properties associated specifically with joints and fasteners [Ibrahim and Pettit, 2005], it is difficult in this case to accurately model the overall dynamic properties of the assembled structure. Uncertainties and non linear characteristics arise due to the complex behaviour of connection elements [Ouyang et al., 2006]. Also, the mathematical modelling of frictional contact surfaces, to describe its dynamic characteristics, is unduly complicated. Although connection elements affect the damping behaviour due to the dissipation of energy, the dynamic response at discrete points on the built-up structure can be computed using vibration test measurements on the structural members themselves [Jalali et al., 2007]. Global control of the structure using modal control methods will not achieve desired results due to difficulties in reachability and observability of the states at the unmeasured location. These limitations will manifest as smaller regions of intersection for the circles in  $\alpha$ -plane corresponding to attenuation at the local and unmeasured locations.

## 2.3 Practical Considerations

The feedback controller using the geometric design approach from [Wang and Daley, 2007a], which is reviewed in section 2.2, is implemented as a function of the design freedom variable that incorporates the inverse of the local control path transfer function. A model based controller is recommended only if the plant is modeled accurately, especially for a lightly damped structure [Preumont, 2002]. The uncertainty in the identified plant model at higher frequencies, particularly for a displacement response, increases due to the noise component in measurements therefore a model based controller is not suitable when excitation is dominated by high frequency characteristics. Passive control can be used for vibration attenuation at high frequencies. Moreover, the excitations that are generated due to rotating or reciprocating components in large equipment such as industrial machinery or diesel engines are usually dominated by low frequency characteristics. Hence, this inverse model based geometric control design can be pursued as an active vibration control solution for similar applications.

It is desirable to use a collocated and dual sensor actuator pair for feedback control due to the inherent stability robustness [Balas, 1979]. This allows application of a passive control law; such as velocity feedback control that alters only the damping of the natural frequencies in the closed loop system. Also, it benefits from the application of very large feedback control gains for better performance, irrespective of the modelling errors. Moreover, the design of decoupled SISO feedback loops is comparatively easier using a collocated and dual sensor actuator pair [Canavin, 1978]. The stability of the closed loop system is guaranteed if the individual feedback loops are themselves stable. The favourable conditions with the use of collocated control can be attributed to the alternating pole-zero pattern in the open loop transfer function, which is always minimum phase. So, as the nominal gain increases, the root locus plot from all the poles to the zeros remains entirely in the left half plane and the phase is restricted between  $0^\circ$  and  $180^\circ$ . The sensor and actuator for the geometric based control design in section 2.2 is assumed to be collocated. The limitations of other control design methods with non-ideal collocated set-up is generally due to the resulting additional phase lag.

#### 2.3.1 Time Delay and Phase Lag

As stated previously, the sensor and actuator used for the geometric design approach can be collocated and dual which in theory should give a minimum phase transfer function with its phase bounded between  $0^\circ$  and  $180^\circ$ . But it has been widely appreciated that even when the sensors and actuators are collocated, there is significant phase lag in the frequency response [Ren et al., 1997], which limits the performance of feedback control. The phase lag of the open loop frequency response coupled with the limitations on accurate model identification generally presents the control designer with a non-minimum phase local control path transfer function approximation. This is especially true when excitation data-based model identification techniques are used for control design.

The phase lag in the frequency response is attributed to a number of different factors in active control design. In most practical cases, even when the sensor is located very close to the actuator, it is very difficult to achieve true physical collocation. The factors that affect mis-collocation of distributed transducers are transducer registration, spatial gain weighting, type and aperture [Burke et al., 1993]. There has also been considerable work to improve physical collocation such as by designing self sensing actuators [Dosch et al., 1992; Paulitsch et al., 2006a]. Also, to ensure duality, the sensor and actuator has to be energetically conjugated by using the same type of transducer; for example, force input coupled with velocity or acceleration measurement, or torque coupled with angular measurements, etc. [Fahy and Gardonio, 2007].

Moreover, the sensors and actuators have significant dynamics associated with them and even if they are collocated, there is phase lag in the frequency response [Aoki et al., 2008]. Sensors such as piezo-strip, linear accelerometer, velocity sensor, etc. and actuators such as PZT, electrohydraulic, electrodynamic proof-mass actuators, etc. which are widely used for AVC applications have significant dynamics associated with them [Rohlfing et al., 2011a] that contribute to the dynamics of the local control path. Also, the time delays in the electronic instrumentation contribute to unmodelled phase shift. There are several stages in the instrumentation that affect the time delay [Heylen et al., 2006] which is predominantly due to sampling in digital controllers (A/D and D/A), integration, power amplification, anti-aliasing and reconstruction filtering.

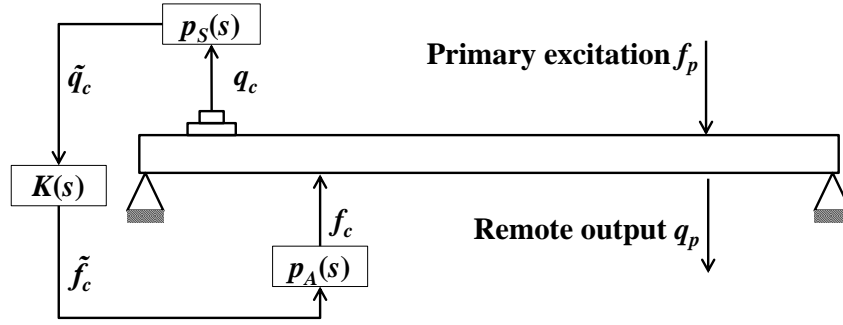


Figure 2.2: The sensor and actuator dynamics included in the open loop transfer function

### Implication for the geometric design approach

The sensor and actuator dynamics can cause difficulties in many active vibration control problems. The dynamics of the shaker has to be explicitly taken into account especially when its resonance frequency is close to the frequency of problematic excitation [Díaz and Reynolds, 2010]. This is because it introduces additional phase lag in the open loop transfer function. In this section, the dynamics of the sensor and actuator that are very likely to be encountered in practical installation are explicitly incorporated in the open loop transfer function and their effect on controller implementation using the geometric design methodology is presented.

The multivariable transfer function matrix in (2.1) relates the actual local and remote outputs with the force inputs. However, the effect of sensor and actuator dynamics is neglected on this plant model. The sensor dynamics affect the output measurement and the actuator dynamics affect the actual force applied on to the structure from the control input. Figure 2.2 shows representation of sensor and actuator dynamics included separately in the local control path dynamics. The control input  $\tilde{f}_c$  in figure 2.2 represents voltage or current that drives the actuator. The sensor measurement output is related to the actual kinematic quantity as

$$\tilde{q}_c(j\omega) = P_S(j\omega)q_c(j\omega) \quad (2.17)$$

The actuator force applied on the structure is related to the control input as

$$f_c(j\omega) = P_A(j\omega)\tilde{f}_c(j\omega) \quad (2.18)$$

### 2.3.1. TIME DELAY AND PHASE LAG

---

Substituting (2.17) and (2.18) in the equation for output at the local control point gives

$$\frac{\tilde{q}_c(j\omega)}{P_S(j\omega)} = g_{cc}(j\omega)P_A(j\omega)\tilde{f}_c(j\omega) + g_{cp}(j\omega)f_p(j\omega)$$

$$\tilde{q}_c(j\omega) = g_{cc}(j\omega)P_A(j\omega)P_S(j\omega)\tilde{f}_c(j\omega) + g_{cp}(j\omega)P_S(j\omega)f_p(j\omega)$$

$$\tilde{q}_c(j\omega) = \tilde{g}_{cc}(j\omega)\tilde{f}_c(j\omega) + \tilde{g}_{cp}(j\omega)f_p(j\omega)$$

where

$$\tilde{g}_{cc}(j\omega) = g_{cc}(j\omega)P_A(j\omega)P_S(j\omega)$$

and

$$\tilde{g}_{cp}(j\omega) = g_{cp}(j\omega)P_S(j\omega)$$

Similarly, substituting (2.18) in the expression for output at the remote point gives

$$q_p(j\omega) = \tilde{g}_{pc}(j\omega)\tilde{f}_c(j\omega) + g_{pp}(j\omega)f_p(j\omega)$$

where

$$\tilde{g}_{pc}(j\omega) = g_{pc}(j\omega)P_A(j\omega)$$

The transfer function matrix in (2.1) can be written with the inclusion of sensor and actuator dynamics to relate the sensor measured output with the control signal applied to the actuator for local control and primary excitation paths as

$$\begin{bmatrix} \tilde{q}_c(j\omega) \\ q_p(j\omega) \end{bmatrix} = \begin{bmatrix} \tilde{g}_{cc}(j\omega) & \tilde{g}_{cp}(j\omega) \\ \tilde{g}_{pc}(j\omega) & g_{pp}(j\omega) \end{bmatrix} \begin{bmatrix} \tilde{f}_c(j\omega) \\ f_p(j\omega) \end{bmatrix} \quad (2.19)$$

In (2.19),  $\tilde{g}_{cc}(j\omega)$  can therefore be generally considered as non-minimum phase due to practical problems of non-collocation and non-duality and phase delays which can be transformed as right half plane zeros. Any remote vibration control problem for simulation purposes can therefore be replicated using a non-collocated local control sensor and actuator pair. As shall be seen, with the geometric methodology, there is no need to determine actuator  $P_A(j\omega)$ , or sensor  $P_S(j\omega)$  dynamics explicitly, or the time delays due to instrumentation - A/D, D/A, integration, amplification, filtering, etc and

the measured open loop FRF between any input and any output itself is sufficient to design a control system.

The geometric-based remote vibration controller given as (2.16) in section 2.2 is therefore more accurately implemented as

$$k(j\omega) = \frac{-\alpha(j\omega)}{[1 + \alpha(j\omega)] \tilde{g}_{cc}(j\omega)} \quad (2.20)$$

The transfer function from the local control actuator to the local vibration sensor,  $\tilde{g}_{cc}(j\omega)$ , appears as a factor in the denominator of the controller transfer function in (2.20). It has been argued that  $\tilde{g}_{cc}(j\omega)$  is likely non-minimum phase even when the sensor and actuator are collocated due to instrumentation phase lags, acquisition delays and sensor, actuator dynamics. The right half plane zero(s) of the local control path transfer function would therefore result in an unstable controller which cancels the non-minimum phase zeros of the local control path transfer function. This will introduce an unstable hidden mode giving an unbounded control signal and therefore cannot be implemented. Additionally, an unstable controller in general is not practical because of problems associated with it such as difficulty in controller commissioning, excessive actuator use and instability issues if the feedback loop fails.

### 2.3.2 Unstable Controller - Testing and Implementation

Owing to the difficulties associated with unstable controllers, controller stabilisation has been the focus of earlier control design research. Unstable controllers are encountered with many controller design methods and some of the attempts in addressing controller stabilisation can be found in [Liu et al., 2000] for state feedback pole assignment design, in [Liu et al., 2001] for proportional-integral plus controllers and in [Petersen, 2009] for an  $\mathcal{H}_\infty$  controller design. A modified design procedure that results in a stable controller whilst retaining the informative approach of this geometric methodology is established in the next chapter.

It is always desirable to implement a strongly stabilising controller due to difficulties in the practical implementation of an unstable controller. One of the obstacles encountered with an unstable controller that is also relevant to the experimental set-up used in the remote vibration attenuation problem in this project will be demonstrated here using

### 2.3.2. UNSTABLE CONTROLLER

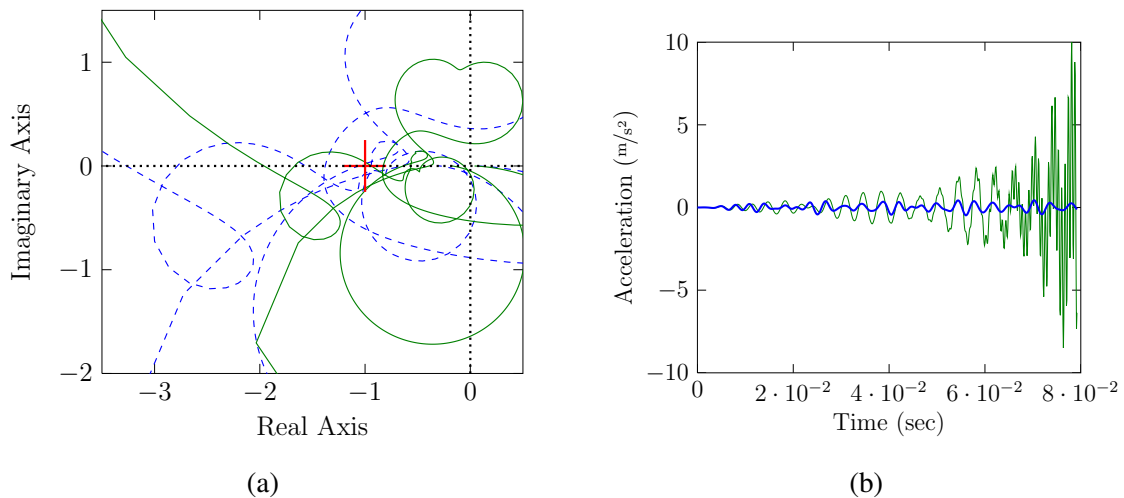


Figure 2.3: (a) Nyquist diagram of open loop system for nominal gain (blue dashed) encircles the critical point and is closed loop stable if the controller itself is unstable but as the dc gain reduces below 60% nominal value (green solid) the closed loop system becomes unstable as is seen in the corresponding (b) time response of closed loop simulation outputs for nominal gain (blue) and 60% of it (green)

an example. This example serves to illustrate the complexities in implementation and testing of unstable controllers in similar applications.

Due to robustness issues, in practice, any new controller design is usually commissioned on a real world plant or experimental set-up with very small open loop gain that is then gradually increased [Stoustrup and Niemann, 1997]. One method that can be employed to start up an unstable controller is to gradually switch between the Youla parameterisation of a stable controller to another one of the unstable controller until the latter is fully active [Balini et al., 2011]. However, if the unstable controller is to be implemented directly, then the closed loop system can go unstable for values of gain that are different from the nominal design values.

Consider the closed loop stability of the system described in section 4.2 when an unstable but stabilising broadband controller is to be implemented. An unstable controller would be stabilising for a stable and non-minimum phase plant if, as per the nyquist stability criterion, the polar plot of the open loop transfer function encircles the critical point  $-1 + j0$  as many times as there are unstable poles in the open loop transfer function. Figure 2.3(a) shows the nyquist diagram of such a system for the nominal controller gain. Since the plant itself is stable, for closed loop stability the number of

encirclements of the critical point is dictated by the number of unstable controller poles. Now consider the closed loop stability of the same open loop system when the controller gain is implemented for a fraction of the designed gain. If the gain of controller falls below 60% of this open loop design gain, then the closed loop system would go unstable as seen in figure 2.3(b). Similarly, it can be easily verified that the closed loop system would go unstable when the controller gain is increased beyond a certain limit. This would present challenges in the practical implementation and commissioning in plants when the control action starts to wind up gradually. This is an indirect effect of the time delays and phase lag in the open loop control path and motivates investigation of a modified approach that benefits from the remote geometric methodology whilst realising a stable controller.

## 2.4 Summary

This chapter introduces the geometric based control design method that had previously been developed to address the problem of remote vibration control. The parameterisation of vibration reduction at the local and remote points in terms of a design freedom parameter is revisited. The benefits of this method over traditional multivariable control design methods is also highlighted in this chapter. The justification for using this intuitive control design for vibration attenuation in large scale applications is presented. Unlike the 'handle turning' nature of modern multivariable control design, this approach retains vital physical insight into the trade-offs between vibration mitigation of the performance and measured outputs. The practical considerations relating to the actuator and sensor dynamics along with time delays in the instrumentation affect the realisation of a stable controller. Finally, the difficulty encountered in the implementation of unstable controllers are highlighted with the help of an example.

# Chapter 3

## Design of Strongly Stabilising Controllers

### 3.1 Introduction

The geometric design method had been experimentally validated on a rig facility to attenuate local and remote vibration due to a discrete frequency excitation [Daley and Wang, 2008]. However, there are some drawbacks to this control design when broadband frequency attenuation is desired in the local and remote outputs. As noted in the previous chapter, controller implementation for suppressing vibration due to broadband excitation involves inversion of the local control path model. This will lead to an unstable controller if the local control path model has non-minimum phase characteristics. Although collocated sensors and actuators are generally used in the local control path, the transfer function can still be non-minimum phase due to non-ideal practical conditions. In [Wang et al., 2010], it is shown that the closed loop stability can be determined from the relation of the design parameter,  $\alpha$ , with the Youla parameter.

It is well known that a stable Youla or Q-parameter parameterises all stabilising controllers. Therefore, an  $\alpha$  parameter that corresponds to a stable Q parameter would also ensure closed loop stability of the system. However, the Q-parameterisation itself does not systematically ensure stability of the controller. This broad-band controller is also not resilient to parasitic dynamics or control spillover resulting from the limitations in identification at high frequencies. If the controller has significant energy at higher

frequencies then the unmodelled high frequency dynamics will be excited.

The main contributions in this chapter are the development of solutions to address the issues of controller stability and robustness at high frequencies. A modified control design approach is proposed which uses a single design freedom variable to parameterise vibration attenuation feasibility in a straightforward geometric representation that is similar to the original method. It therefore retains the beneficial physical insight into the feasibility of simultaneous local and remote vibration attenuation whilst yielding a strongly stabilising controller. Additionally, the control spillover that can affect stability due to unmodelled lightly damped high frequency dynamics is addressed. The new method is also extended for both global performance requirements such as kinetic energy reduction and for multiloop sequential loop closing controller designs.

## 3.2 Design of Stable and Broadband Controller

A modified design approach is formulated in this section that gives a stable remote vibration controller using the geometric methodology. The minimum phase counterpart of the local control path transfer function, which is assumed to be non-minimum phase, is used to denote a new design freedom parameter. The non-minimum phase transfer function  $\tilde{g}_{cc}(j\omega)$  is decomposed into its minimum phase counterpart  $\hat{g}_{cc}(j\omega)$ , which has all its RHP zeros reflected into the LHP, and an all pass transfer function  $B_{cc}(j\omega)$  as (3.1).

$$\tilde{g}_{cc}(j\omega) = \hat{g}_{cc}(j\omega)B_{cc}(j\omega) \quad (3.1)$$

A new design freedom parameter  $\gamma$  is introduced as

$$\gamma(j\omega) = \frac{-\hat{g}_{cc}(j\omega)k(j\omega)}{1 + \tilde{g}_{cc}(j\omega)k(j\omega)} \quad (3.2)$$

In the presence of local feedback control action  $\tilde{f}_c(j\omega) = -k(j\omega)\tilde{q}_c(j\omega)$ , the closed loop local and remote vibration outputs for the multivariable transfer function matrix in (2.19) can be written as

$$\tilde{q}_c(j\omega) = \left[ 1 + \left\{ -\frac{\tilde{g}_{cc}(j\omega)k(j\omega)}{1 + \tilde{g}_{cc}(j\omega)k(j\omega)} \right\} \right] g_{pp}(j\omega)f_p(j\omega) \quad (3.3)$$

### 3.2. STRONGLY STABILISING CONTROLLER

---

$$q_p(j\omega) = \left[ 1 + \left\{ -\frac{\tilde{g}_{cc}(j\omega)k(j\omega)}{1 + \tilde{g}_{cc}(j\omega)k(j\omega)} \right\} \frac{\tilde{g}_{cp}(j\omega)\tilde{g}_{pc}(j\omega)}{\tilde{g}_{cc}(j\omega)g_{pp}(j\omega)} \right] g_{pp}(j\omega)f_p(j\omega) \quad (3.4)$$

Substituting (3.2) in (3.3) and (3.4) gives (3.5) and (3.6), respectively

$$\tilde{q}_c(j\omega) = [1 + \gamma(j\omega)B_{cc}(j\omega)] \tilde{g}_{cp}(j\omega)f_p(j\omega) \quad (3.5)$$

$$q_p(j\omega) = \left[ 1 + \gamma(j\omega)B_{cc}(j\omega) \frac{\tilde{g}_{cp}(j\omega)\tilde{g}_{pc}(j\omega)}{\tilde{g}_{cc}(j\omega)g_{pp}(j\omega)} \right] g_{pp}(j\omega)f_p(j\omega) \quad (3.6)$$

Attenuation in the local and remote vibration levels using feedback control results from a reduction in the magnitude of the terms inside the brackets in (3.5) and (3.6) which can be represented as (3.7) and (3.9), respectively

$$|\gamma(j\omega) + U_c(j\omega)| < |U_c(j\omega)| \quad (3.7)$$

where

$$U_c(j\omega) = \frac{1}{B_{cc}(j\omega)} \quad (3.8)$$

$$|\gamma(j\omega) + U_p(j\omega)| < |U_p(j\omega)| \quad (3.9)$$

where

$$U_p(j\omega) = \frac{\hat{g}_{cc}(j\omega)g_{pp}(j\omega)}{\tilde{g}_{cp}(j\omega)\tilde{g}_{pc}(j\omega)} \quad (3.10)$$

$U_p(j\omega)$  given by (3.10) is a dimensionless quantity which, as noted in earlier fundamental control research, provides a useful measure for the severity of the trade-off between stability robustness and disturbance attenuation [Freudenberg et al., 2003a]. For frequencies at which  $U_p(j\omega)$  is very large or very small, the trade-off between stability robustness and disturbance attenuation will be severe which is the case in flexible structures and is attributed to its lightly damped zeros [Freudenberg et al., 2003b].

It should be noted that (3.8) and (3.10) computed at any discrete frequency  $\omega_0$  is a complex number that denotes the gain and phase of these transfer functions at this frequency. As a result, (3.7) and (3.9) for a discrete frequency  $\omega_0$  are algebraic inequalities

### 3.2. STRONGLY STABILISING CONTROLLER

that represent region inside circles in a  $\gamma$ -plane. Inequality (3.7) at discrete frequency  $\omega_0$  represents a circle with centre  $-U_c(j\omega_0)$  and radius  $|U_c(j\omega_0)|$  in the  $\gamma$ -plane. Similarly, inequality (3.9) at discrete frequency  $\omega_0$  represents a circle with centre  $-U_p(j\omega_0)$  and radius  $|U_p(j\omega_0)|$  in the  $\gamma$ -plane. If a controller is implemented using a value of  $\gamma$  from inside both these circles, then simultaneous remote and local vibration attenuation is possible for a primary excitation at frequency  $\omega_0$ . An illustration of the circles in the  $\gamma$ -plane that portray regions where attenuation in both local and remote outputs is feasible is shown in figure 3.1. It can be seen that the centre of circle representing local vibration attenuation has a unit radius. The locus of its centre varies with frequency and is not fixed at a point unlike the original geometric method shown in figure 2.1.

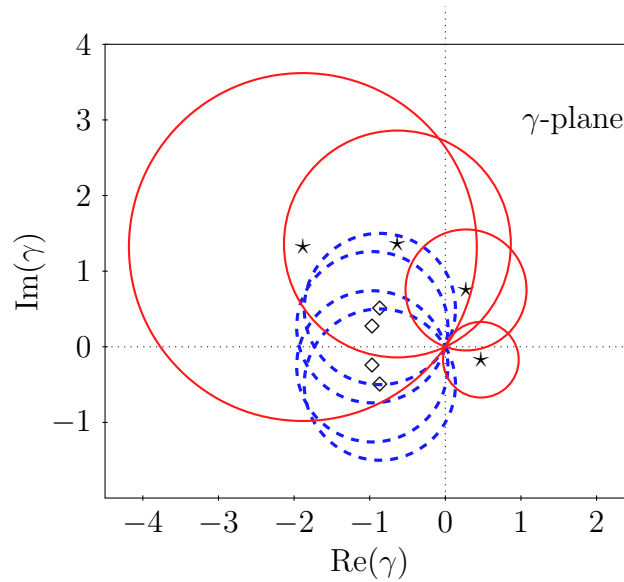


Figure 3.1: The constraint regions for discrete frequencies in  $\gamma$ -plane which signify reduction in output at local (dashed) and remote (solid) points and their centres that represent maximum attenuation at local ( $\diamond$ ) and remote ( $\star$ ) points

If the disturbance is a broadband frequency excitation in a certain known frequency range  $[\omega_L, \omega_H]$  then the circles given by inequalities (3.7) and (3.9) are plotted at several discrete frequencies in this frequency band. The selected optimal values for the design freedom  $\gamma$  at regular intervals of frequency in the excitation frequency band  $[\omega_L, \omega_H]$  is interpolated by a stable transfer function  $\gamma(j\omega)$  and the controller is now implemented

as (3.11).

$$k(j\omega) = -\frac{\gamma(j\omega)}{[1 + \gamma(j\omega) B_{cc}(j\omega)] \hat{g}_{cc}(j\omega)} \quad (3.11)$$

Comparing controller equation (3.11) with (2.16) it can be seen that the RHP zeros of the local control transfer function do not form the poles of the compensator and as  $\gamma(j\omega)$  is a stable transfer function by design, the compensator itself can be stabilised subject to conditions listed in section 3.4.

### 3.3 Robust Performance

#### 3.3.1 Control Spillover and Observation Spillover

The model of any structural or mechanical system that is continuous or has a very high number of degrees of freedom is normally truncated beyond a certain number of modes for ease of computation. The controller is designed based on the lower order approximation of the original system. This approximation has implications on the stability of the closed loop system [Fuller et al., 1997]. The response of any distributed parameter system can be described by a partial differential equation

$$m(x) \frac{\partial^2 q(x, t)}{\partial t^2} + c \frac{\partial q(x, t)}{\partial t} + kq(x, t) = f(x, t) \quad (3.12)$$

where  $q(x, t)$  is the displacement at location  $x$  and time  $t$ ,  $m(x)$  is the mass distribution,  $c$  and  $k$  are the damping and stiffness respectively. The deflection of such a structure can be described in terms of the mode shape functions  $\psi(x)$  and modal amplitude  $\eta(t)$  as

$$q(x, t) = \sum_{k=1}^{\infty} \psi_{xk} \eta_k(t) \quad (3.13)$$

The measurement at a point is the summation of infinitely many modes that occur at different frequencies. In practice, only the first  $N$  modes are considered for control design. The measurement is split into dominant modes that significantly contribute to the overall response and the residual modes as

$$q(x, t) = \sum_{k=1}^N \psi_{xk} \eta_k(t) + \sum_{k=N}^{\infty} \psi_{xk} \eta_k(t) \quad (3.14)$$

Similarly, any force  $f_y$  at a point  $y$  on the structure relates to the modal force component  $f^m$  as

$$f^m = \sum_{k=1}^N \psi_{yk} f_y + \sum_{k=N}^{\infty} \psi_{yk} f_y \quad (3.15)$$

The truncation of residual modes for control design purpose leads to the following approximations

$$f^m \approx \sum_{k=1}^N \psi_{yk} f_y \quad (3.16)$$

and

$$q(x, t) \approx \sum_{k=1}^N \psi_{xk} \eta_k(t) \quad (3.17)$$

The approximation given by (3.16) neglects the excitation of the residual set of modes. This is known as Control Spillover. Similarly, the approximation given by (3.17) neglects the information about the residual modes in the actual measurement. This is known as Observation Spillover. The presence of both control spillover and observation spillover can lead to instabilities in the closed loop system.

Additionally, the actuator dynamics can have a lightly damped resonance frequency and if neglected in the design and the control signal has high amplitude near this frequency, it can lead to instability. The accuracy of measurements provided by the sensor which is fed back to the controller also affects the stability robustness. This depends on many factors such as sensor attachment on the surface, rigidity of host structure, environment noise etc. [Ewins, 2000]. The signal to noise ratio is generally much lower at higher frequency and so it is more susceptible to amplification of noise at these frequencies.

### 3.3.2 Control Design for Robust Performance

The uncertainties in the plant model due to truncation of higher order modes can lead to instabilities. By design the natural frequencies of the neglected modes are usually well above the bandwidth of the problematic disturbance excitation. Also, the uncertainty due to sensor limitations are prevalent at high frequencies. The controller (3.11) derived in section 3.2 will amplify measurement noise in the closed loop system if it has high gain at those frequencies. The effect of low signal to noise ratio on the mea-

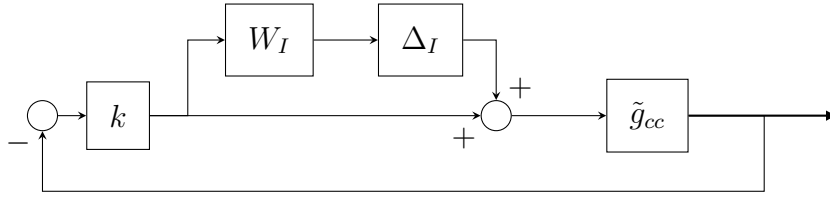


Figure 3.2: Feedback system with multiplicative uncertainty

measurements and truncation of high frequency modes can be represented as a frequency dependent uncertainty and the robust stability conditions can be determined using upper limit values on uncertainty [Skogestad and Postlethwaite, 2005].

The dynamic uncertainty for a nominal plant model  $\tilde{g}_{cc}(j\omega)$  is shown in figure 3.2.  $\Delta_I$  is any stable transfer function such that  $\|\Delta_I\|_\infty \leq 1$  and  $W_I(j\omega)$  denotes the frequency dependent magnitude of uncertainty. The system is robustly stable if the set of all possible perturbed plant models are stable. This can be verified using the Nyquist stability criterion for the set of all perturbed plant models. The nyquist plot of this set of perturbed plant models can be represented as discs of radius  $|W_I(j\omega)\tilde{g}_{cc}(j\omega)k(j\omega)|$  centred on the nyquist contour of the open loop nominal model transfer function  $\tilde{g}_{cc}(j\omega)k(j\omega)$ . At every frequency this disc should avoid the point  $-1$  for robust stability. This can be achieved if the distance from  $-1$  to  $\tilde{g}_{cc}(j\omega)k(j\omega)$  is greater than the radius of the disc  $|W_I(j\omega)\tilde{g}_{cc}(j\omega)k(j\omega)|$  which is determined by

$$|W_I(j\omega)\tilde{g}_{cc}(j\omega)k(j\omega)| < |1 + \tilde{g}_{cc}(j\omega)k(j\omega)|, \quad \forall\omega \quad (3.18)$$

$$\left| \frac{\tilde{g}_{cc}(j\omega)k(j\omega)}{1 + \tilde{g}_{cc}(j\omega)k(j\omega)} \right| < \left| \frac{1}{W_I(j\omega)} \right|, \quad \forall\omega \quad (3.19)$$

$$|T(j\omega)| < \left| \frac{1}{W_I(j\omega)} \right|, \quad \forall\omega \quad (3.20)$$

Since the magnitude of the complementary sensitivity function is equivalent to the magnitude of the design freedom parameter transfer function  $\gamma(j\omega)$

$$|\gamma(j\omega)B_{cc}(j\omega)| < \left| \frac{1}{W_I(j\omega)} \right|, \quad \forall\omega \quad (3.21)$$

The magnitude of all pass transfer function is unity at all frequencies

$$|B_{cc}(j\omega)| = 1, \quad \forall \omega$$

so the expression (3.21) gives an upper bound on the magnitude of  $\gamma(j\omega)$ . A controller implemented in terms of  $\gamma(j\omega)$  that satisfies (3.21) will ensure robustness to unmodelled dynamics. The uncertainty increases at higher frequencies, therefore  $W_I(j\omega)$  can be assumed to have low magnitude at lower frequencies but high magnitude at higher frequencies.  $\gamma$  values for vibration attenuation purposes are only selected for discrete frequencies in the disturbance excitation frequency bandwidth which is mostly in the low frequency region, so the gain of the complementary sensitivity function is not ensured to roll-off at high frequencies. Therefore this may lead to a deterioration in the performance at out of bound frequencies. It is necessary to roll-off the controller gain at high frequencies so that the system is made robust to uncertainties. Assuming that the identified model of the local path transfer function  $\hat{g}_{cc}(j\omega)$  has 2 excess poles then it is seen from controller equation (3.11) that the design parameter transfer function  $\gamma(j\omega)$  should have atleast 4 excess poles in order to have 2 excess poles in the controller transfer function  $k(j\omega)$ . By giving careful consideration to the tuning and interpolation of  $\gamma(j\omega)$  a refined controller with excess poles can be obtained.

A systematic procedure to achieve gain roll-off after an appropriate cut-off frequency can be incorporated into the controller implementation itself. At frequencies within the disturbance bandwidth the optimal  $\gamma$  points are selected from inside circles (3.7) and (3.9). But at high frequencies, the robust stability condition in (3.21) dictates that  $\gamma(j\omega)$  be close to the origin in the  $\gamma$ -plane. This can be achieved using a low pass filter in series with the controller so that  $\tilde{g}_{cc}(j\omega)k(j\omega)$  rolls off at least as fast as  $\tilde{g}_{cc}(j\omega)$ . A low pass filter following the controller would roll-off the gain at high frequency but it will also affect the phase in the disturbance frequency region. This has the effect of rotating the  $\gamma$  points in the  $\gamma$ -plane possibly resulting in  $\gamma$  points outside circles (3.7) and (3.9) and hence the intended vibration attenuation will not be achieved. But if a low pass filter is incorporated in the  $\gamma$  point selection then the effect of phase changes on the  $\gamma$  points would be accounted for in the controller implementation itself. The local and remote vibration attenuation conditions from (3.7) and (3.9) are therefore modified to

(3.22) and (3.24), respectively

$$|\gamma(j\omega) + U_c(j\omega)| < |U_c(j\omega)| \quad (3.22)$$

where

$$U_c(j\omega) = \frac{1}{W_\gamma(j\omega)B_{cc}(j\omega)} \quad (3.23)$$

$$|\gamma(j\omega) + U_p(j\omega)| < |U_p(j\omega)| \quad (3.24)$$

where

$$U_p(j\omega) = \frac{\hat{g}_{cc}(j\omega)g_{pp}(j\omega)}{W_\gamma(j\omega)\tilde{g}_{cp}(j\omega)\tilde{g}_{pc}(j\omega)} \quad (3.25)$$

and  $W_\gamma(j\omega)$  is any chosen frequency weighting function that has low gain at frequencies where the percentage of uncertainty is high due to model truncation or sensor noise. The magnitude of  $W_\gamma(j\omega)$  is close to unity in the disturbance frequency bandwidth therefore it has negligible influence on the size of circles but only affects the rotation of its centre. The controller from (3.11) is now implemented as (3.26) which satisfies the robust stability condition in (3.21).

$$k(j\omega) = \frac{-\gamma(j\omega)W_\gamma(j\omega)}{[1 + \gamma(j\omega)B_{cc}(j\omega)W_\gamma(j\omega)]\hat{g}_{cc}(j\omega)} \quad (3.26)$$

Additionally, the actuator dynamics can cause performance degradation or stability issues in certain applications. So, it is preferable to have low gain around the actuator resonance in order to avoid stroke and force saturation effects which usually occur in the low frequency region. Then  $W_\gamma(j\omega)$  can be a bandpass filter to suppress spillover at low and high frequencies. It should be noted that for nominal performance  $W_\gamma(j\omega)$  should have unity gain within the disturbance frequency bandwidth. Then the controller, implemented as (3.26), will achieve both nominal performance and robust stability.

### 3.4 Stability Analysis

The controller in (3.26) is equivalent to the original geometric-based controller in (2.16) if the local transfer function is minimum phase and no weighting filter is used, i.e.  $B_{cc}(j\omega)W_\gamma(j\omega) = 1$ , and then the closed loop stability conditions follow from [Wang and Daley, 2010]. However, for the non-minimum phase condition, the centre of the

circle representing local vibration attenuation is no longer fixed at  $-1$  for all frequencies and the mapping of its centre in the  $\gamma$ -plane also depends on the frequency response of  $B_{cc}(j\omega)W_\gamma(j\omega)$  which has to be taken into account in order to ensure closed loop stability. The conditions for the closed loop stability and controller stability on the selection of  $\gamma$  points is considered in this section.

Rearranging controller equation (3.26) to form a relation between the design freedom parameter and the complementary sensitivity function

$$\gamma(j\omega)B_{cc}(j\omega)W_\gamma(j\omega) = \frac{-\tilde{g}_{cc}(j\omega)k(j\omega)}{1 + \tilde{g}_{cc}(j\omega)k(j\omega)}$$

It can be observed that since  $B_{cc}(j\omega)W_\gamma(j\omega)$  is stable, selecting  $\gamma$  points as the mapping of a stable function (in a similar fashion to the approach proposed by Wang and Daley [2010]) guarantees closed loop stability.

Since  $\hat{g}_{cc}(j\omega)$  has no RHP zero(s), a controller given by (3.26) is stable if  $\gamma(j\omega)$  is a stable transfer function and the Nyquist contour of  $\gamma(j\omega)B_{cc}(j\omega)W_\gamma(j\omega)$  does not enclose the  $-1$  point<sup>1</sup>. This has implications near the resonant frequency of a flexural mode. As will be shown in section 5.3 of chapter 5, the optimal  $\gamma$  point for vibration attenuation close to a resonant frequency of the structure approaches  $[-B_{cc}(j\omega)W_\gamma(j\omega)]^{-1}$ . This means that when a controller is to be designed for attenuation near resonant frequencies the polar plot of  $\gamma(j\omega)B_{cc}(j\omega)W_\gamma(j\omega)$  approaches the critical point and would therefore have very low gain and phase margins close to this frequency. Hence, when  $\gamma$  points are to be selected for attenuation near a resonant frequency, which will usually be the case, then it becomes important to define some additional constraints so that  $\gamma(j\omega)B_{cc}(j\omega)W_\gamma(j\omega)$  in the disturbance frequency bandwidth does not encircle the critical point.

The polar plot of  $\gamma(j\omega)B_{cc}(j\omega)W_\gamma(j\omega)$  will not enclose the  $-1$  point and hence the controller will be stable if, at the phase crossover frequency  $\omega_{pc}$  (i.e. when  $\text{Im}(\gamma(j\omega)B_{cc}(j\omega)W_\gamma(j\omega)) = 0$ ), the condition  $\text{Re}(\gamma(j\omega)B_{cc}(j\omega)W_\gamma(j\omega)) > -1$  is satisfied. The frequency response of  $\gamma(j\omega)B_{cc}(j\omega)W_\gamma(j\omega)$  at the phase crossover frequency can be written in cartesian form as the products of the frequency response of  $\gamma(j\omega)$  and  $B_{cc}(j\omega)W_\gamma(j\omega)$  evaluated at  $\omega_{pc}$  as

---

<sup>1</sup>It should be noted that the Nyquist contour of open loop system is normally used for closed loop stability analysis. However, this is an unconventional use of Nyquist of the closed loop system to analyse the RHP zeros in the denominator of the controller, which is per the consequence of the Cauchy's argument principle.

$$\begin{aligned} \gamma(j\omega)B_{cc}(j\omega)W_\gamma(j\omega) = \\ [\text{Re}(\gamma(j\omega)) + j\text{Im}(\gamma(j\omega))][\text{Re}(B_{cc}(j\omega)W_\gamma(j\omega)) + j\text{Im}(B_{cc}(j\omega)W_\gamma(j\omega))] \end{aligned} \quad (3.27)$$

Multiplying the terms inside the brackets and rearranging as the summation of real and imaginary parts

$$\begin{aligned} \gamma(j\omega)B_{cc}(j\omega)W_\gamma(j\omega) = \\ [\text{Re}(\gamma(j\omega))\text{Re}(B_{cc}(j\omega)W_\gamma(j\omega)) - \text{Im}(\gamma(j\omega))\text{Im}(B_{cc}(j\omega)W_\gamma(j\omega))] \\ + j[\text{Re}(\gamma(j\omega))\text{Im}(B_{cc}(j\omega)W_\gamma(j\omega)) + \text{Im}(\gamma(j\omega))\text{Re}(B_{cc}(j\omega)W_\gamma(j\omega))] \end{aligned} \quad (3.28)$$

At the phase crossover frequency  $\text{Im}(\gamma(j\omega)B_{cc}(j\omega)W_\gamma(j\omega)) = 0$ , therefore equating the imaginary term on the right hand side of (3.28) to zero gives

$$\text{Re}(\gamma(j\omega))\text{Im}(B_{cc}(j\omega)W_\gamma(j\omega)) + \text{Im}(\gamma(j\omega))\text{Re}(B_{cc}(j\omega)W_\gamma(j\omega)) = 0 \quad (3.29)$$

The controller is stable if at the phase crossover frequency  $\text{Re}(\gamma(j\omega)B_{cc}(j\omega)W_\gamma(j\omega)) > -1$ , which from the real term of (3.28) can be stated as

$$\text{Re}(\gamma(j\omega))\text{Re}(B_{cc}(j\omega)W_\gamma(j\omega)) - \text{Im}(\gamma(j\omega))\text{Im}(B_{cc}(j\omega)W_\gamma(j\omega)) > -1 \quad (3.30)$$

Substituting  $\text{Im}(\gamma(j\omega))$  from (3.29) in (3.30) gives

$$\text{Re}(\gamma(j\omega)) > \frac{-\text{Re}(B_{cc}(j\omega)W_\gamma(j\omega))}{[\text{Re}(B_{cc}(j\omega)W_\gamma(j\omega))]^2 + [\text{Im}(B_{cc}(j\omega)W_\gamma(j\omega))]^2} \quad (3.31)$$

The Blaschke product  $B_{cc}(j\omega)$  has unity magnitude at all frequencies and the weighting filter is chosen such that in the design frequency bandwidth it does not affect the magnitude

$$|B_{cc}(j\omega)W_\gamma(j\omega)| = |B_{cc}(j\omega)| |W_\gamma(j\omega)| = 1. \quad \omega \in [\omega_L, \omega_H]$$

The stability consideration is also not critical because of small gain outside of this frequency band due to the band pass filter. Therefore, (3.31) reduces to

$$\operatorname{Re}(\gamma(j\omega)) > -\operatorname{Re}(B_{cc}(j\omega)W_\gamma(j\omega)) \quad (3.32)$$

Similarly, substituting  $\operatorname{Re}(\gamma(j\omega))$  from (3.29) in (3.30) leads to the expression

$$\operatorname{Im}(\gamma(j\omega)) < \operatorname{Im}(B_{cc}(j\omega)W_\gamma(j\omega)) \quad (3.33)$$

A controller given in (3.26) will therefore be both stable and stabilising if the  $\gamma$  points are selected from a mapping of a stable transfer function  $\gamma(j\omega)$  and either of the conditions (3.32) or (3.33) is satisfied.

## 3.5 Numerical example

In this section the new geometric based approach for the design of a stable remote vibration controller is verified using simulation results for a flexible beam. The difficulty arising in the synthesis of a stable controller for vibration attenuation at resonance is clearly evident with this example.

### 3.5.1 Model of beam

The response of a slender beam, assuming Euler Bernoulli beam theory for a simply supported boundary condition, is considered in order to illustrate the remote vibration control technique described in section 3.3.2. Finite element modelling [Petyt, 2010] is used to construct the mass and stiffness matrices for a beam with the dimensions and material properties given in Table 3.1. For convenience Rayleigh damping is assumed for the beam model. The beam is subdivided into 10 elements and two degrees of freedom are associated with each node (end connection) of a single beam element. The two degrees of freedom associated with each point are the angular rotation and vertical translational displacement. The mass, stiffness and damping matrices for this model of the beam is provided in Appendix B. The control force acts as a discrete translational force at a distance of 0.2 m from one end of the beam while the feedback sensor measures translational displacement at a distance of 0.1 m as shown in figure 2.2. This non-collocated arrangement will impart NMP characteristics on the local control path

Parameter	Value
Length	1 m
Cross section	$2.0 \times 2.0$ cm
Mass Density	$7850 \text{ kg/m}^3$ (mild steel)
Young's modulus of elasticity	$21 \times 10^{10} \text{ N/m}^2$

Table 3.1: Properties of the beam considered for simulation study in section 3.5

transfer function  $\tilde{g}_{cc}(j\omega)$ . The primary excitation acts as a discrete translational force at a distance of 0.9 m from the end of the beam. The first bending mode of the beam occurs at 47 Hz and the controller will be designed to attenuate vibration at the local and remote points for excitation around this frequency.

### 3.5.2 Selection of optimal $\gamma$

A controller targeting attenuation of vibration for the excitation frequency range 42 Hz to 52 Hz is designed for the beam. Although the controller will be implemented on a known model of the structure, robustness to high frequency dynamics will be included as part of the design procedure to illustrate the practical applicability of this method. The frequency weighting terms have to be selected such that the closed loop magnitude rolls off at high frequencies and also the amplitude is minimum at low frequencies which might be necessary to prevent excitation of actuator dynamics. Therefore, an 8<sup>th</sup> order bandpass filter with lower cut-off frequency of 14 Hz and a higher cut-off frequency of 57 Hz is chosen as  $W_\gamma(j\omega)$  to account for suppression of spillover at both low and high frequencies.

The circles corresponding to local and remote vibration reduction as per (3.22) and (3.24) are computed for 30 discrete frequencies within the disturbance bandwidth as shown in figure 3.3. The circles are stacked on top of each other with increasing frequency depicted as a cylinder in a three-dimensional plot. The locus of the centre of the circles corresponding to a reduction at the local point  $U_c(j\omega_i)$  is denoted by  $\diamond$ , and the equivalent locus for the remote point  $U_p(j\omega_i)$  is denoted by  $\star$ . Based on the required vibration attenuation at the local and remote points, a set of optimal values denoted as  $\gamma_i$  is selected at each discrete frequency  $\omega_i$ . In order to achieve the maximum reduction at the remote point, the set of optimal  $\gamma$  points is selected as  $U_p(j\omega_i)$ . The next step

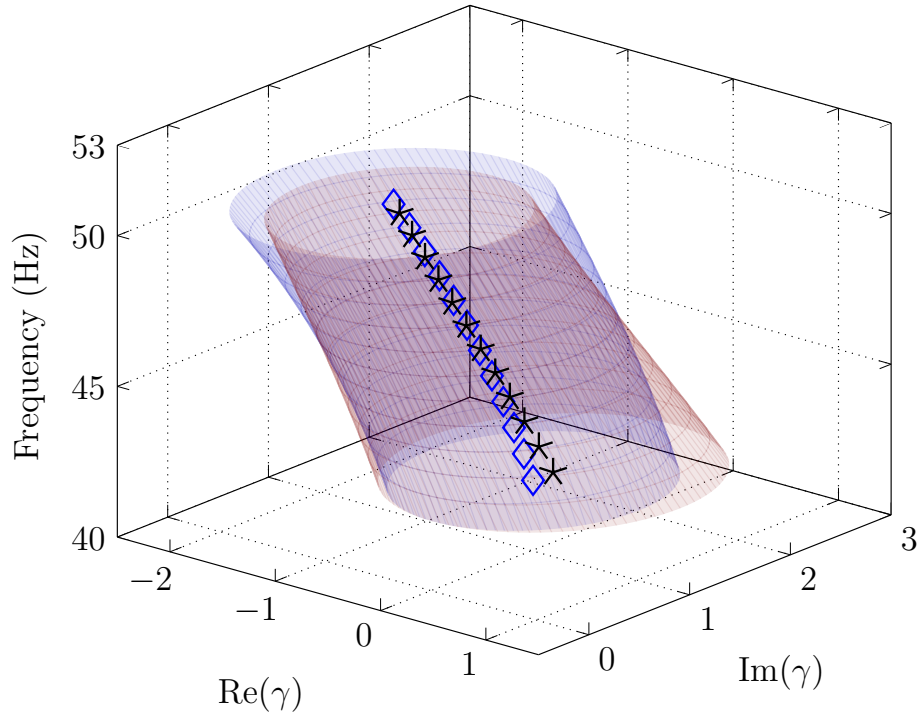


Figure 3.3: Circles representing reduction in vibration at the local (blue) and remote (red) points on the beam,  $U_c(j\omega_i)$  -  $\diamond$ ,  $U_p(j\omega_i)$  -  $\star$

is to determine a stable transfer function that takes these optimal values for the design freedom parameter at discrete frequencies  $\omega_i$ .

### 3.5.3 Interpolation of $\gamma$ values

The set of optimal values  $\gamma_i$  can be interpolated by a stable transfer function using any suitable curve fitting technique. The Nevanlinna Pick interpolation technique is well suited as it allows determination of a stable transfer function and provides extra degrees of freedom. It is stated as follows [Delsarte et al., 1981]: given  $n$  distinct points  $s_1, \dots, s_n$  in the right half plane  $\Pi^+$  and a collection of complex numbers  $\xi_1, \dots, \xi_n$ , determine a transfer function  $h(s)$  that is analytic in  $\Pi^+$  with

$$\sup |h(s)| \leq 1$$

### 3.5. NUMERICAL EXAMPLE

such that  $h(s_i) = \xi_i$  for all  $i = 1, \dots, n$ . The solution of this interpolation problem exists if and only if the associated Pick matrix (3.34) is positive definite.

$$P = \left[ \frac{1 - \xi_k \bar{\xi}_l}{s_k + \bar{s}_l} \right]_{k,l=1}^n \quad (3.34)$$

The points  $s_i$  according to the above theorem should strictly lie in the right half plane, whereas the set of optimal selected values for the design parameter  $\gamma$  have to be interpolated on the imaginary  $j\omega$  axis. The frequency points are shifted into the RHP using Lemma 2 in [Ferrerres and Puyou, 2005] and the original problem is transformed as follows: for the optimal  $\gamma$  data values at  $n$  discrete frequencies  $\omega_i$ , for  $i = 1, \dots, n$ , a stable transfer function  $\gamma(j\omega)$  exists if and only if the associated Pick matrix (3.35) is positive definite.

$$P = \left[ \frac{1 - Z_k \bar{Z}_l}{s_k + \bar{s}_l} \right]_{k,l=1}^n = \left[ \frac{1 - \frac{\gamma_k \bar{\gamma}_l}{M M}}{\sigma + j\omega_k + (\sigma - j\omega_l)} \right]_{k,l=1}^n \quad (3.35)$$

It can be seen from (3.35) that increasing the constant value of non-unitary upper bound  $M$  or decreasing stability margin  $\sigma$  will increase the positiveness of the pick matrix but for a stable controller and good performance at intermediate frequencies,  $M$  and  $\sigma$  values have to be finely tuned. It should be noted that a small value of shift  $\sigma$  will result in interpolated transfer function  $\gamma(j\omega)$  with poles that are close to the imaginary axis. This would cause oscillations between the interpolated frequency points in the frequency response of the identified transfer function leading to gain and phase crossover at intermediate frequencies [Coelho et al., 2002]. As the final  $\gamma$  values at the non-interpolated frequency points may lie outside the (3.22) and (3.24) circles in the  $\gamma$ -plane, closed loop performance will deteriorate. Also, since  $\|\gamma(j\omega)\|_\infty = M$  a large value of  $M$  could result in polar plot of  $\gamma(j\omega)B_{cc}(j\omega)W_\gamma(j\omega)$  to encircle the  $-1$  point. A good tuning rule would be to iteratively increase the value of  $M$  so that the pick matrix is positive definite for every specific value of  $\sigma$  until the controller stability condition is violated [Fu, 1991].

The first step in the iterative classical N-P interpolation algorithm is to compute

elements of Fenyves array  $\Omega$ .

$$\Omega_{k,l} = \frac{s_l + \bar{s}_{k-1}}{s_l - s_{k-1}} \frac{\Omega_{k-1,l} - \Omega_{k-1,k-1}}{1 - \Omega_{k-1,l}\bar{\Omega}_{k-1,k-1}}, \quad 2 < k < n, k < l < n \quad (3.36)$$

where  $\Omega_{1,l} = Z_l$ , for  $1 < l < n$ . The next step is to recursively estimate  $Z_1(s)$  from

$$Z_k(s) = \frac{\Omega_{k,k} + Z_{k+1}(s) \frac{s - s_k}{s + \bar{s}_k}}{1 + \bar{\Omega}_{k,k} Z_{k+1}(s) \frac{s - s_k}{s + \bar{s}_k}}, \quad k = n, n-1, \dots, 2, 1 \quad (3.37)$$

If the set of data points  $(s_i, Z_i)$  for interpolation is augmented with its complex conjugate  $(\bar{s}_i, \bar{Z}_i)$ , then a stable bounded real analytic interpolating function is given by

$$\gamma(s) = M \times \frac{1}{2} [Z_1(s + \sigma) + \bar{Z}_1(s + \sigma)]$$

for any arbitrarily selected initial stable bounded analytic function  $Z_{k+1}(s)$  in (3.37).

### 3.5.3.1 Reduced interpolation data set

Each data point used for interpolation adds 4 poles and zeros to the identified  $\gamma(j\omega)$  transfer function. This increases the order of the controller by 4 for every additional  $\gamma_i$  value considered. Therefore, for practical reasons a reduced set of data points should be selected from the complete design set for  $\gamma(j\omega)$  interpolation. If the gradient of optimal points  $\gamma_i$  between two consecutive discrete frequencies is large and a reduced set of points that excludes the intermediate frequency point is used for interpolation, then the frequency response of  $\gamma(j\omega)$  at the intermediate frequency point will differ by a large extent from the optimal value at this frequency. The gradient of the real and imaginary parts of the complete data set,  $(\gamma_i, \omega_i)$ , is denoted as  $\kappa_i$

$$\kappa_i = \frac{\gamma_i - \gamma_{i-1}}{\omega_i - \omega_{i-1}} \quad (3.38)$$

The phase of  $W_\gamma(s)$  affects the gradient of  $\kappa$  and it depends on the order of the filter and also the cut off frequency of the filters as shown in figure 3.4. More interpolation points need to be considered in the corresponding frequency intervals when  $\frac{d(\text{Re}(\kappa))}{d\omega}$

and  $\frac{d(\text{Im}(\kappa))}{d\omega}$  are large, which is the case when the upper and lower cut-off frequencies are nearer to the disturbance frequency bandwidth. As can be seen in figure 3.4, for the selected filter with low and high cut-off frequencies of 14 Hz and 57 Hz, respectively, the gradient of  $\text{Re}(\kappa)$  and  $\text{Im}(\kappa)$  at frequencies higher than 48 Hz is small.

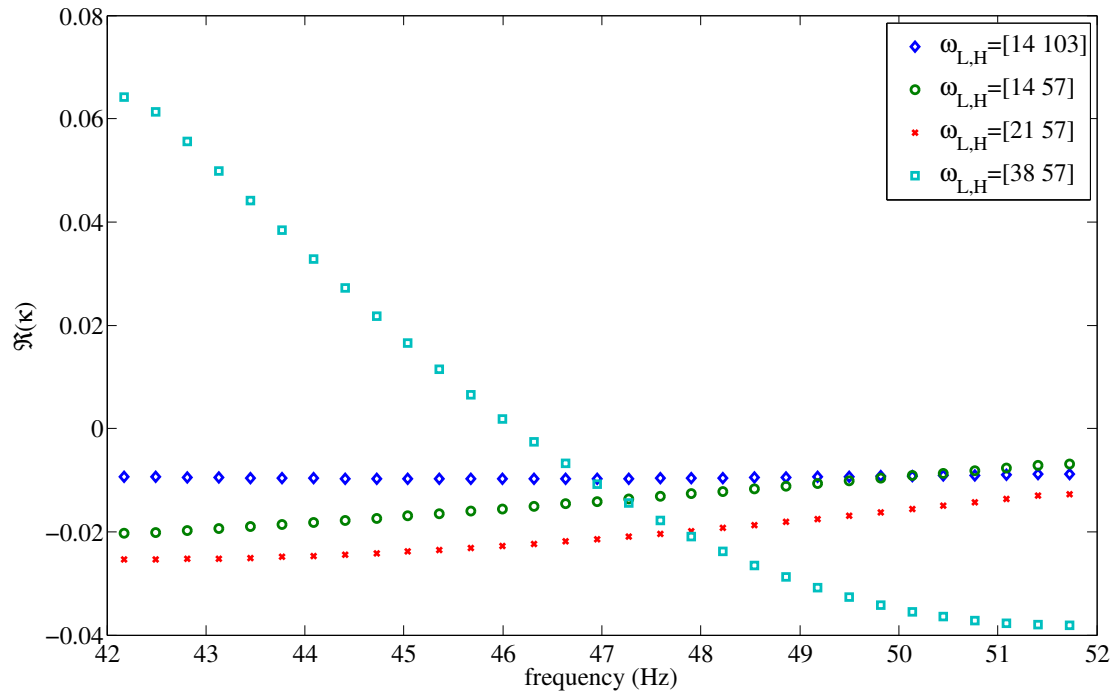
#### 3.5.3.2 Modification of $\gamma_i$ to satisfy controller stability

Although increasingly large values of  $\sigma$  give a better approximation at intermediate frequencies, the values of  $M$  that ensure positivity of the pick matrix for these  $\sigma$  values would be large enough to cause the nyquist locus of  $\gamma(j\omega)B_{cc}(j\omega)W_\gamma(j\omega)$  to encircle the critical point. To illustrate this point, the frequency response of the  $\gamma(j\omega)$  transfer function interpolated using  $\sigma = 50$  (large) shows good approximation at intermediate frequencies in figure 3.5, but the corresponding nyquist plot of  $\gamma(j\omega)B_{cc}(j\omega)W_\gamma(j\omega)$  encircles  $-1$  as shown in figure 3.6. It is seen that for  $\sigma = 6.5$  the nyquist plot of  $\gamma(s)B_{cc}(s)W_\gamma(s)$  crosses the real axis to the left of  $-1$  in the immediate vicinity of the disturbance frequency band as shown in figure 3.7. This is because absolute value of optimal  $\gamma$  data points is greater than 1 at some discrete frequencies  $\omega_i$ . In order to use  $\sigma$  value large enough to give satisfactory response at intermediate frequencies whilst simultaneously satisfying controller stability conditions, optimal  $\gamma$  values are slightly modified such that  $\gamma(j\omega_i)B_{cc}(j\omega_i)W_\gamma(j\omega_i)$  at discrete disturbance frequencies only lie to the right of  $-1$ . This modified set of points  $\tilde{\gamma}_i$  is used for interpolation. The nyquist plot of  $\gamma(s)B_{cc}(s)W_\gamma(s)$  for transfer function  $\gamma(j\omega)$  obtained by interpolating a reduced set of  $\tilde{\gamma}_i$  in figure 3.8 shows that the critical point is not enclosed and hence the controller is stable. The final operating  $\gamma$  points from the FRF of  $\gamma(j\omega)$  at  $\omega_i$  and  $\tilde{\gamma}_i$  is plotted in figure 3.9 for comparison. This shows that the modified optimal  $\gamma$  points lie inside both circles and therefore the overall performance will be similar to that provided by the original optimal  $\gamma$  point selection.

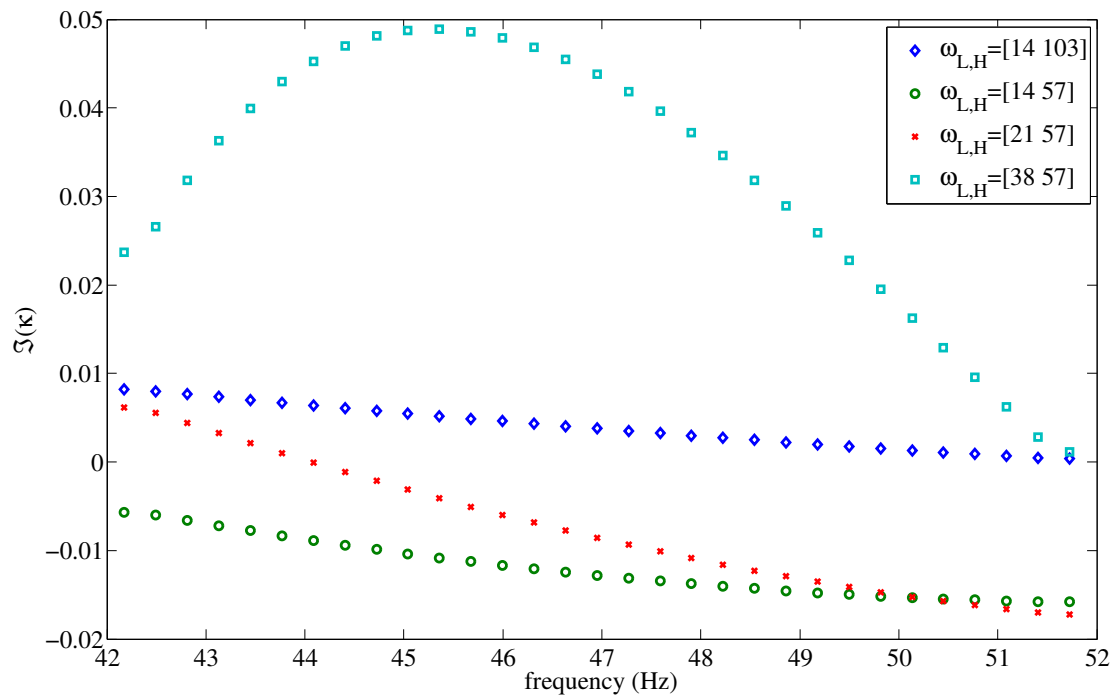
#### 3.5.4 Controller Implementation

The interpolated stable transfer function  $\gamma(j\omega)$  is substituted into (3.26) to obtain a controller  $k(j\omega)$ . The magnitude of the controller rolls-off at higher frequencies due to action of  $W_\gamma(j\omega)$  as shown in figure 3.12 and will not excite any unmodelled high fre-

### 3.5. NUMERICAL EXAMPLE



(a)  $\text{Re}(\kappa)$  vs frequency



(b)  $\text{Im}(\kappa)$  vs frequency

Figure 3.4: Variation in  $\kappa$  for different cut on and cut off frequencies of  $W_\gamma(s)$

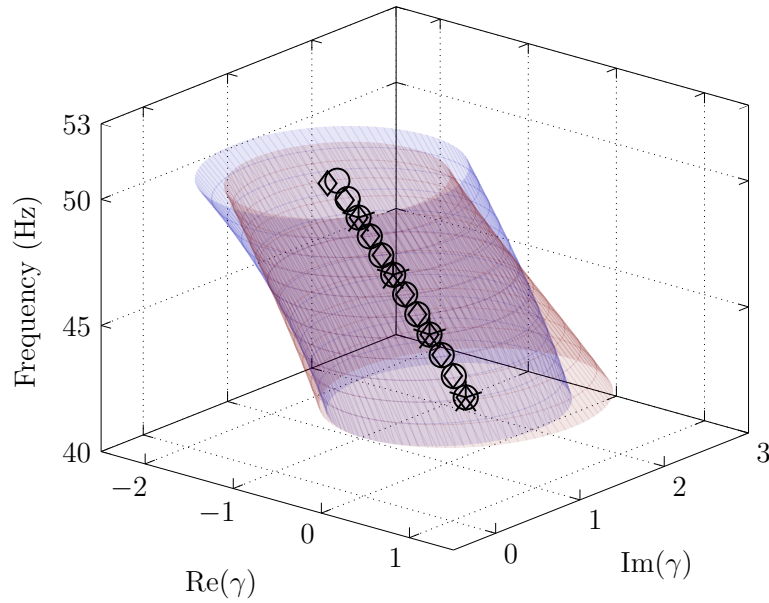


Figure 3.5: Initial set of optimal selected  $\gamma$  values ( $\circ$ ), set of  $\gamma$  values used for interpolation ( $\star$ ), operating  $\gamma$  values shown as  $\diamond$  is the frequency response of identified  $\gamma(j\omega)$ , which is interpolated using a value of  $\sigma = 50$

quency dynamics. The reduction in magnitude of the closed loop FRF from disturbance input to local vibration output shows around 20 dB attenuation as shown in figure 3.10. The corresponding reduction in magnitude from disturbance input to remote vibration output is also 20 dB as shown in figure 3.11.

However, it can be seen in figure 3.11 that a sharp peak is induced at 97 Hz in the closed loop FRF which is originally not present in the open loop case. The controller realisation involves inversion of the minimum phase counterpart of the local control path FRF. The antiresonance anti-peaks in the local control path FRF appears as a peak in the controller FRF which results in sharp peaks in the closed loop FRF between disturbance input and remote output. This peak can be suppressed by using a notch filter in series with the controller, as illustrated in section 4.5.2 of chapter 4. Alternatively, low gain of  $\gamma(j\omega)$  at this frequency can suppress this peak in controller FRF. If this antiresonant frequency is close to the design frequency band then a high order filter  $W_\gamma(j\omega)$  is necessary to achieve steep roll-off of gain in  $\gamma(j\omega)$ . But it is easier to define few additional values for the design freedom parameter near the origin to ensure small magnitude of  $\gamma(j\omega)$  at this frequency.

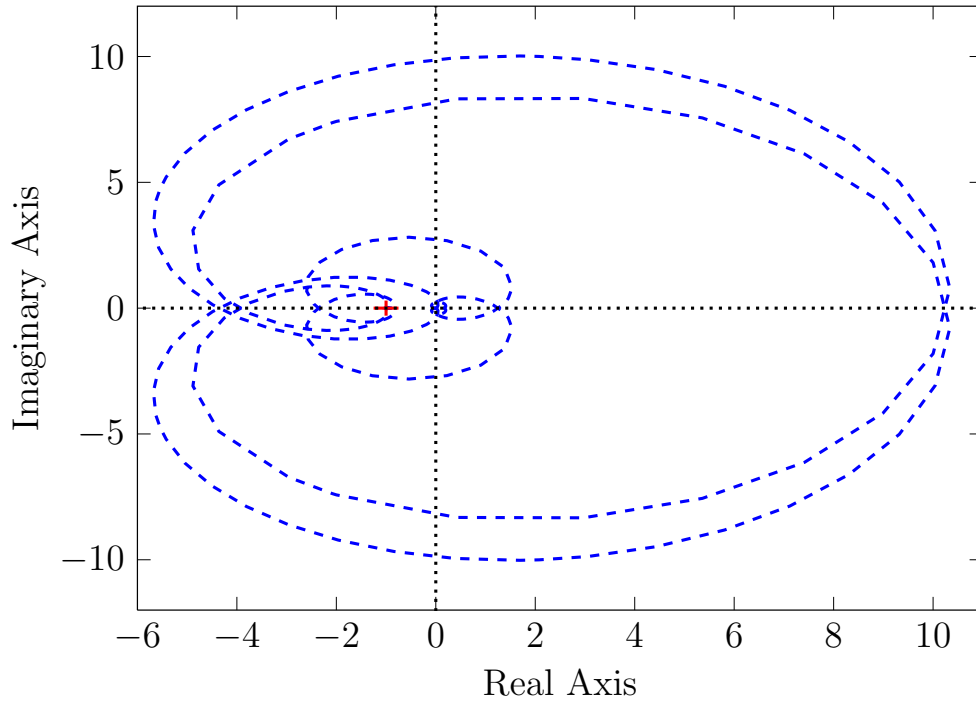


Figure 3.6: Nyquist diagram of  $\gamma(j\omega)B_{cc}(j\omega)W_\gamma(j\omega)$  for  $\gamma(j\omega)$  interpolated using a value of  $\sigma = 50$

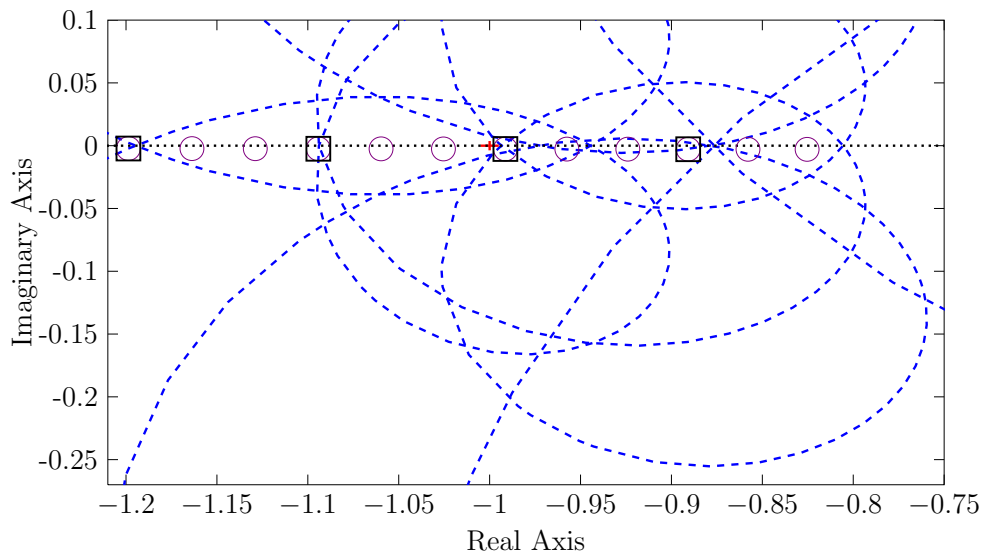


Figure 3.7: Nyquist plot of  $\gamma(s)B_{cc}(s)W_\gamma(s)$  for  $\gamma(j\omega)$  interpolated using a value of  $\sigma = 6.5$ , also shown are the values of  $\gamma(j\omega_i)B_{cc}(j\omega_i)W_\gamma(j\omega_i)$  corresponding to the initial set of optimal selected  $\gamma$  values (○) and its reduced set used for interpolation (□)

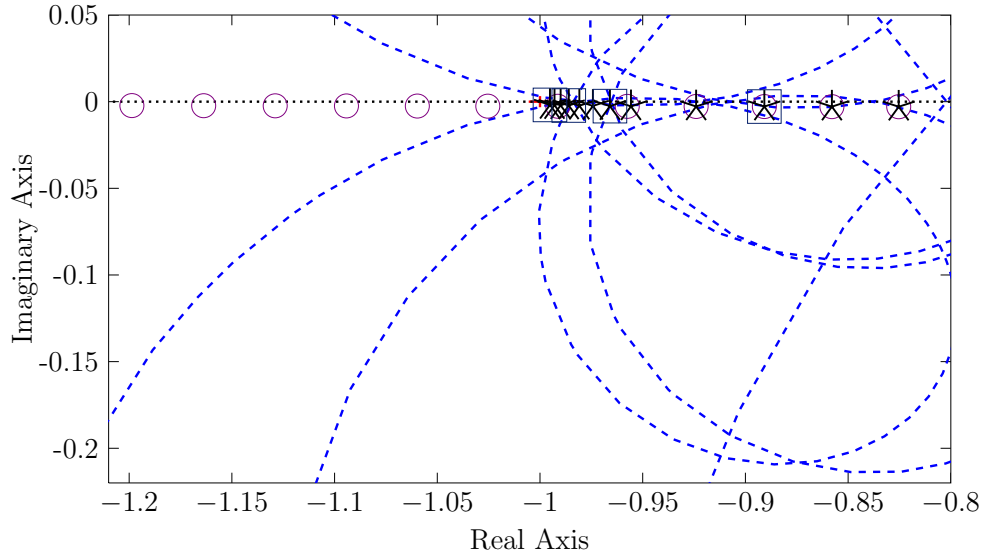


Figure 3.8: Nyquist plot of  $\gamma(s)B_{cc}(s)W_{\gamma}(s)$  for  $\gamma(j\omega)$  interpolated from the modified set of  $\gamma$  data values using a value of  $\sigma = 6.5$  and  $M = 1.54$ , also shown are the values of  $\gamma(j\omega_i)B_{cc}(j\omega_i)W_{\gamma}(j\omega_i)$  corresponding to the initial set of optimal selected  $\gamma$  values (○), modified set of  $\gamma$  values (☆) and its reduced set used for interpolation (□)

### 3.5.5 Alternative Controller Implementation

In the case of lightly damped modes, a slight discrepancy in the  $\gamma$  value at resonance affects the attenuation at this frequency. The inversion of the local control path in the controller implementation will result in very low control action at this resonant frequency if  $\gamma(j\omega)$  does not accurately compensate for it. The frequency response of  $\gamma(j\omega)$  at resonance should lie at the centre of the local vibration reduction circle.

A controller synthesised in terms of the inversion of a modified minimum phase local control path transfer function will not suffer from low gain at resonance. This is achieved by using a local control path transfer function such that the damping at the resonant frequency is increased considerably. The damping of the first resonance of  $\hat{g}_{cc}(j\omega)$  is increased by a factor of 30 and this modified transfer function  $\hat{G}_{cc}(j\omega)$  is used as given in (3.39). The reduction in the closed loop FRF using  $\hat{G}_{cc}(j\omega)$  for controller realisation shows better disturbance attenuation in the local and remote output as shown in figures 3.13 and 3.14. Utilization of a damped model compensates for the errors in interpolation and is manifested as a better magnitude in the controller FRF at the

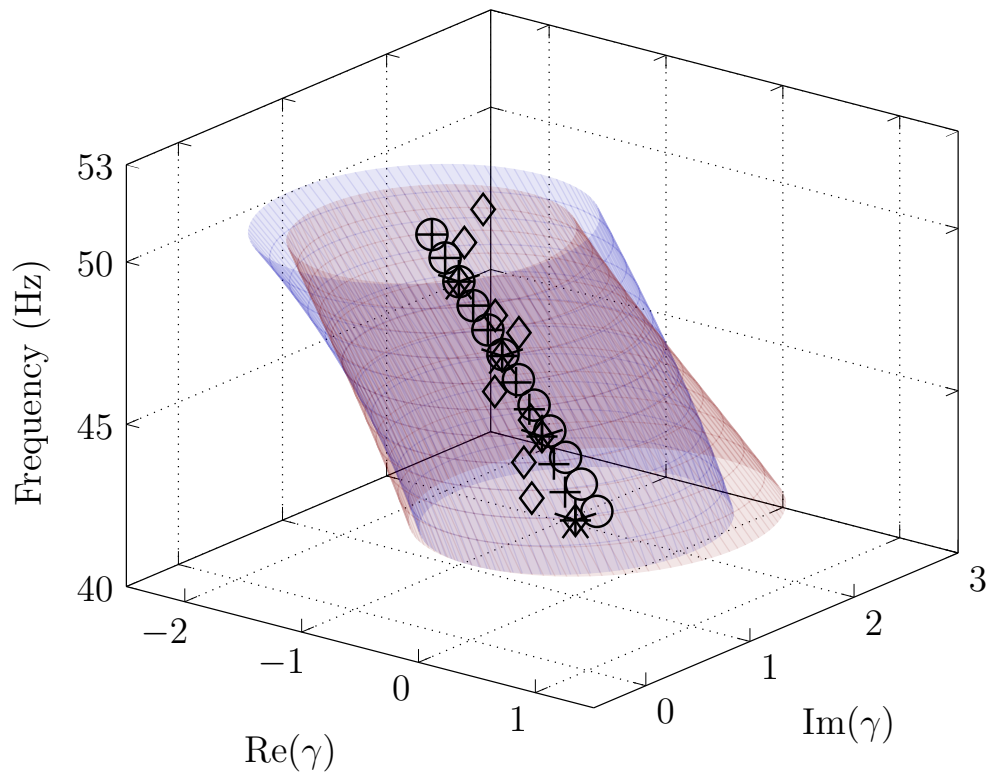


Figure 3.9: Initial set of optimal selected  $\gamma$  values ( $\circ$ ), modified set of  $\gamma$  values ( $+$ ), set of  $\gamma$  values used for interpolation ( $*$ ), final operating  $\gamma$  values shown as  $\diamond$  is the frequency response of identified  $\gamma(j\omega)$ , which is interpolated using a value of  $\sigma = 6.5$  and  $M = 1.54$

### 3.5. NUMERICAL EXAMPLE

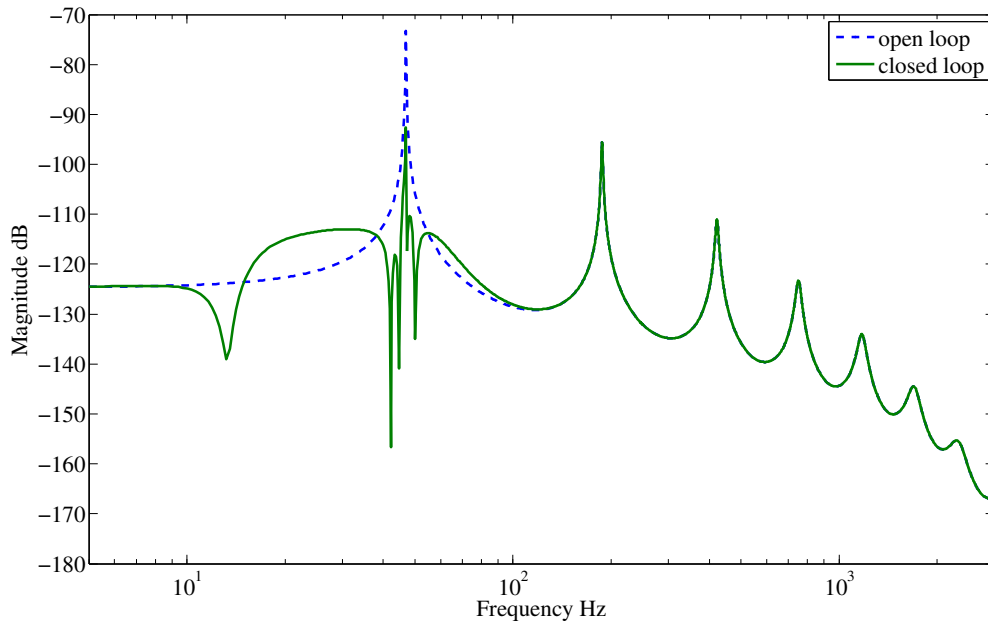


Figure 3.10: Magnitude FRF of primary disturbance input to local sensor with (solid) and without (dashed) feedback control

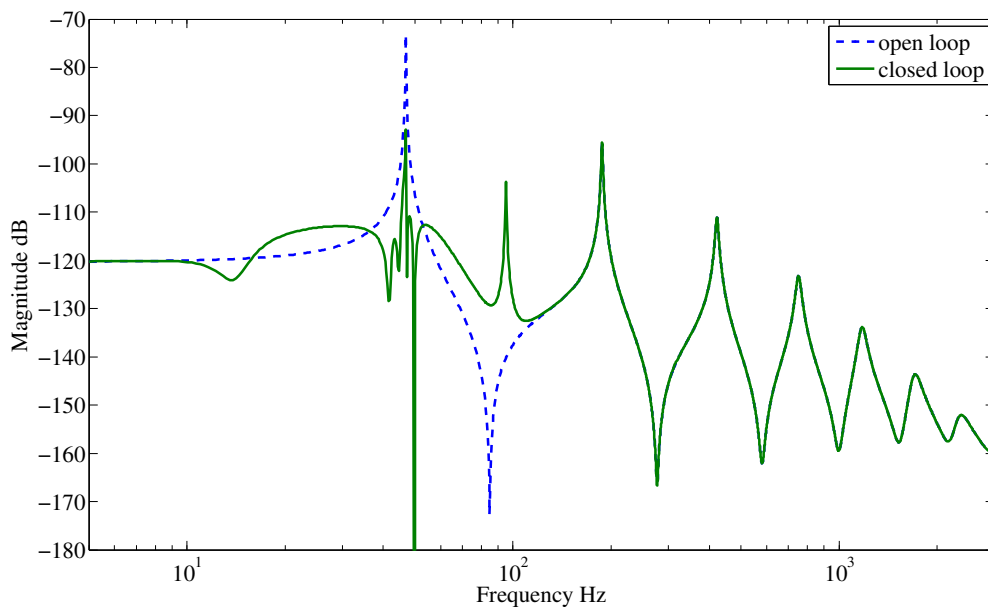


Figure 3.11: Magnitude FRF of primary disturbance input to remote output with (solid) and without (dashed) feedback control

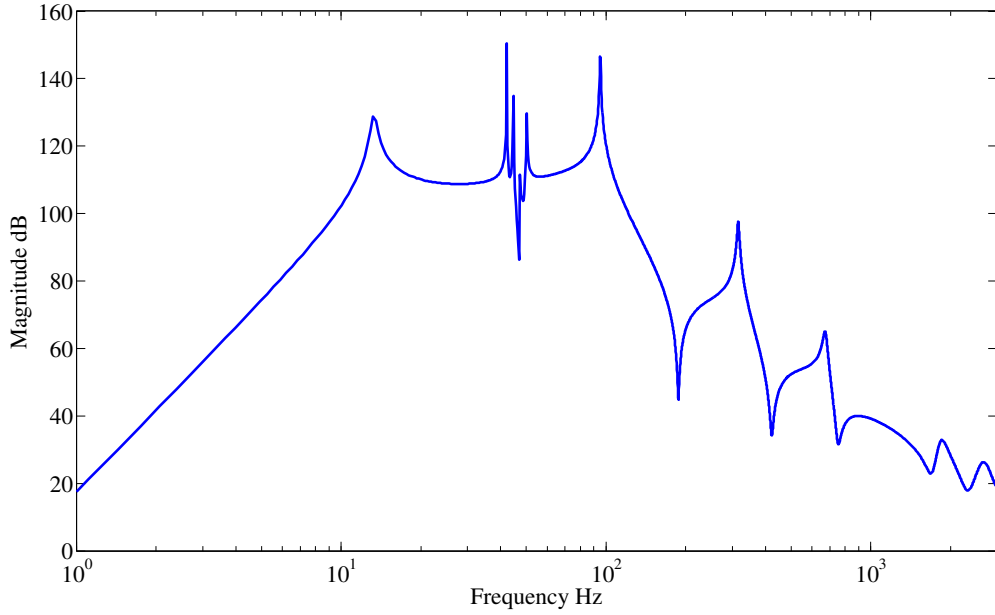


Figure 3.12: Magnitude FRF of controller,  $|k(j\omega)|$

resonant frequency as shown in figure 3.15. It should be noted that this alternative controller implementation in a real-life situation may not always be feasible due to the difficulty in modal parameter estimation. Derivation of modal properties from data-driven models is in itself a vast area of research [Heylen et al., 2006] and so whenever possible the former controller implementation should be realised in the first instance.

$$\hat{k}(j\omega) = \frac{-\gamma(j\omega)W_\gamma(j\omega)}{[1 + \gamma(j\omega)B_{cc}(j\omega)W_\gamma(j\omega)]\hat{G}_{cc}(j\omega)} \quad (3.39)$$

### 3.6 Summary

A modified geometric control design methodology for the control of remote vibration has been presented in this chapter. It yields a stable controller even when the local control path transfer function is non-minimum phase. This control design relaxes the requirement for a truly collocated sensor and actuator pair, which is often impractical in real situations. It is seen that neither the sensor and actuator dynamics nor the

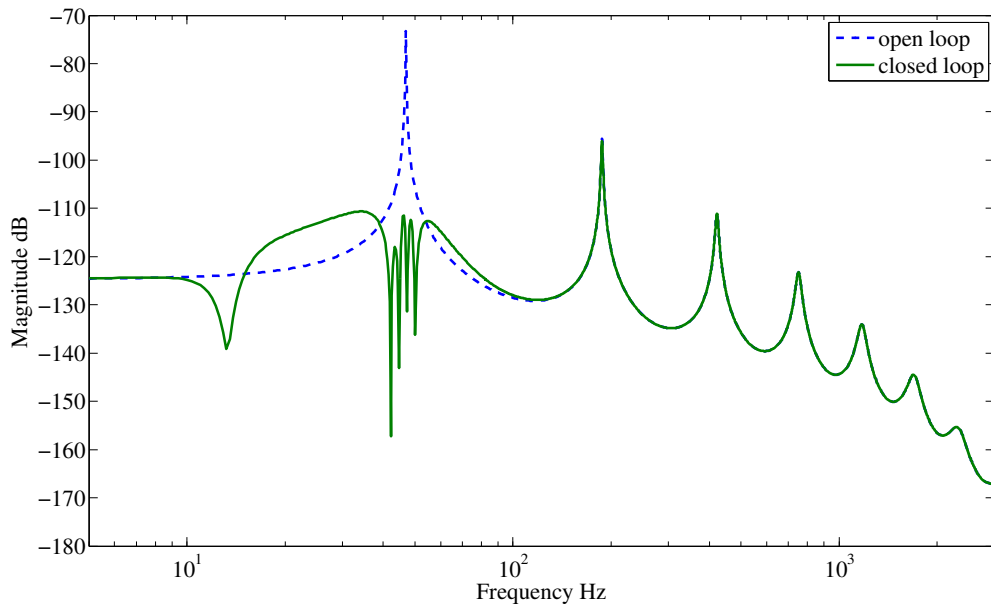


Figure 3.13: Magnitude FRF of primary disturbance input to local sensor with (solid) and without (dashed) feedback control,  $\hat{k}(j\omega)$

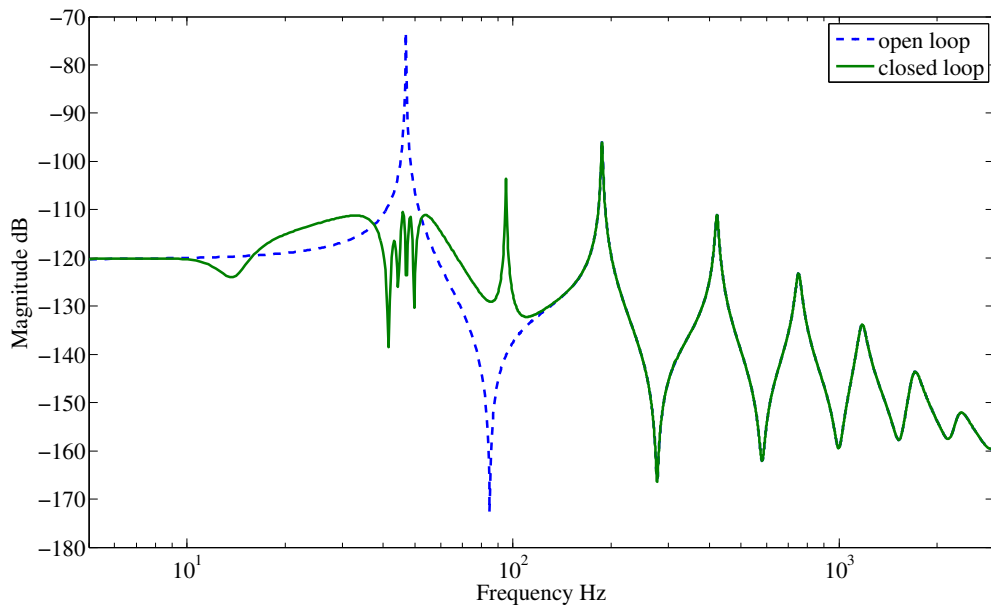


Figure 3.14: Magnitude FRF of primary disturbance input to remote output with (solid) and without (dashed) feedback control,  $\hat{k}(j\omega)$

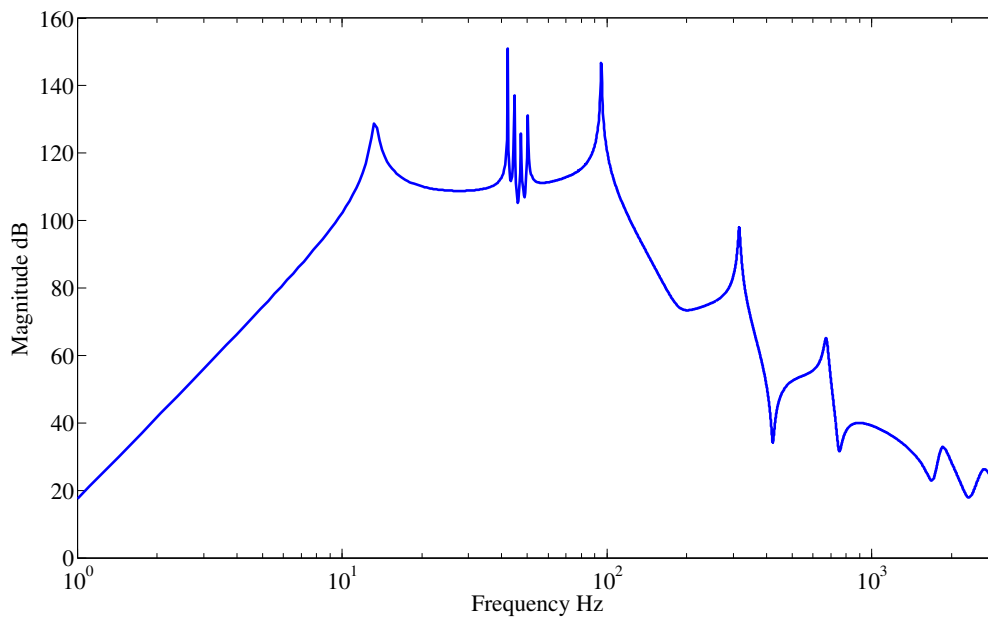


Figure 3.15: Magnitude FRF of controller,  $|\hat{k}(j\omega)|$

time delay due to instrumentation need to be explicitly determined using this method. Robustness to uncertainties or unmodelled high frequency dynamics and low frequency actuator resonance has also been incorporated as part of the design procedure. This is achieved using weighting filters with appropriate cut off frequencies that are selected depending on the requirements to avoid control spillover. A simulated example using a finite element model of a beam shows the practical potential of a systematic procedure to design a controller for simultaneous mitigation of vibration at the local and remote points.

# Chapter 4

## Vibration Attenuation Using a Remote Controller at a Non-resonating Point

### 4.1 Introduction

The original remote vibration control design for was experimentally validated on a blade rig facility for harmonic or tonal excitation [Daley and Wang, 2008]. The digital implementation of this controller requires extraction of the Fourier component of the noise corrupted output signal using an approach from [Liu and Daley, 1999]. The recursive least squares algorithm [Ljung, 2002] is used to determine the gain and phase of the measured output signal with respect to a sinusoidal reference signal. This is then used to apply the control input after multiplying its gain with the controller gain and adding its phase with the phase of controller.

The blade rig used in this study replicates the vibration problem encountered in rotor blade propulsion systems which is widely used in helicopters and marine vessels. The oscillatory vibration is caused when the propeller blades rotate through a non-uniform wake velocity in the fluid field. The response levels increase close to the resonant frequency of the blades and this gets transmitted through the shaft to the hull or fuselage via the thrust bearing. The construction and working of the experimental set-up is described in more detail in section 4.2.

It was shown in chapter 3 that the controller design using the original geometric method results in an unstable controller. A stable and stabilising solution using the

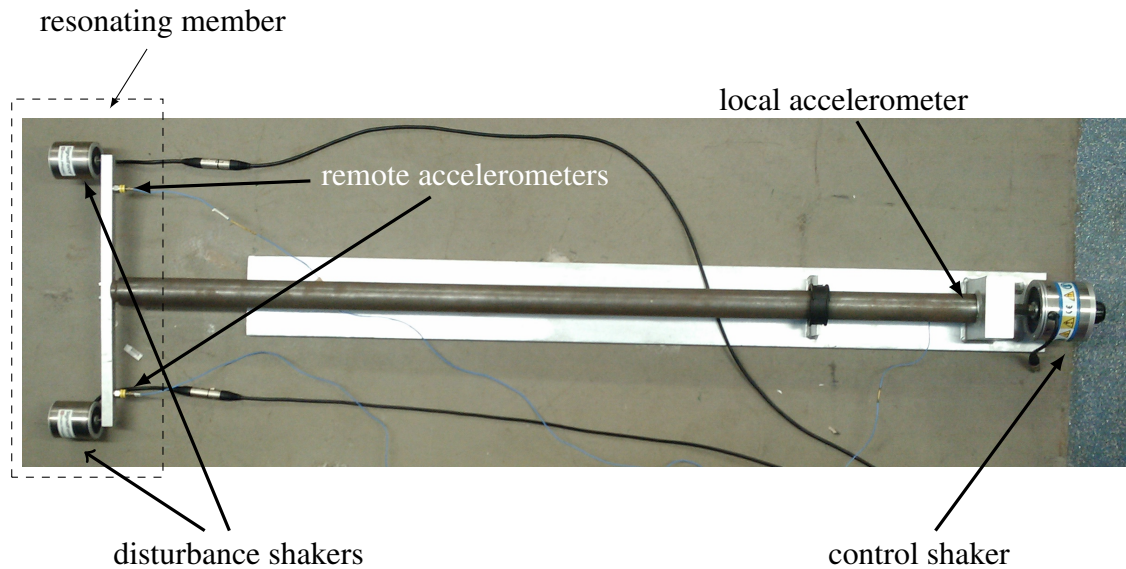


Figure 4.1: Top view of the experimental facility

geometric methodology presented in chapter 3 is easier to implement as it does not suffer from the complications encountered in the implementation of an unstable controller. Also, it is possible to systematically avoid the excitation of high frequency dynamics using this method. In this chapter, the geometric method for the design of stable and broadband vibration controllers is experimentally validated using the propeller blade test rig<sup>1</sup>.

## 4.2 Experimental set-up

A picture of the blade rig used for experimental testing is shown in figure 4.1. It is made up of a long shaft supported at one end on a rigid block and at the other end pinned to a short iron bar element, which acts as the resonating member in this experiment. The shaft is bolted with screws near the mid span of the beam element. The primary excitation signal  $f_p(t)$  is a common signal fed to two smaller shakers (30 N each) attached at both ends of the beam which acts as the transient loading force due to rotation of the propeller blades. The vibration at the blade end of the shaft  $q_p(t)$  is the summation of

<sup>1</sup>This work was carried out by the author during a research visit to the Institute of Sound and Vibration Research at the University of Southampton in March-April 2012

outputs measured by two accelerometers connected near each of the disturbance shakers. Remote output is composed of the summation of these measurements because it is dominated by the dynamics of the first bending mode. As both the sensors are in phase it approximates appropriately with the first bending mode. Maximum transmission of force to the thrust block occurs around the first bending mode of the blade element. The total momentum of higher modes that is transmitted through the connected shaft is negligible. The control input  $f_c(t)$  drives the control shaker (50 N) attached at the other end of propeller shaft on the thrust block and a local accelerometer on the thrust block measures local vibration levels  $q_c(t)$ .

In marine vessels the thrust block is rigidly connected to the hull, which is to be safeguarded against excessive vibration. Vibration is transmitted from the blade end along the shaft to the hull via the thrust block end and is particularly detrimental at the blade resonant frequency. Due to difficulties in measuring and actuating at the blade end for most applications, it is desired to control both blade vibration and its transmission using sensors and actuators mounted on the thrust block only<sup>2</sup>. This blade system can be considered as a two input two output system with the frequency response function matrix relating the disturbance and control inputs to the remote and local vibration outputs as

$$\begin{bmatrix} q_c(j\omega) \\ q_p(j\omega) \end{bmatrix} = \begin{bmatrix} g_{cc}(j\omega) & g_{cp}(j\omega) \\ g_{pc}(j\omega) & g_{pp}(j\omega) \end{bmatrix} \begin{bmatrix} f_c(j\omega) \\ f_p(j\omega) \end{bmatrix} \quad (4.1)$$

The frequency response function matrix in (4.1) is obtained by exciting the disturbance shakers and control shaker with an uncorrelated white noise signal and taking measurements of the blade and thrust block accelerometers. The magnitude frequency response of the open loop path from primary excitation input of the disturbance shakers to the outputs on the thrust block and the blade end is plotted in figure 4.2(a) and figure 4.2(b), respectively. These show that close to the frequency of the first bending mode of the blade (i.e. the iron beam connected to one end of the shaft), vibration transmission to the thrust block is amplified. A feedback controller to achieve simultaneous reduction in the thrust block and blade vibration outputs is designed around this frequency band.

---

<sup>2</sup>It should be noted that the control arrangement shown in figure 4.1 is the subject of a BAE Systems patent [Pearson and Emery, 2003]

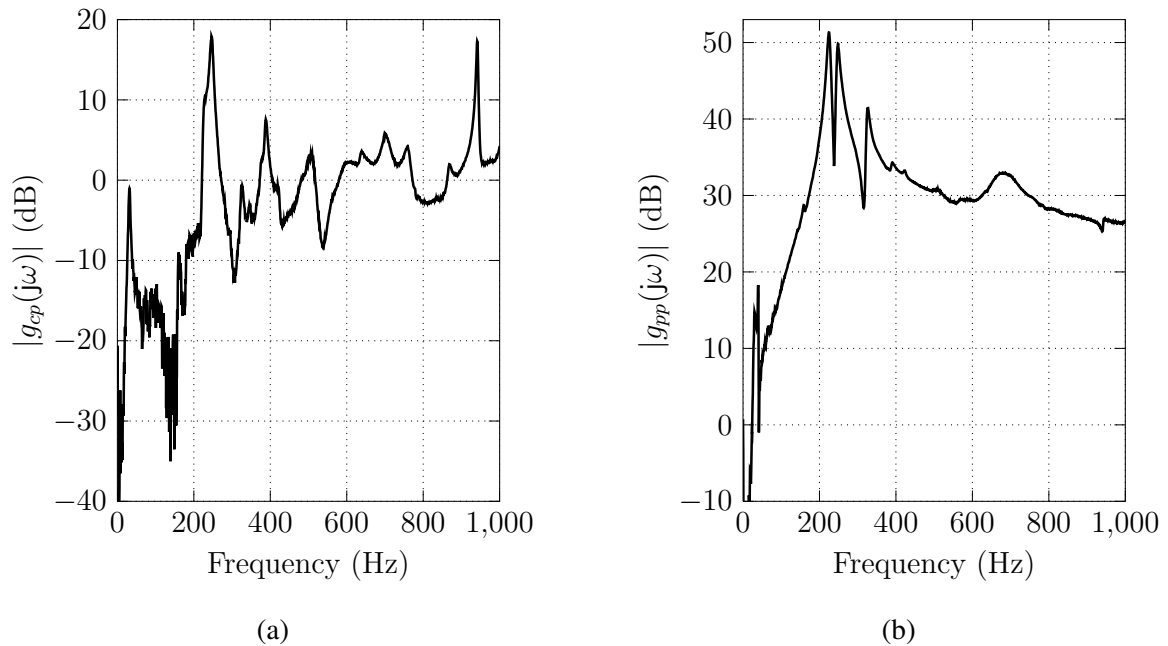


Figure 4.2: Magnitude frequency response of primary excitation input to (a) thrust block vibration output and (b) blade vibration output

### 4.3 Description using Relative Gain Array

The experimental assembly used in this study is noteworthy because it consists of two coupled structural components which makes it complex. This distinguishes its requirement for a control algorithm different from other active structural damping techniques. It is later established in section 5.3 of chapter 5 that active control of vibration close to resonance at the local point leads to global mitigation of vibration but this holds true only if the control force acts directly on the resonating part of the structure. However in the blade rig, the control force is applied to a non resonating part of the structure and hence it does not ensure global vibration attenuation. The vibration due to the resonating component of the structure is transmitted to another part of the structure. Therefore, close to resonance associated with a structural component, response levels at any other point on the whole structure is also amplified. Vibration attenuation using control action at a non-resonating part of the structure, therefore, also depends on the coupling between both structures. The difficulty in observability and controllability of the blade resonance at the thrust block side will manifest as a smaller intersection of circular re-

gions in the  $\gamma$ -plane that represent attenuation at the resonating and non-resonating part of the structure. Active damping of the blade resonance using control action at the thrust block is not a feasible objective for the blade rig set-up. Another tool from multi-variable control design is more useful to infer the performance at the blade end, which is described next.

In this section, it is shown that the design parameter from the geometric approach has a direct correspondence to the Relative Gain Array (RGA). Although the RGA is a tool used in chemical process control to evaluate efficient pairing between different input and output combinations, in this work it is used to demonstrate the effect of a control input on a vibration output at various remote points. The RGA between an input and output signal is the ratio between the loop gain, when all other loops are open, to the loop gain when all other loops are closed. The measure of difficulty in controlling a particular output using a given input can be readily obtained from the RGA matrix. For a system, large RGA elements indicate strong interactions and the system will be ill-conditioned. RGA matrix is a function of frequency and its value at crossover frequencies are important. The pairing rule for independent control design states that the control input which has an RGA element closer to 1 should be used to actuate that output. Many alternatives to RGA that consider both the gain and phase of the RGA elements, such as RGA number and iterative RGA, have also been developed. The RGA matrix at a discrete frequency is next defined for the blade rig system given by (4.1). The gain matrix for this system at a discrete frequency  $\omega_0$  can be written as

$$G_{\omega_0} = \begin{bmatrix} g_{cc}(j\omega_0) & g_{cp}(j\omega_0) \\ g_{pc}(j\omega_0) & g_{pp}(j\omega_0) \end{bmatrix} \quad (4.2)$$

The relative gain array for this gain matrix is calculated as

$$\Lambda(G_{\omega_0}) = G_{\omega_0} \otimes (G_{\omega_0}^{-1})^T \quad (4.3)$$

where  $\otimes$  is the Hadamard or Schur product. The individual elements of this  $2 \times 2$  matrix

are given as

$$\Lambda(G_{\omega_0}) = \begin{bmatrix} \left(1 - \frac{g_{cp}(j\omega_0)g_{pc}(j\omega_0)}{g_{cc}(j\omega_0)g_{pp}(j\omega_0)}\right)^{-1} & \left(1 - \frac{g_{cc}(j\omega_0)g_{pp}(j\omega_0)}{g_{cp}(j\omega_0)g_{pc}(j\omega_0)}\right)^{-1} \\ \left(1 - \frac{g_{cc}(j\omega_0)g_{pp}(j\omega_0)}{g_{cp}(j\omega_0)g_{pc}(j\omega_0)}\right)^{-1} & \left(1 - \frac{g_{cp}(j\omega_0)g_{pc}(j\omega_0)}{g_{cc}(j\omega_0)g_{pp}(j\omega_0)}\right)^{-1} \end{bmatrix} \quad (4.4)$$

The rows and columns of an RGA matrix sum to unity and also as per the pairing rule, an input should be used to actuate a particular output for which the corresponding RGA element is close to unity. If the RGA matrix (4.4) is multiplied by a diagonal scaling matrix then the pairing rule is determined by the proximity of the elements to  $W_\gamma(j\omega_0)B_{cc}(j\omega_0)$ , which also has a magnitude close to unity in the design bandwidth.

$$\begin{bmatrix} W_\gamma(j\omega_0)B_{cc}(j\omega_0) & 0 \\ 0 & W_\gamma(j\omega_0)B_{cc}(j\omega_0) \end{bmatrix} \times \Lambda(G_{\omega_0}) = \begin{bmatrix} \Lambda_{11} & \Lambda_{12} \\ \Lambda_{21} & \Lambda_{22} \end{bmatrix} \quad (4.5)$$

where  $W_\gamma(j\omega)$  is the filter for robustness and  $B_{cc}(j\omega)$  is the Blaschke product formed from the non-minimum phase zeros of the local control path transfer function and

$$\Lambda_{11} = \Lambda_{22} = \left( \frac{1}{W_\gamma(j\omega_0)B_{cc}(j\omega_0)} - \frac{g_{cp}(j\omega_0)g_{pc}(j\omega_0)}{W_\gamma(j\omega_0)B_{cc}(j\omega_0)g_{cc}(j\omega_0)g_{pp}(j\omega_0)} \right)^{-1}$$

$$\Lambda_{12} = \Lambda_{21} = \left( \frac{1}{W_\gamma(j\omega_0)B_{cc}(j\omega_0)} - \frac{g_{cc}(j\omega_0)g_{pp}(j\omega_0)}{W_\gamma(j\omega_0)B_{cc}(j\omega_0)g_{cp}(j\omega_0)g_{pc}(j\omega_0)} \right)^{-1}$$

The magnitude of the elements of this matrix is determined by the magnitude of the corresponding RGA elements only. Additionally, the magnitude of elements of this matrix between the control input and the blade vibration output has a distinct relation to the size and position of circles in  $\gamma$ -plane that represents feasible attenuation in vibration levels at the blade and thrust block end. It can be seen that this element is the inverse of the difference between the centre of both these circles. This shows that if the centre of circles that denote reduction in output at the remote point and at the local point are close in the  $\gamma$ -plane, then the RGA element will be large. Although a very large RGA element is not desirable for many chemical process control applications, it is necessary for the active control of remote vibration. A large RGA element corresponds to a larger region of overlap for the circles in the  $\gamma$ -plane, which allows for maximum

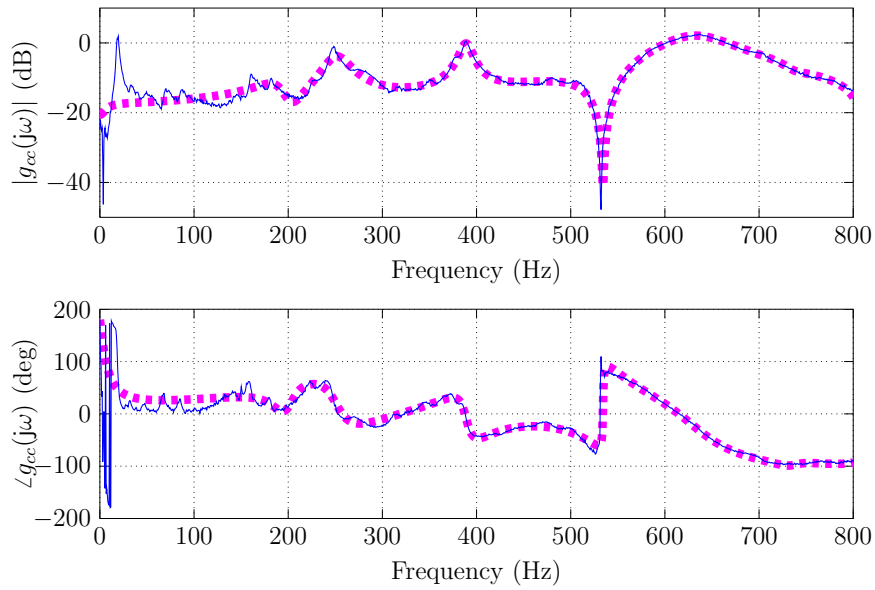


Figure 4.3: Magnitude and phase frequency response of the local control path from control shaker input to thrust block accelerometer measurements (solid) and an identified model (dashed)

attenuation simultaneously at the local and remote locations. On the other hand, if the centre of both circles are far apart, then the RGA element for the cross-coupling term will be small which means that a large control action will be needed to reduce the output at the blade end.

## 4.4 Control design

The first step is to determine an LTI model for the open loop control path,  $\tilde{g}_{cc}(j\omega)$ , from the measured frequency response. The measured frequency response data of the path from control shaker input to acceleration output on the thrust block for frequencies below 800 Hz is fitted with a 15th order transfer function model using least squares fit as shown in figure 4.3. This identified transfer function has 1 right half plane zero so that  $B_{cc}(j\omega)$  is of order 1 and  $\hat{g}_{cc}(j\omega)$  has this RHP reflected into the LHP. The high frequency dynamics neglected is not a cause for concern as the filter,  $W_\gamma(j\omega)$ , avoids control spillover thus ensuring that the controller does not excite unmodelled high frequency dynamics. However, the control shaker resonance at 20 Hz can potentially lead

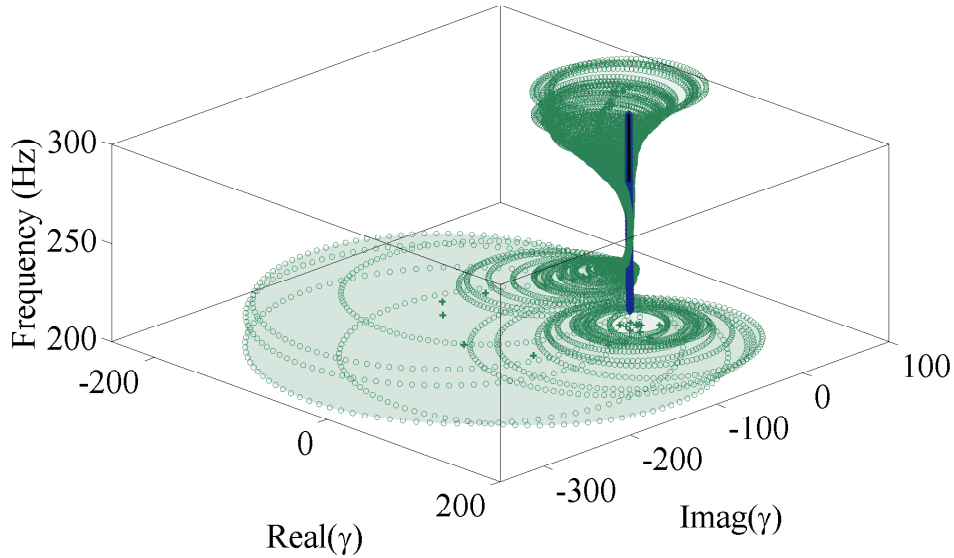


Figure 4.4: Portrayal of constraint regions in  $\gamma$ -plane that denote attenuation in blade vibration for discrete frequencies between 200 Hz and 300 Hz. Unit radius circles corresponding to reduction of vibration at the thrust block appear as a cylinder passing through the origin

to instabilities if the control signal exerts more gain at low frequencies. This can additionally be dealt with by selecting  $W_\gamma(j\omega)$  as a bandpass filter. It is selected as a bandpass butterworth filter with lower and higher cut-off frequencies selected as 100 Hz and 600 Hz, respectively.

The circles in the  $\gamma$ -plane corresponding to a reduction in vibration at the local and remote outputs, given by inequalities (3.22) and (3.24), for frequencies around the first bending mode of the beam is shown in figure 4.4. The circles corresponding to reduction in vibration at the blade end are very large in the frequency band 200 Hz to 220 Hz and above 270 Hz. The distance between the centre of both circles is large and so it will not be possible to achieve considerable reduction in vibration levels at the blade end without amplifying vibration at the thrust block end. Moreover, the off-diagonal elements in the RGA matrix for this frequency are very small which indicates the limited influence of the control action on the vibration output at the blade end. Therefore, optimal values for  $\gamma$  at these frequencies are selected such that the vibration level at the thrust block is reduced without increasing the level at the blade end.

### 4.4.1 Interpolation of optimal $\gamma$ data values

The set of optimal values for  $\gamma$  at discrete frequencies in the design frequency band is interpolated by a stable transfer function using the Nevanlinna Pick interpolation algorithm. A stable  $\gamma(j\omega)$  that interpolates the optimal data set is possible only if the associated Pick matrix is positive definite. As the Pick matrix is basically defined for data values that are interpolated in the right half plane, a transformation is needed on the optimal  $\gamma$  data set. The Pick matrix is then calculated as

$$P = \left[ \frac{1 - Z_k \bar{Z}_l}{s_k + \bar{s}_l} \right]_{k,l=1}^n = \left[ \frac{1 - \frac{\gamma_k \bar{\gamma}_l}{M M}}{\sigma + j\omega_k + (\sigma - j\omega_l)} \right]_{k,l=1}^n \quad (4.6)$$

The Pick matrix for the initial selection of  $\gamma$  data values is not positive definite. An approach from [Wang and Daley, 2010] can be used to modify the  $\gamma$  values so as to satisfy the positive definiteness of the matrix. This is done using Linear Matrix Inequalities to alter the optimal  $\gamma$  values within a very narrow tolerance limit until the Pick matrix is positive definite. The subsequent steps in the identification of a stable  $\gamma(j\omega)$  is similar to the description given in section 3.5.3 of chapter 3. In the frequency interval from 200 Hz to 300 Hz there are 164 discrete frequencies for which an optimal  $\gamma$  value is selected. Only 6 of the optimal  $\gamma$  data values are used for interpolation so that the final compensator is of low order. This results in a stable  $\gamma(j\omega)$  that also satisfies the controller stability condition, namely, the nyquist contour of  $\gamma(j\omega)B_{cc}(j\omega)W_\gamma(j\omega)$  does not encircle  $-1$ .

The final operating  $\gamma$  values for frequencies 220 Hz to 250 Hz obtained from the frequency response of the interpolated  $\gamma(j\omega)$  are shown in figure 4.5. It can be seen that in the frequency range 230 Hz to 245 Hz, circles representing a reduction in blade vibration converge towards the origin and reduce in size. Due to this several more  $\gamma$  data values have to be selected in this frequency band alone to get a good transfer function approximation, but this will increase the order of  $\gamma(j\omega)$  considerably, which in turn affects the order of controller. The circles corresponding to reduction in blade vibration output for all other frequencies in this frequency band are considerably larger than its counterpart for reduction at the thrust block. The final operating values for  $\gamma$  lie inside the unit circle that corresponds to local vibration attenuation. This is esti-

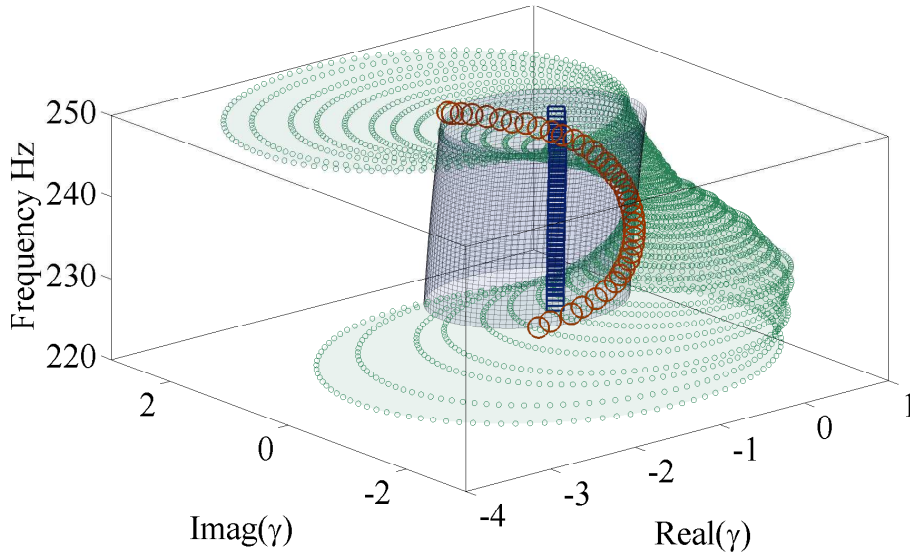


Figure 4.5: The reduction in vibration at the thrust block ( $\circ$ ) and blade end portrayed as regions inside circles in  $\gamma$ -plane. The frequency response of the interpolated  $\gamma(j\omega)$  ( $\square$ ) and the optimal selected values for interpolation ( $\bigcirc$ )

mated to achieve only slight reduction in the blade vibration output using a 58th order controller. This vibration attenuation problem is a case of very extreme magnitude for the dimensionless parameter discussed in [Freudenberg et al., 2003b], which is equivalent to the function formed by the centre of remote vibration reduction circle given as  $-g_{cc}(j\omega)g_{pp}(j\omega) [g_{cp}(j\omega)g_{pc}(j\omega)B_{cc}(j\omega)W_{\gamma}(j\omega)]^{-1}$ . The magnitude of this function is a measure of the severity of the trade-off between disturbance attenuation and stability robustness. This also substantiates the difficulty in attenuation of the blade vibration levels without a deterioration at the thrust block end which may lead to closed loop instabilities.

A controller realised in terms of this  $\gamma(j\omega)$  by substituting it in (3.26) has a magnitude frequency spectrum as shown in figure 5.11. The gain of the controller starts to roll-off after 600 Hz due to the action of filter,  $W_{\gamma}(j\omega)$ , thereby improving robustness to unmodelled high frequency dynamics.

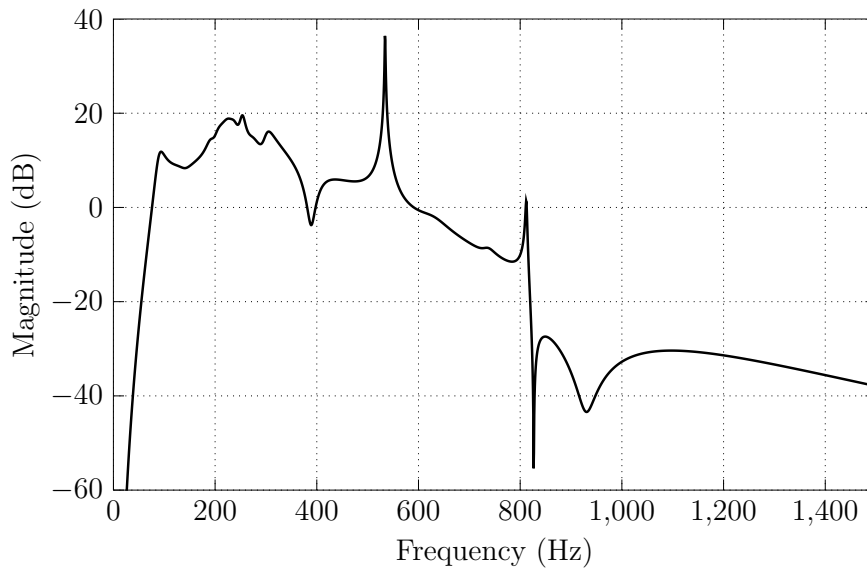


Figure 4.6: Magnitude frequency spectrum of the synthesized controller

## 4.5 Experimental implementation

The controller obtained in the previous section is a compensator transfer function in the continuous time domain. It is converted to a discrete time model using a first order hold approximation with a sampling frequency of 5 kHz. The frequency characteristic of the discrete time model matches exactly with that of the continuous time model especially in the design frequency bandwidth. A minimal and balanced realisation of the state space model of this compensator is used such that its observability and controllability grammians are equal and diagonal. It is then integrated with the experimental set-up through Simulink using a dSPACE real time interface hardware. The acceleration outputs at the thrust block,  $q_c(t)$ , and blade end,  $q_p(t)$ , are measured to compare the closed loop and open loop responses.

### 4.5.1 Sinusoidal excitation of frequency 247 Hz

In order to test the reduction at the resonant frequency of the blade, it is excited by a sinusoidal excitation of 247 Hz. The power spectral density of the measured acceleration at the thrust block with and without feedback control for this excitation input is plotted in figure 4.7. It shows more than 14 dB reduction in magnitude at this frequency. The

## 4.5. EXPERIMENTAL IMPLEMENTATION

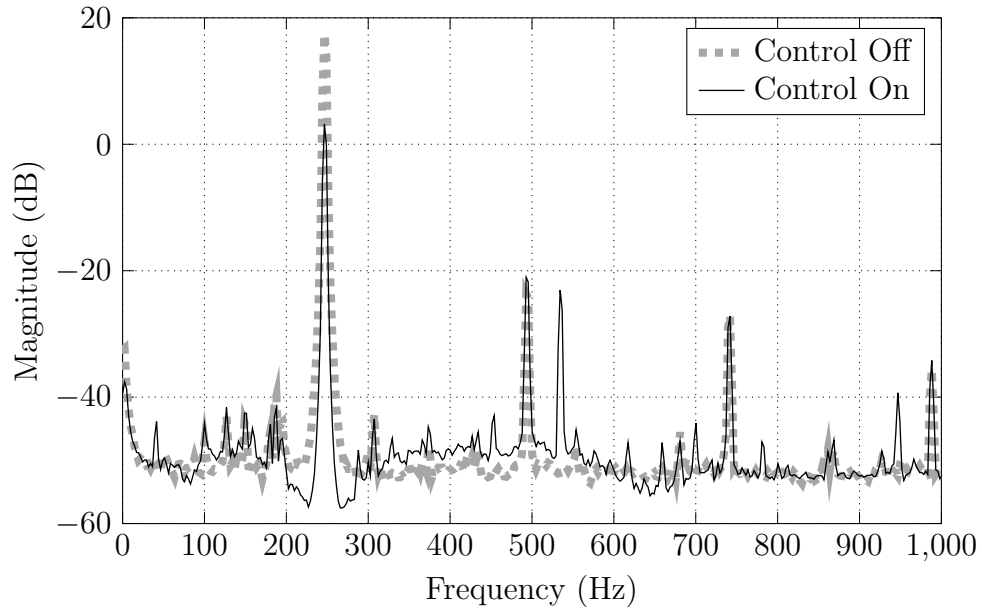


Figure 4.7: Power spectral density of accelerometer output on thrust block when disturbance shakers on the blade are excited by a sinusoidal of 247 Hz

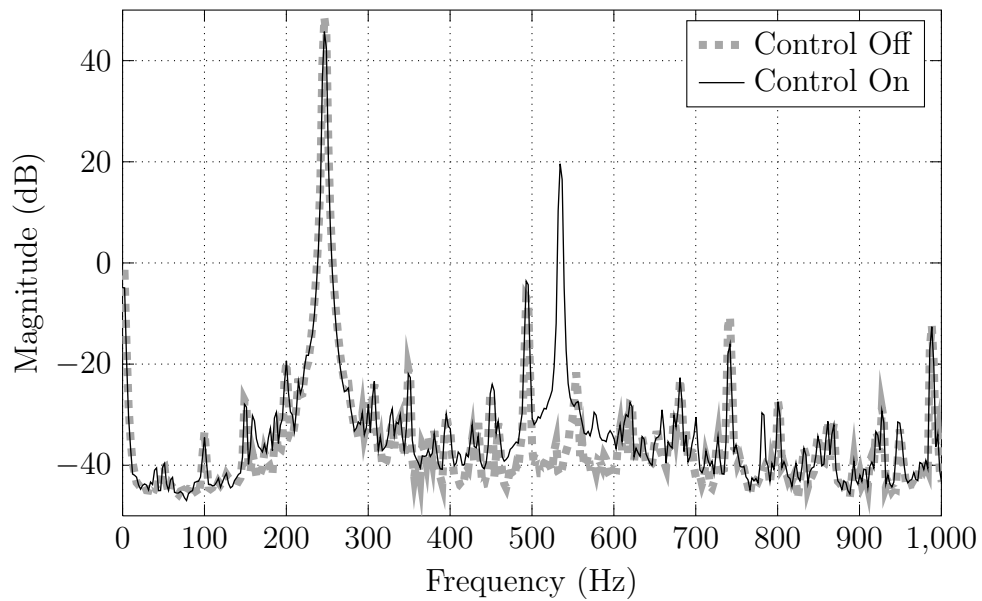


Figure 4.8: Power spectral density of the summation of accelerometer outputs on blade end when disturbance shakers on the blade are excited by a sinusoidal of 247 Hz

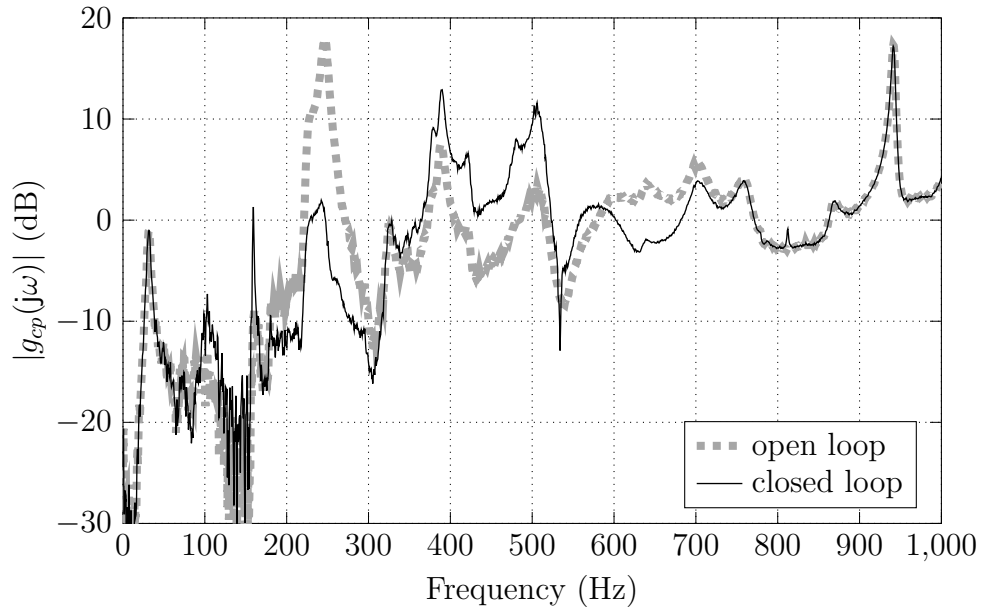


Figure 4.9: Estimated magnitude frequency response of the path from primary excitation input to thrust block output with (solid) and without (dashed) feedback control

power spectral density of the summation of outputs from each ends of the blade in figure 4.8 shows around 3 dB reduction in magnitude at this frequency. However, a peak at 534 Hz in the PSD of both closed loop outputs can be noticed which is not originally present for the open loop. However, this additional component is well below ( $\sim 20$  dB) the dominant 247 Hz tone. The implications of this sharp peak, its underlying causes and a solution to suppress it are discussed in the next section.

### 4.5.2 Reduction of peak in controller FRF

The estimated magnitude of the closed loop frequency response of the thrust block and blade outputs to the primary excitation input with and without feedback control is plotted in figure 4.9 and figure 4.10, respectively. These show that around 534 Hz, the closed loop system has low stability margins. This is caused by the peak in controller FRF. The controller implementation involves inversion of the minimum phase counterpart of the local control path transfer function so an antiresonance (lightly damped zeros) at frequency 534 Hz in the local control path FRF (figure 4.3) appears as a peak in the controller FRF. Filter  $W_\gamma(j\omega)$  has a high cut-off frequency 600 Hz which is higher

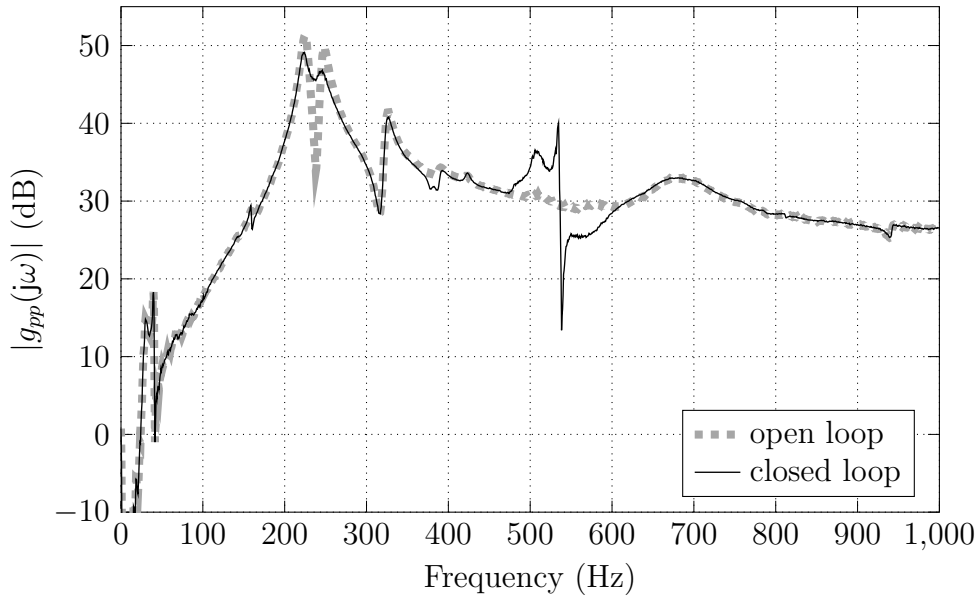


Figure 4.10: Estimated magnitude frequency response of the path from primary excitation input to blade vibration output with (solid) and without (dashed) feedback control

than the frequency (534 Hz) at which the peak in controller FRF appears. If the high cut-off frequency of  $W_\gamma(j\omega)$  is reduced below 534 Hz and the order of filter is also increased so as to take account of the sharp increase in this peak then due to limitations as quantified by Bode's sensitivity integral, amplification due to waterbed effect at out-of-bound frequencies will not be spread over a large frequency range and there will be peaks appearing in the closed loop frequency response. Therefore, the controller is implemented in series with a notch filter which has a notch at 534 Hz in order to reduce the peak at this frequency. The magnitude and phase of the controller is unaffected in the design frequency band.

The PSD of acceleration measured at the thrust block with and without feedback control when the blade end is excited by a sinusoidal input of 247 Hz shows around 16 dB reduction in magnitude at this frequency as shown in figure 4.11. The PSD of the summation of acceleration measured at the blade end for the same excitation in figure 4.12 shows around 3 dB reduction in magnitude at this frequency. The peak at 534 Hz is reduced considerably and the performance of the controller is also not compromised.

## 4.5. EXPERIMENTAL IMPLEMENTATION

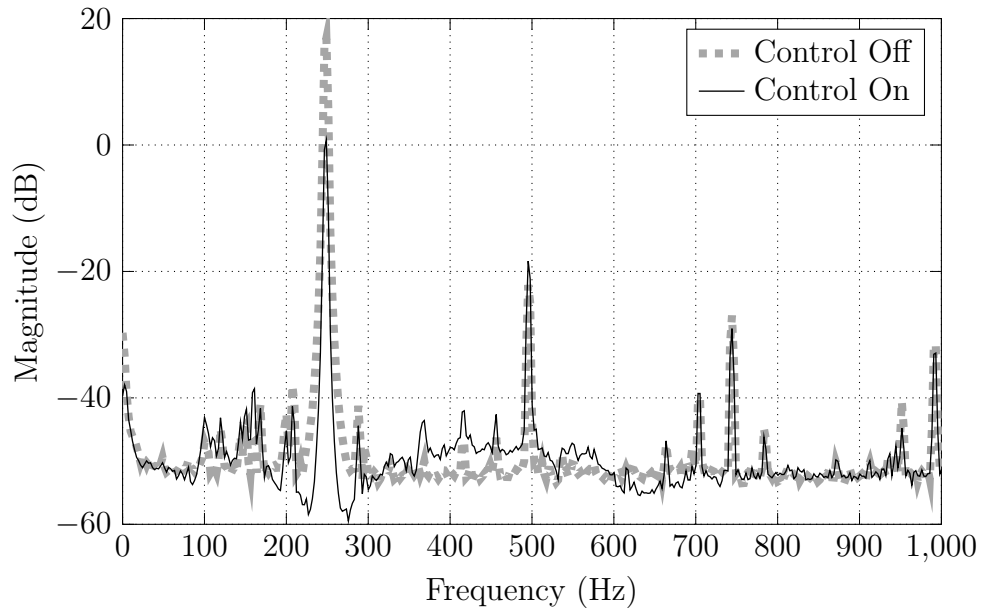


Figure 4.11: Power spectral density of accelerometer output on thrust block when disturbance shakers on the blade are excited by a sinusoidal of 247 Hz, and the controller is implemented in series with a notch filter

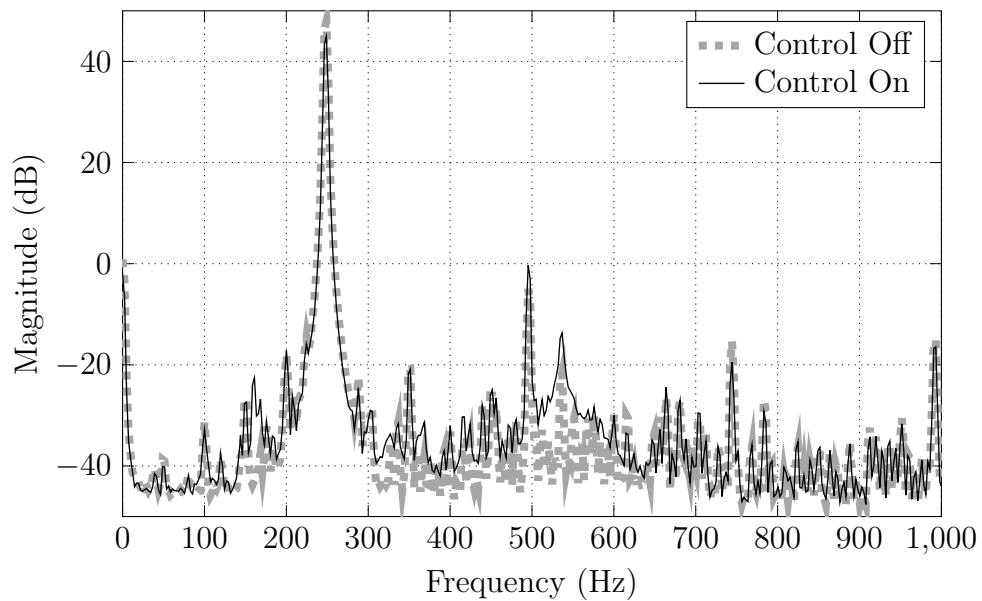


Figure 4.12: Power spectral density of the summation of accelerometer outputs on blade end when disturbance shakers on the blade are excited by a sinusoidal of 247 Hz, and the controller is implemented in series with a notch filter

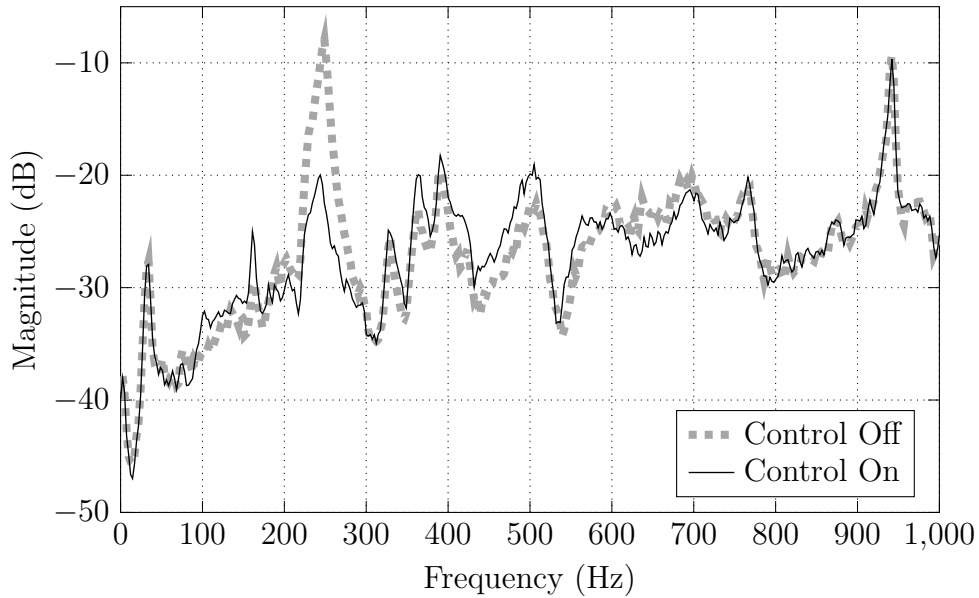


Figure 4.13: Power spectral density of accelerometer output on thrust block when disturbance shakers on the blade are excited by a random white noise input, controller is implemented in series with a notch filter

### 4.5.3 Broad frequency band random excitation

The disturbance shakers are excited by a random white noise input and the PSD of the acceleration outputs from the thrust block and blade end are plotted in figures 4.13 and 4.14, respectively, for the open and closed loop cases. These show a maximum of 12 dB attenuation in the thrust block output while the output at the blade end is only marginally reduced as per design.

## 4.6 Summary

The proposed remote vibration control design approach has been experimentally validated using a laboratory rig that replicates the vibration problem encountered in rotary propeller blade shafting systems. The force transmitted to the thrust block which is predominantly due to the momentum of the first bending mode of the resonating beam element is minimised. As the control force is applied on a non-resonating part of the structural assembly, active damping of this mode is not feasible. Moreover, the circles

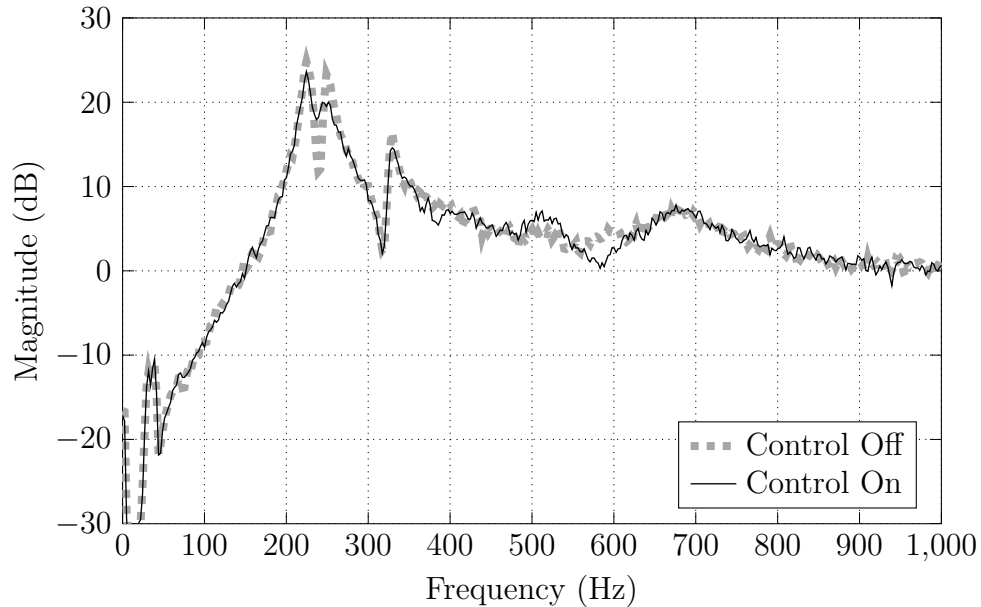


Figure 4.14: Power spectral density of the summation of accelerometer outputs on blade end when disturbance shakers on the blade are excited by a random white noise input, controller is implemented in series with a notch filter

in the  $\gamma$ -plane that correspond to a reduction in thrust block and blade outputs do not overlap. The limited effect of control action on the blade output is also substantiated from the relation between the design parameter and the relative gain array matrix. The RGA elements between input at thrust block and output at blade is the inverse of the distance between the centre of circles in the  $\gamma$ -plane that portray reduction in output at these locations. The centre of both these circles are not close in the  $\gamma$ -plane and consecutively the RGA elements for these frequencies are also small, which demonstrates the limited effect of control action upon the blade vibration output.

# Chapter 5

## Active Damping at Resonance

### 5.1 Introduction

The geometric technique for a stable controller design presented in chapter 3 targets reduction in vibration at pre-determined locations in a certain frequency band only. In this chapter, the feasibility of designing a controller using the geometric approach to target spatially global vibration attenuation in a broader frequency band will be investigated. Initially it is proved analytically in terms of the design parameter that when control action is applied on a resonating structure, the selection of design freedom parameter to achieve maximum attenuation at the local point would also correspond to attenuation at other remote points at which that mode is observable.

Firstly, this proof presented in section 5.3 simplifies the selection criterion for optimal  $\gamma$  values near resonant frequencies and can be used to address vibration attenuation in a wider frequency band encompassing several mode resonant frequencies. Secondly, it has implications for spatially global vibration attenuation for lightly damped structures using only a single pair of transducers for measurement and actuation. This is validated using an experimental beam facility for vibration attenuation at both local and remote locations around its first bending mode frequency<sup>1</sup>.

---

<sup>1</sup>This work was carried out at the Institute of Sound and Vibration Research, University of Southampton, during March-April 2012

## 5.2 Active Damping

The response of a structure is particularly detrimental when the disturbance forces are near its natural frequency as the magnitude is amplified near these frequencies. Several control design methods achieve dissipation of energy at resonance by modifying the eigenvalues of the open loop system. The closed loop system properties are altered by increasing the damping of the natural frequency or shifting the eigenvalues away from frequency of the excitation signal. Positive position feedback control design developed by Goh and Caughey [1985] can increase the damping of desired modes when the natural frequency is accurately known. It does not suffer from control spillover effects at high frequencies but may amplify the response at frequencies lower than the natural frequency of the second order controller. It is also essential for this control scheme that the control sensor and actuator be perfectly collocated, similar to the requirement in direct velocity feedback control.

Other control design methods to assign the closed loop poles with desired damping and natural frequency are accomplished using the pole placement feedback approach [Kautsky et al., 1985], independent modal space control approach [Daley et al., 2004] or the receptance based active control method [Mottershead et al., 2008]. The effects of spillover can be minimised in these types of control design methods by seeking a condition of unobservability [Datta et al., 1997] or uncontrollability [Ghandchi Tehrani et al., 2010] of the higher order modes so that the corresponding eigenvalues remain unchanged. However, the proportional and derivative gain vector for this approach is formed from the inversion of a measurement dependant matrix. The rank of this matrix is affected by the number of error sensors used and so partial pole assignment is not possible using only a local transducer pair. Also, the experimental studies considered so far have not elaborated if the performance of the receptance based control design is affected by the accuracy of modal parameter estimation technique. On the other hand, the geometric based approach provides a systematic procedure using only a local transducer pair for remote and global vibration attenuation.

### 5.3 Design parameter at resonance

The geometric based controller presented in chapter 3 achieves perfect remote vibration annihilation if values for the optimal  $\gamma$  point is selected as  $U_p(j\omega_0)$ , i.e. the centre of circle (3.24) at frequency  $\omega_0$ . Substituting this value for  $\gamma$  in (3.26) gives the perfect cancellation controller as (5.1). It may not be strictly proper and so needs to be modified before practical implementation [Hong and Bernstein, 1998].

$$k_x^c(j\omega_0) = \frac{g_{xp}(j\omega_0)}{\tilde{g}_{cp}(j\omega_0)\tilde{g}_{xc}(j\omega_0) - \tilde{g}_{cc}(j\omega_0)g_{xp}(j\omega_0)} \quad (5.1)$$

Assuming a worst case scenario such that the centre of the circle for maximum reduction in output at the remote point does not lie inside the circle corresponding to reduction in local vibration, then the ideal disturbance attenuation problem is not solvable and the cancellation controller given by (5.1) will amplify the response level at the local point. The optimal  $\gamma$  point in this case is selected from the region of intersection of the two circles in the  $\gamma$ -plane.

However, it has been shown in previous works that the control of resonant vibrations at a local point on a structure results in global reduction on the structure [Brennan et al., 1995; Pope and Daley, 2009; Post and Silcox, 1990]. The optimal  $\gamma$  value that achieves attenuation at the local point will therefore also lie inside the region in the  $\gamma$ -plane that corresponds to attenuation at any remote point. This result is analytically proven for active structural control of resonant vibration using a control action at a resonating part of the structure. If the control force does not act at a node of any of the modes under consideration then the frequency response between the output at the  $i$ th point and the input at the  $j$ th point can be written in terms of the summation of the first  $N$  dominant modes [Ewins, 2000] as

$$g_{ij}(j\omega) = \sum_{k=1}^N \frac{\psi_{ik}\psi_{jk}}{(-\omega^2 + j2\zeta_k\omega_k\omega + \omega_k^2)} \quad (5.2)$$

where  $\psi_{ik}$  is the  $i$ th element in the mode shape vector  $\psi_k$ ,  $\zeta_k$  is the damping ratio and  $\omega_k$  is the natural frequency of the  $k$ th mode. At a natural frequency  $\omega_n$  of a resonant mode, the frequency response function between the  $i$ th output and the  $j$ th input is given

as

$$g_{ij}(j\omega_n) = \sum_{k=1}^N \frac{\psi_{ik}\psi_{jk}}{(-\omega_n^2 + j2\zeta_k\omega_k\omega_n + \omega_k^2)} \quad (5.3)$$

Expanding the contribution from the first  $N$  modes to the structural frequency response at this frequency gives

$$g_{ij}(j\omega_n) = \frac{\psi_{i1}\psi_{j1}}{(\omega_1^2 - \omega_n^2 + j2\zeta_1\omega_1\omega_n)} + \dots + \frac{\psi_{in}\psi_{jn}}{(j2\zeta_n\omega_n^2)} + \dots + \frac{\psi_{iN}\psi_{jN}}{(\omega_N^2 - \omega_n^2 + j2\zeta_N\omega_N\omega_n)} \quad (5.4)$$

For a lightly damped structure with low modal density, the contribution to the structural frequency response from modes that are away from the dominant mode frequency  $\omega_n$  would be insignificant and can be neglected. Therefore the structural frequency response near a resonant mode frequency can be approximated by the modal frequency response of the dominant mode [Gawronski, 2004] as

$$g_{ij}(j\omega_n) \approx \frac{\psi_{in}\psi_{jn}}{(j2\zeta_n\omega_n^2)} \quad (5.5)$$

Substituting the modal transfer function approximation near mode frequency  $\omega_n$  from (5.5) into the centre of circle (3.24), the value of the design freedom parameter  $\gamma$  for maximum reduction in vibration at node  $x$  is given as

$$\frac{\frac{\psi_{1n}\psi_{1n}}{(j2\zeta_n\omega_n^2)} \frac{\psi_{xn}\psi_{2n}}{(j2\zeta_n\omega_n^2)}}{\frac{\psi_{1n}\psi_{2n}}{(j2\zeta_n\omega_n^2)} \frac{\psi_{xn}\psi_{1n}}{(j2\zeta_n\omega_n^2)}} \frac{1}{B_{cc}(j\omega_n)W_\gamma(j\omega_n)} = - \frac{1}{B_{cc}(j\omega_n)W_\gamma(j\omega_n)} \quad (5.6)$$

which is the value of  $\gamma$  that corresponds to maximum attenuation in local vibration. Thus the centre of the circle in the  $\gamma$ -plane for vibration reduction at any remote point near resonant frequencies coincides with the centre of circle for local vibration reduction, has unit radius and is independent of its location on the structure. As a consequence of this, any controller will have the same effect both locally and at any remote point and in theory can be selected at the common centre of the circles to provide global vibration annihilation.

### 5.3. DAMPING AT RESONANCE

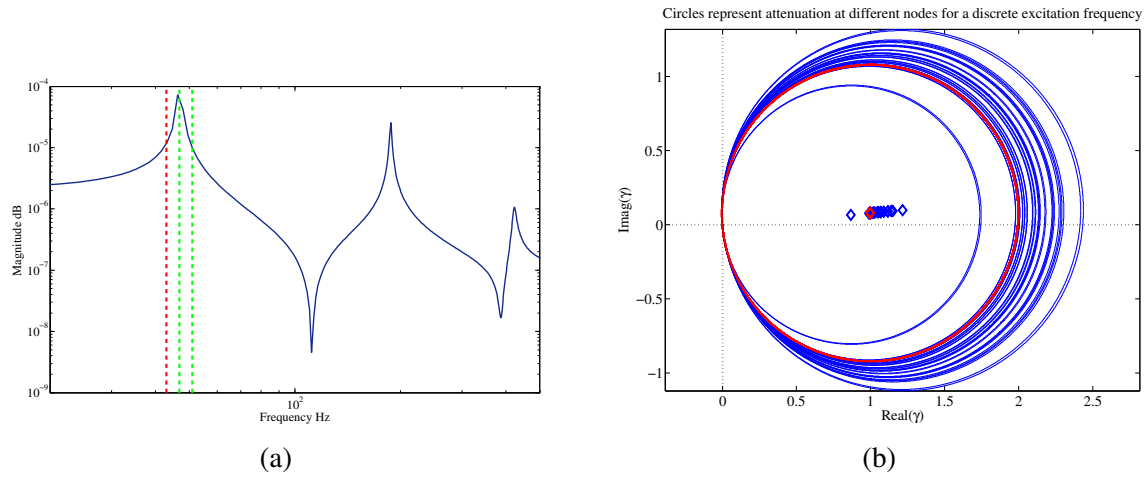


Figure 5.1: (a) the point frequency response plot showing a discrete frequency relative to the peak of resonant frequency highlighted by red dashed line and (b) the circles corresponding to reduction in output at 10 different locations on the beam for this discrete frequency

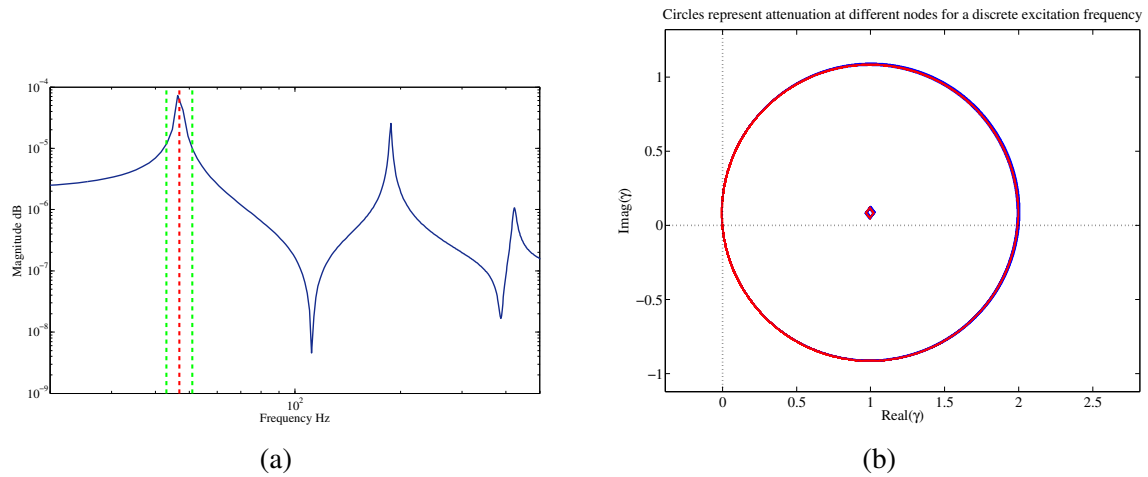


Figure 5.2: (a) resonant frequency highlighted by red dashed line and (b) the circles corresponding to reduction in output at 10 different locations on the beam for this discrete frequency

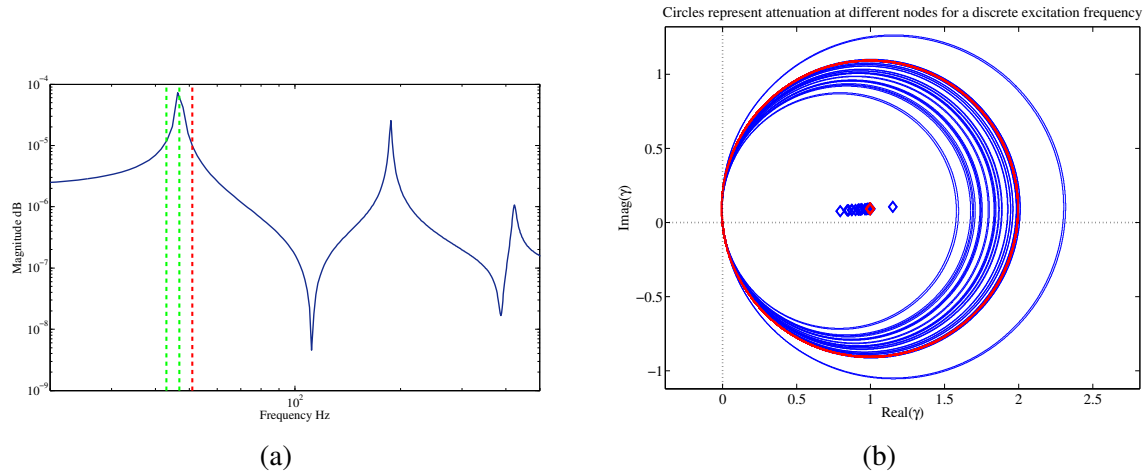


Figure 5.3: (a) a discrete frequency near the peak of resonant frequency and (b) the circles corresponding to reduction in output at 10 different locations on the beam for this discrete frequency

As an example, the finite element model of the beam presented in section 3.5.1 is considered to describe the overlap of regions near resonance described above. The circles and its centres corresponding to reduction in vibration at 10 equidistant positions on the beam are plotted for frequencies at resonance in figure 5.2 and close to it in figures 5.1 and 5.3. As the design frequency moves away from resonance, the common region of intersection between the regions for local and remote vibration attenuation reduces and so it becomes difficult to achieve global attenuation at off resonant frequencies [Johnson et al., 2003]. At an antiresonant frequency, the circles are  $180^\circ$  separated on opposite sides of the origin and have no common region of intersection so the only optimal value of  $\gamma$  is near origin in the  $\gamma$ - plane (i.e. the uncontrolled state).

## 5.4 Active damping of a beam structure

Control design using the geometric method to achieve active damping of a beam structure near its first natural frequency is presented in this section. The response levels near the base of this beam assembly are amplified near its first resonant frequency. The vibration output from the top of the beam is fed back to the controller for corrective action which is applied using two smaller control shakers. This arrangement of error

sensor and control shaker is non-collocated and forms the local control path while the transmission of vibration near the base of the passive isolation mounts that support the beam forms the remote output, which is also distinct from the location of primary excitation. The helpful feature of the design parameter near a mode resonant frequency (as described in the previous section) is also validated for this experimental rig.

### 5.4.1 Experimental set-up

A picture of the test rig is shown in figure 5.4 highlighting the location of sensors and actuators, and an illustration of the experimental set-up for control implementation is shown in figure 5.5. The beam is supported at both ends on passive mounts and a performance measurement sensor is placed near the base of each mount. The summation of output from both these accelerometers forms the remote output,  $q_p(t)$ . The primary disturbance signal,  $f_p(t)$ , is fed to a 170 N *Gearing & Watson IV46* inertial shaker attached on top of the beam which excites the beam near its mid-span. Three sensors mounted on top of the beam at either ends and at its centre produce the error measurement,  $q_c(t)$ , which is fed back to the controller. The three accelerometers attached on top of the beam together give a measurement of the first bending mode. This is calculated by subtracting the top middle accelerometer output  $q_c^m(t)$  from the summation of the top right  $q_c^r(t)$  and top left  $q_c^l(t)$  accelerometer outputs.

Each accelerometer is connected in series with a *FLYDE microAnalog2* amplifier and anti-aliasing filters. The gains on the card of the amplifier for the channels that serve the accelerometers below the mount are set on higher values in order to compensate for the comparatively lower level of response. Anti aliasing filters are set at a cut-off frequency of 700 Hz. The analog voltage signals from the anti-aliasing filters is connected to a 16 bit analog to digital converter. Two 10 N *Labworks Inc.* inertial electrodynamic actuators mounted on the underside of circular discs connected at each end of the beam are used to provide the control input,  $f_c(t)$ . A single control signal is fed to both the identical shakers and so the local control path, comprising of a single measurement output and a single control signal, can be considered as a SISO set up.

The frequency response between the two vibration outputs and the two input signals is required for control design. This is obtained by exciting the disturbance and control shakers separately with a random signal which has a uniform distribution and measuring

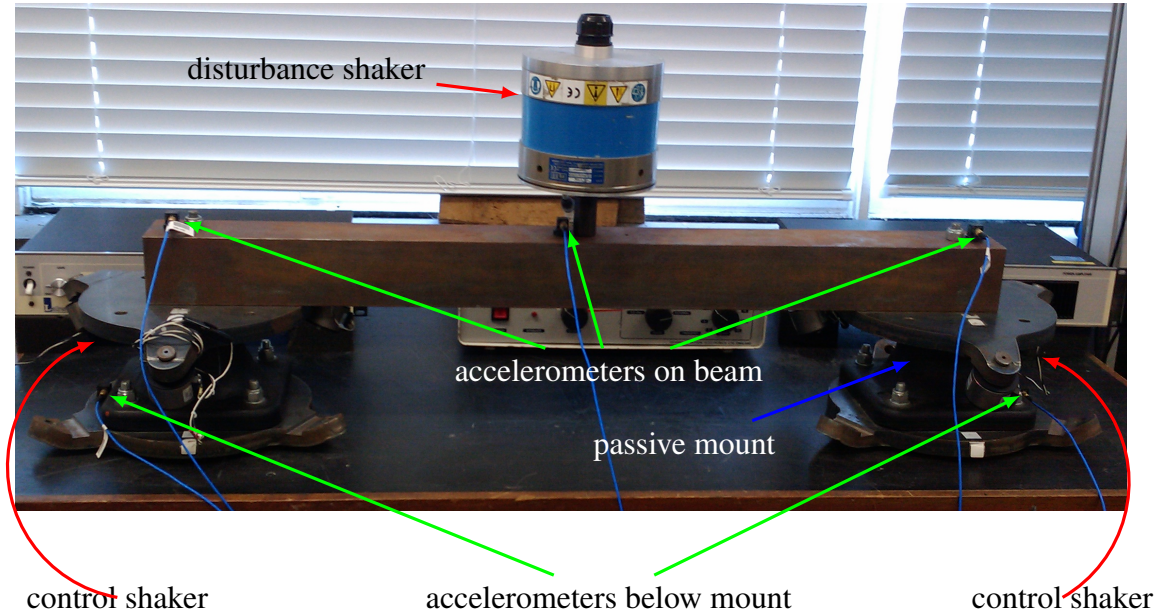


Figure 5.4: Experimental test rig consists of a beam mounted on passive mounts

the local and remote outputs. The plant can be considered as a  $2 \times 2$  system and the frequency response measurements relate the local and remote vibration outputs as

$$\begin{bmatrix} q_c(j\omega) \\ q_p(j\omega) \end{bmatrix} = \begin{bmatrix} g_{cc}(j\omega) & g_{cp}(j\omega) \\ g_{pc}(j\omega) & g_{pp}(j\omega) \end{bmatrix} \begin{bmatrix} f_c(j\omega) \\ f_p(j\omega) \end{bmatrix} \quad (5.7)$$

The frequency response measurement includes the dynamics of: ADC, DAC, sensors, actuators and the associated instrumentation. The first natural frequency of the beam structure found from the magnitude and phase of the frequency response of the open loop paths occurs around 283 Hz as evident from the plots in figure 5.6 (a) and figure 5.6 (b).

### 5.4.2 Control design

The local output measurement alone is used as a feedback signal for the controller as given in (5.8). A geometric based controller that increases the damping in the closed loop outputs of the local and remote points for frequencies near the first natural fre-

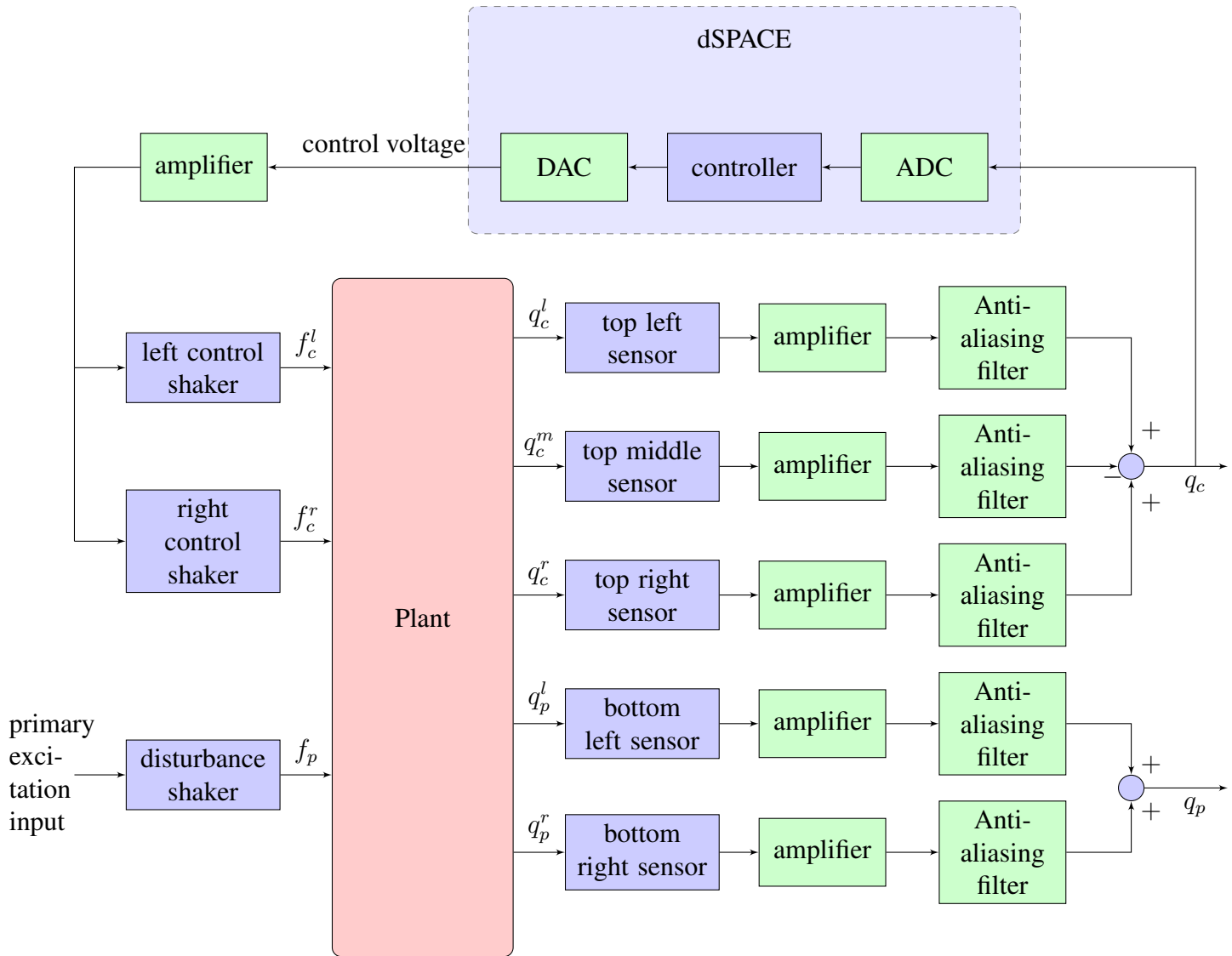


Figure 5.5: Schematic illustration of the experimental set-up

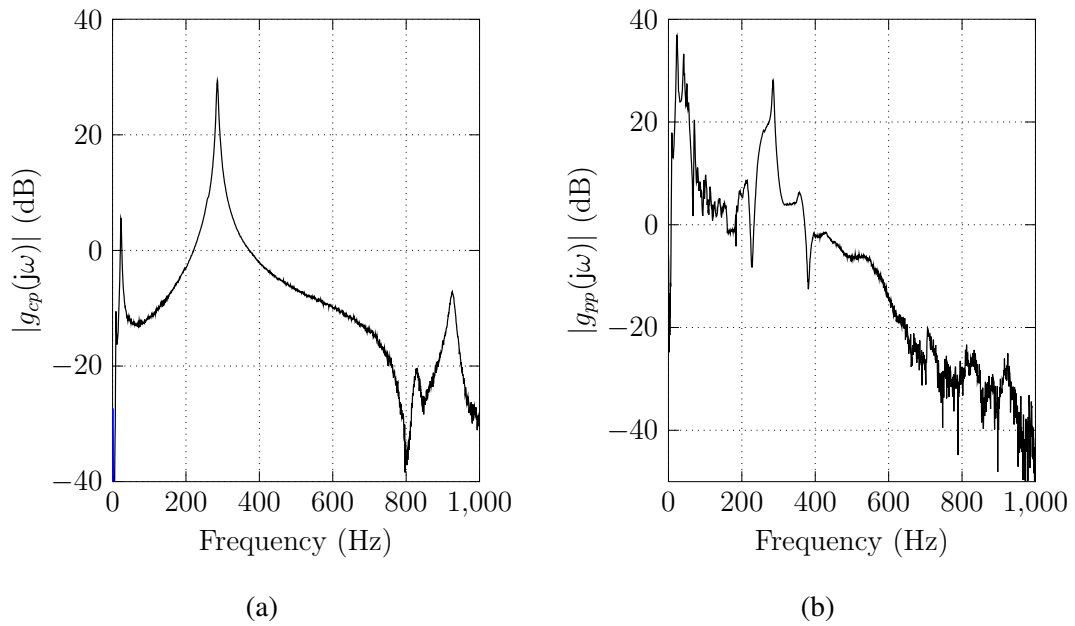


Figure 5.6: Magnitude frequency response of output (a) on top of the beam and (b) at the base of beam near the mounts, for disturbance excitation input

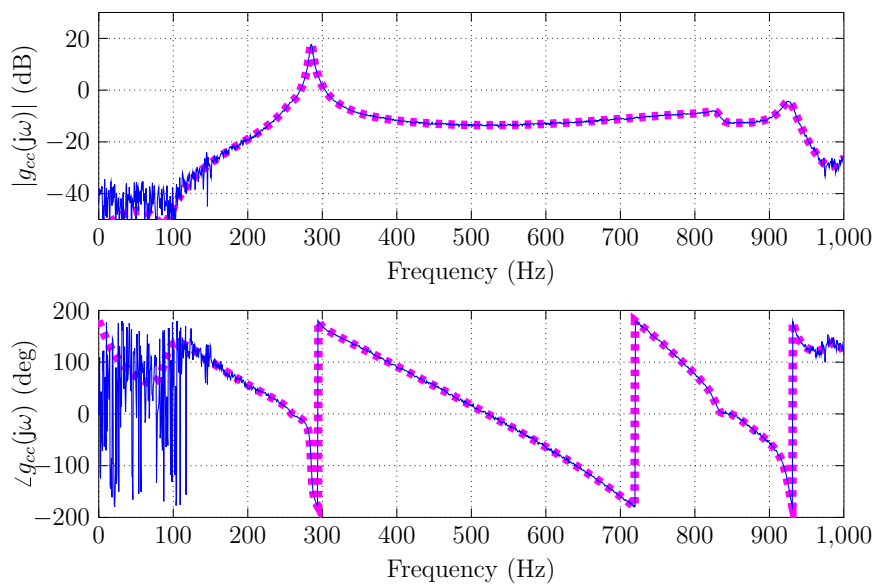


Figure 5.7: Magnitude and phase frequency response of output on top of the beam and control input plotted using data from measurements (solid) and an identified model (dashed)

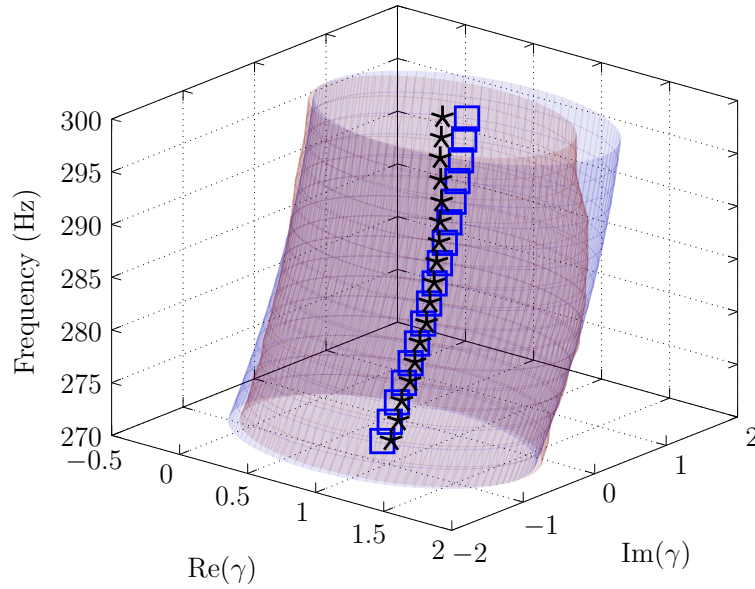


Figure 5.8: Portrayal of vibration attenuation at the local (blue) and remote (red) points as circles in  $\gamma$ -plane and its centres ( $\square$  and  $\star$ , respectively) which denote maximum attenuation at the respective points

quency of the beam is developed.

$$f_c(j\omega) = -k(j\omega)q_c(j\omega) \quad (5.8)$$

The first step is to identify a model for the local control path frequency response function,  $g_{cc}(j\omega)$ . This is done by estimating a transfer function using least squares curve fitting to the frequency response data up to 1 kHz as shown in figure 5.7. This results in a non-minimum phase transfer function containing 9 right half plane zeros. A bandpass filter,  $W_\gamma(j\omega)$ , with low and high cut-off frequencies at 135 Hz and 600 Hz respectively, is used for robustness to suppress control spillover at out of band frequencies. This filter,  $W_\gamma(j\omega)$ , alongwith the Blaschke product,  $B_{cc}(j\omega)$ , formed from the local control path transfer function, is then used to compute the centre and radius of circles at discrete frequencies describing the regions of feasible local and remote vibration attenuation in the  $\gamma$ -plane, as given by (3.22) and (3.24).

The circles in the  $\gamma$ -plane for frequencies encompassing the first resonance of the beam are plotted in figure 5.8. It can be seen that the constraint regions describing

attenuation in remote output almost entirely overlap with the region corresponding to reduction in the local output. Hence, this confirms the prediction described in section 5.3 for frequencies near resonance. The optimal values for  $\gamma$  are selected from inside both circles for the discrete frequencies. A stable transfer function that interpolates through this  $\gamma$  data set is constructed next.

### 5.4.3 Interpolation of optimal $\gamma$ data values

The set of optimal  $\gamma$  data values is interpolated by a stable transfer function using the Nevanlinna Pick interpolation algorithm in a similar manner to the formulation presented in section 3.5.3. The Pick matrix associated with the optimal  $\gamma$  data values is given by (5.9). A stable function  $\gamma(j\omega)$  that interpolates the optimal data set is possible only if this pick matrix is positive definite.

$$P = \left[ \frac{1 - Z_k \bar{Z}_l}{s_k + \bar{s}_l} \right]_{k,l=1}^n = \left[ \frac{1 - \frac{\gamma_k \bar{\gamma}_l}{M M}}{\sigma + j\omega_k + (\sigma - j\omega_l)} \right]_{k,l=1}^n \quad (5.9)$$

A reduced data set containing only 5  $\gamma$  data values is used for interpolation. As the optimal  $\gamma$  values are selected from near the centre of circle which defines reduction at the local point, the maximum absolute optimal  $\gamma$  values is limited by the radius of this circle which is unity.

$$|\gamma(j\omega_i)| \leq 1, \quad \forall \omega_i \in 2\pi \times [270, 300]$$

The pick matrix is not positive definite for values of  $\sigma = 20$  and  $M = 1$  but the minimum eigenvalue of this matrix is -0.008. A smaller value of  $\sigma$  will increase the positive definiteness of the pick matrix, however, the approximation at intermediate frequencies will deteriorate as a result. Therefore, the set of  $\gamma$  values is slightly modified such that the Pick matrix is positive definite for  $\sigma = 20$  and  $M = 1$ . This modified set of  $\gamma$  values and the final operating  $\gamma$  values, which is the frequency response of the interpolated  $\gamma(j\omega)$  at the discrete frequencies, are plotted in figure 5.9. The modified values used for interpolation lie near the centre of the circles and the final operating points give a good approximation even at intermediate frequencies. The nyquist contour

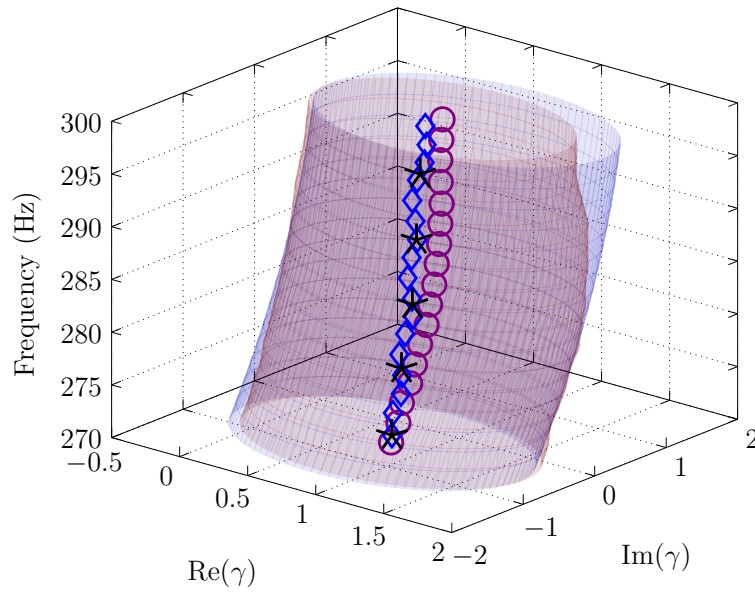


Figure 5.9: Portrayal of vibration attenuation at the local (blue) and remote (red) points as circles in  $\gamma$ -plane, initial set of optimal  $\gamma$  values ( $\circ$ ) and  $\gamma$  values used for interpolation after modification ( $\star$ ). The set of final operating  $\gamma$  values shown as  $\diamond$  is the frequency response of identified  $\gamma(s)$  which is interpolated using a value of  $\sigma = 20$  and  $M = 1$

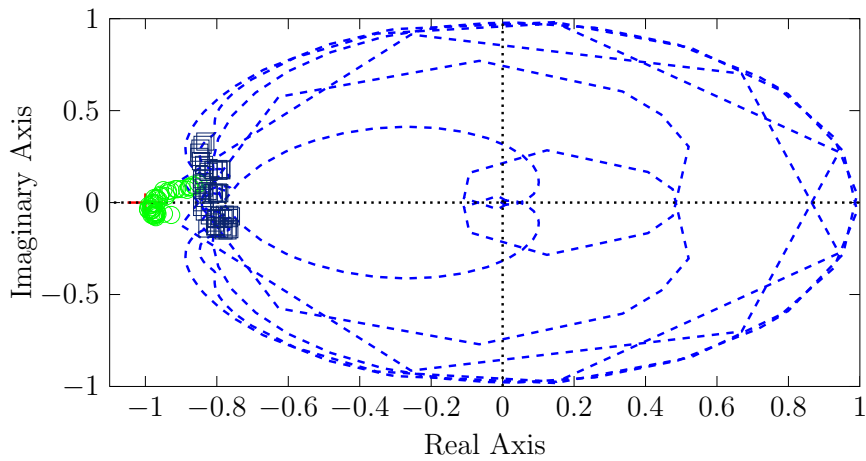


Figure 5.10: Nyquist plot of  $\gamma(s)B_{cc}(s)W_{\gamma}(s)$  interpolated using a value of  $\sigma = 20$ , also shown are the values of  $\gamma(j\omega_i)B_{cc}(j\omega_i)W_{\gamma}(j\omega_i)$  corresponding to the initial set of selected  $\gamma$  values ( $\circ$ ) and the final operating  $\gamma$  values ( $\square$ )

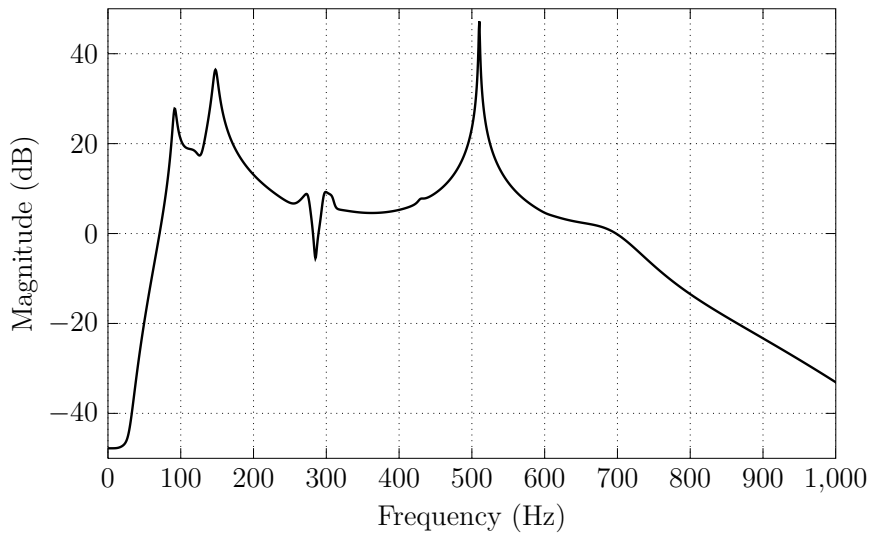


Figure 5.11: Magnitude frequency response of the designed controller

of  $\gamma(j\omega)B_{cc}(j\omega)W_\gamma(j\omega)$  which governs the stability of the controller does not enclose the  $-1$  point as shown in figure 5.10.

A controller is realised by substituting  $\gamma(j\omega)$  in (3.26). The magnitude of the frequency response of this controller is shown in figure 5.11. This starts to roll off after 600 Hz due to the filter action thereby improving robustness at higher frequencies. This response is used to estimate the theoretical closed loop frequency response of the local and remote outputs which predicts around 12 dB reduction close to resonance, as shown in figure 5.12 and figure 5.13.

#### 5.4.4 Experimental results

As the geometric control design is performed in the  $s$  domain, the controller is a continuous-time transfer function. In order to enable digital implementation, a discrete-time state space model of this compensator using a first order hold approximation with a sampling frequency of 4 kHz is obtained. A balanced state space realization such that the observability and controllability grammians of this discrete-time compensator are diagonal and equal is used. The magnitude and phase of the frequency response of the discrete-time compensator matches exactly with the continuous-time model which is necessary and sufficient. This compensator is then implemented in Simulink using a dSPACE real

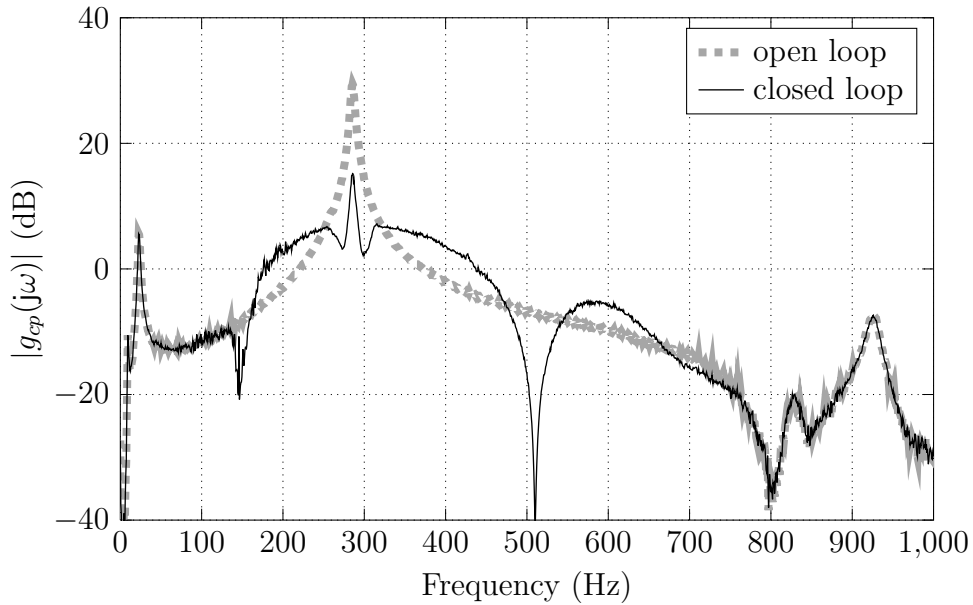


Figure 5.12: Theoretical estimation of the magnitude of the frequency response from primary excitation input to local output with (solid) and without (dashed) feedback control

time hardware interface to integrate it with the experimental set-up. The digital input signal is converted to analog voltage signal using a 16 bit digital to analog converter. The output from DAC is filtered and amplified before driving the shakers as shown in figure 5.5. The disturbance shaker is excited with different input signals for which the local and remote outputs are measured.

#### **Sinusoidal excitation at 283 Hz**

The power spectral density of the outputs obtained from accelerometers mounted on top of the beam is plotted in figure 5.14, for a 283 Hz sinusoidal primary excitation. This shows around 16 dB reduction in magnitude at this frequency compared with the open loop output. The power spectral density of outputs from accelerometers near the base of the isolation mounts is plotted in figure 5.15. This shows approximately 18 dB reduction in magnitude at this frequency compared with the open loop output.

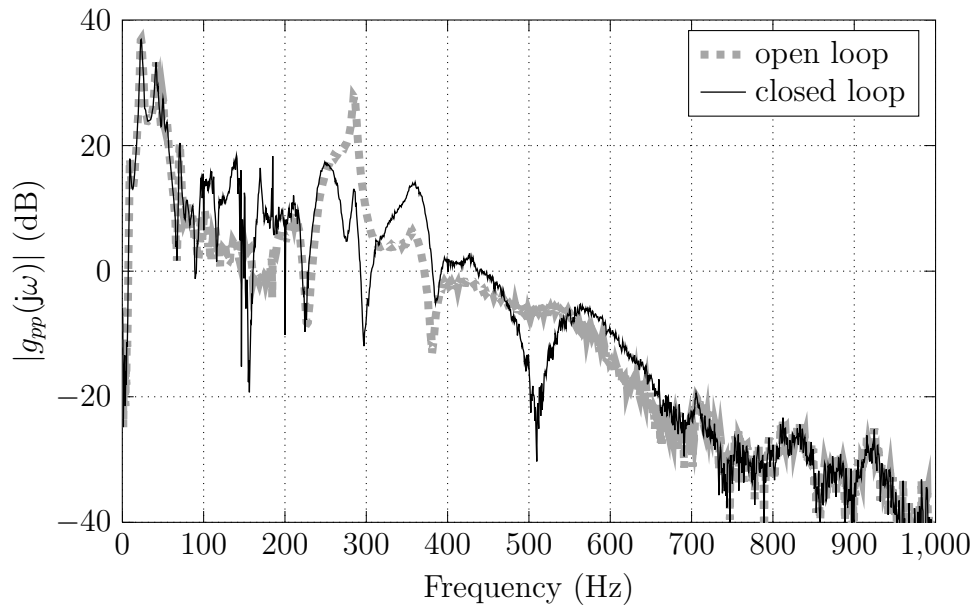


Figure 5.13: Theoretical estimation of the magnitude of the frequency response from primary excitation input to remote output with (solid) and without (dashed) feedback control

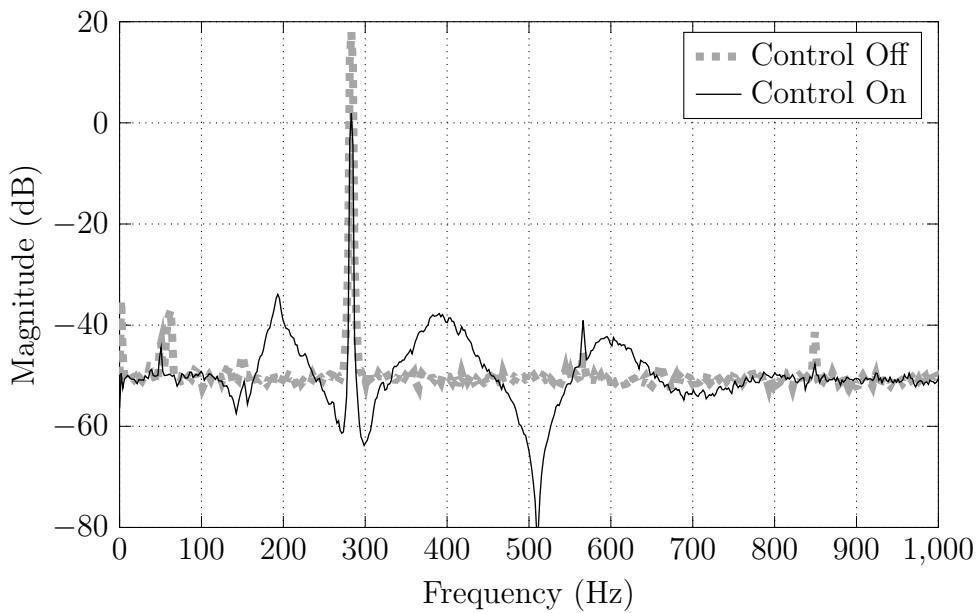


Figure 5.14: Power spectral density of the output on top of the beam for a sinusoidal excitation input with (solid) and without (dashed) feedback control

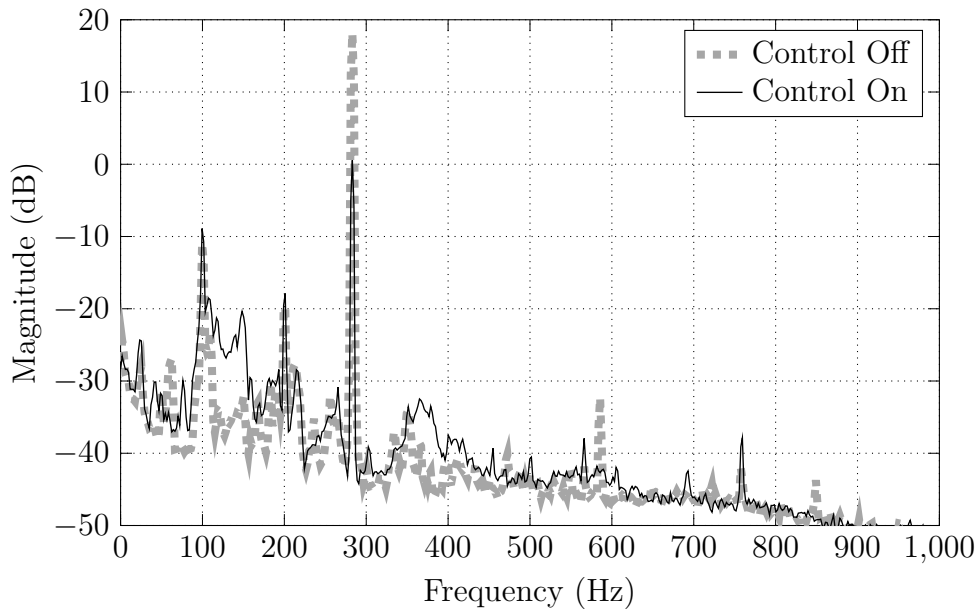


Figure 5.15: Power spectral density of the output at the base of the beam for a sinusoidal excitation input with (solid) and without (dashed) feedback control

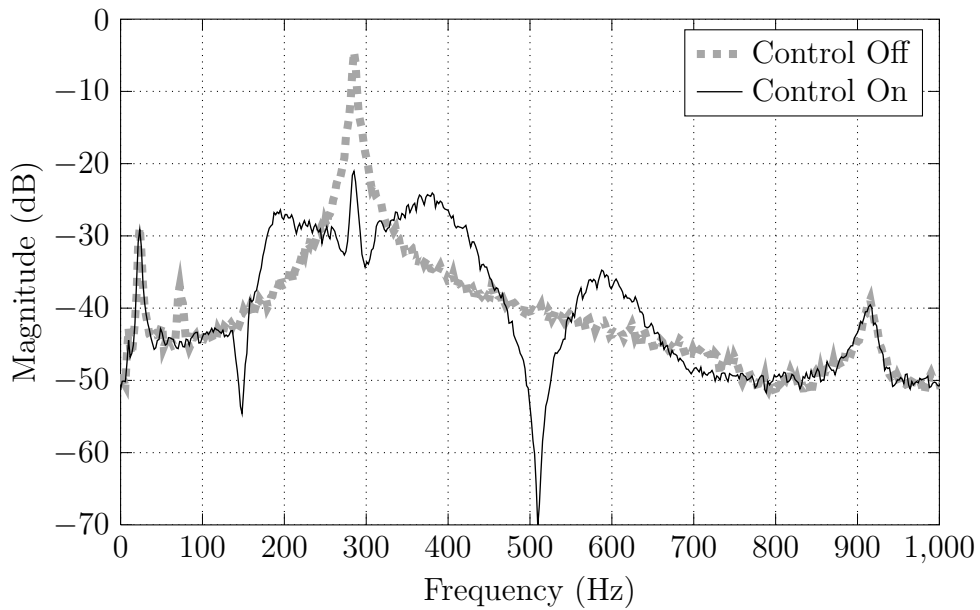


Figure 5.16: Power spectral density of the output on top of the beam for a random excitation input with (solid) and without (dashed) feedback control

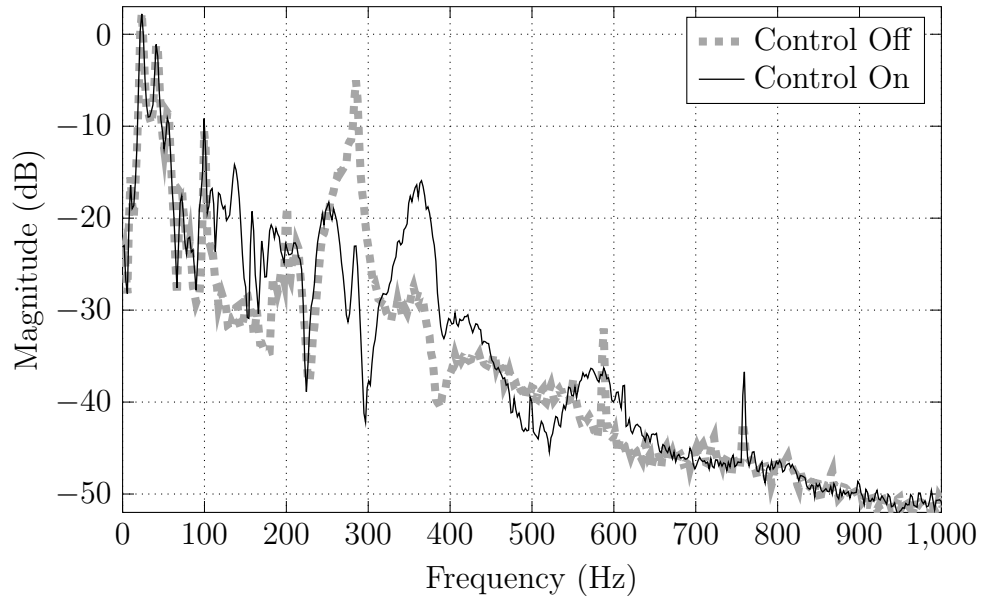


Figure 5.17: Power spectral density of the output at the base of the beam for a random excitation input with (solid) and without (dashed) feedback control

### White noise excitation

The disturbance shaker is excited with a white noise signal and the power spectral density of acceleration outputs on top of the beam,  $q_c(t)$ , is plotted in figure 5.16. As expected this also shows around 16 dB attenuation around the first resonant frequency. The power spectral density of the outputs near the base of the beam for the same excitation input is plotted in figure 5.17. The reduction at resonant frequency is almost 18 dB however there is an amplification of around 10 dB at 350 Hz.

## 5.5 Summary

It has been proven in this chapter that the value of design freedom that parameterises a reduction in the output at any remote point, for frequencies close to resonance, lies at the centre of the circle that depicts reduction in output at the local point. Therefore, a controller that achieves attenuation locally for frequencies close to resonance would also invariably reduce the response at all other points that is not on a node of that mode. The region of overlap corresponding to reduction in output at the local and

remote points reduces as the frequency moves away from resonance. This shows the difficulty in achieving good response at all points using any SISO control design when the excitation frequency is not close to a structural bending mode frequency. It also shows that active damping of a structural resonance using a single sensor and actuator pair on a structure can be achieved using the geometric based control design. This is experimentally validated on a beam rig. The optimal value for design freedom parameter that achieves reduction in a local output near the first bending mode resonant frequency has been shown to also achieve good attenuation of the remote output.

# Chapter 6

## Global Vibration Reduction

### 6.1 Introduction

The analytical proof presented in section 5.2 of chapter 5 is used in this chapter to investigate the feasibility of the geometric based approach for global vibration reduction. A reasonable indicator for the global response level of the whole structure is its kinetic energy. It can be measured relatively easily using laser vibrometers for simple structures, such as flat panels [Rohlfing et al., 2011b]. As the vibration energy propagates it can excite attached structures that are removed from the source of disturbance. Therefore, it is important to control the total vibration energy of the system. An effective method to reduce the global response is achieved by increasing the damping of structural resonances. A few of the active damping methods have been discussed in section 5.2 of chapter 5. The simplest of these methods involves electronically multiplying the measured velocity at a point by a fixed gain and feeding the resultant as a control signal to a closely located actuator, which is commonly termed as direct velocity feedback control.

There are many works based on direct velocity feedback control methods for minimising the kinetic energy and minimising the sound radiation from flat panels [Elliott et al., 2002; Fahy and Gardonio, 2007; Gardonio et al., 2004]. In an ideal case, direct velocity feedback control is unconditionally stable for very high feedback gains using collocated sensor and actuator pairs. However, for a good collocated arrangement, point force actuators such as inertial electrodynamic shakers employed with velocity sensors add significant weight to the lightweight host structure. This defeats the ob-

jective of minimal structural modification intended with active control as opposed to passive methods. On the other hand, strain actuators such as piezoelectric patch actuators are lighter and have been used for direct velocity feedback control of lightweight structures [Hong et al., 2007]. However, it is more difficult to achieve collocation and duality in this case since the forces are provided by a distribution of moments.

Besides the issue of non-collocation and non-duality, the closed loop stability is also affected by the dynamics of different components in the feedback path, namely, transducer dynamics and the time lags in the electronic instrumentation which together add phase lag at low and high frequencies in the local control path. The implications of this on geometric control design has been discussed extensively in section 2.3 of chapter 2. Nevertheless, significant reduction in the total kinetic energy has been achieved using direct velocity feedback control methods for very high values of feedback gains [Gatti et al., 2007].

However, it has been shown in [Gardonio and Elliott, 2005] that direct velocity feedback control would pin the structure at the location of the control actuator for very high control gains which leads to new resonant modes passing through this point as a node. The new resonant peaks in the total kinetic energy spectrum appears at the antiresonant frequencies of the local control input to sensor path transfer function. As a result, the total kinetic energy level of the structure starts to increase for increasing values of feedback gain beyond a certain optimum value. The power absorbed by a control loop also starts to decrease close to this optimum value of gain. Using this principle, the gains of individual feedback loops can be tuned to achieve an optimum value of the kinetic energy [Zilletti et al., 2010].

In this chapter, the geometric based approach is used to design a controller for kinetic energy reduction. It was shown in section 5.3 of chapter 5 that the optimal value for  $\gamma$  close to resonance that achieves maximum reduction in output at the local point also corresponds to a reduction in response level at the remote points. This principle is utilised for the selection of optimal values for the design parameter and subsequent realisation of a controller. This method is compared with the direct velocity feedback control for a lightly damped model of a beam. The limitations of maximum gain for closed loop stability and the problem of new resonant peaks is also investigated using this method.

## 6.2 Design parameter for direct velocity feedback control

The drawbacks of direct velocity feedback control pertaining to the stability and inducement of new resonance can potentially be avoided using the geometric based approach. This is explored in terms of the location of  $\gamma$  value in the  $\gamma$ -plane for increasing values of control gain. This is considered for a  $2 \times 2$  system assuming that the multivariable system matrix is composed of receptance functions.

$$\begin{bmatrix} \tilde{q}_c(j\omega) \\ q_p(j\omega) \end{bmatrix} = \begin{bmatrix} \tilde{g}_{cc}(j\omega) & \tilde{g}_{cp}(j\omega) \\ \tilde{g}_{pc}(j\omega) & \tilde{g}_{pp}(j\omega) \end{bmatrix} \begin{bmatrix} \tilde{f}_c(j\omega) \\ f_p(j\omega) \end{bmatrix} \quad (6.1)$$

The control input for direct velocity feedback is given as

$$f_c(j\omega) = -Cj\omega q_c(j\omega) \quad (6.2)$$

where  $C$  is the constant value of feedback gain. The closed loop output at the local point is then given as

$$q_c(j\omega) = \frac{\tilde{g}_{cp}(j\omega)}{1 + j\omega C \tilde{g}_{cc}(j\omega)} f_p(j\omega) \quad (6.3)$$

The relationship between the sensitivity function and the design parameter can be used to express the latter as a function of the direct velocity feedback controller gain as

$$\gamma(j\omega) = \frac{-1}{B_{cc}(j\omega)W_\gamma(j\omega)} \frac{\tilde{g}_{cc}(j\omega)j\omega C}{1 + \tilde{g}_{cc}(j\omega)j\omega C} \quad (6.4)$$

or alternatively as

$$\gamma(j\omega) = \frac{-1}{B_{cc}(j\omega)W_\gamma(j\omega)} \frac{1}{\frac{1}{\tilde{g}_{cc}(j\omega)j\omega C} + 1} \quad (6.5)$$

Assuming that the transducers are perfectly collocated and the system is unconditionally stable then it can be seen from Eq.(6.5) that when

$$C \rightarrow \infty$$

$$\Rightarrow \gamma(j\omega) \rightarrow \frac{-1}{B_{cc}(j\omega)W_\gamma(j\omega)}$$

It can be observed that as the control gain is increased, the design parameter  $\gamma$  moves from the origin for low gain to the centre of the circle describing a reduction in output at the local point for very large gains. Whilst these circular regions in the  $\gamma$ -plane are depicted only for discrete frequencies, the overall effect of high feedback gain is to reduce the output at the local point in the entire frequency spectrum. As the circles corresponding to a reduction in output at the remote points do not overlap with those of the local point for all frequencies, very large feedback gains do not ensure good global response.

It has been established in section 5.3 circular region describing attenuation at the remote point for resonant frequencies in the  $\gamma$ -plane overlap with those of the local point. Hence, the resonant peaks in the total kinetic energy reduces for increasing gain. However, for frequencies close to the frequency of the zeros these circular regions are removed from each other and do not overlap. Therefore, the amplitude of vibration increases at the remote points and new resonant peaks appear in the total kinetic energy spectrum. A controller based on the geometric technique can be developed such that the optimal value for  $\gamma$  is selected for maximum reduction of resonant peaks without increasing the amplitude of vibration at the antiresonant frequencies. It can be devised by exerting very low dissipation of energy at the frequencies of the zeros while increasing the dissipation of energy at resonance.

### 6.3 Control design for kinetic energy reduction

The geometric technique for kinetic energy reduction is illustrated in this section and is compared with the direct velocity feedback control method using the model of the beam described in section 3.5.1 of chapter 3. As the control input is not collocated with the feedback sensor in this arrangement, the maximum stable gain for direct velocity feedback is used for comparison with the geometric based method.

The geometric based technique for kinetic energy reduction is implemented by selecting the optimal set of  $\gamma$  values for certain frequencies inside a limited bandwidth. This is selected as the centre of the circle for local vibration reduction for the first four resonant frequencies. At the frequencies of the first three lightly damped zeros of the

### 6.3. KINETIC ENERGY REDUCTION

local control path transfer function, it is selected from near the origin in the  $\gamma$ -plane. The filter for robustness is chosen as a fourth order low pass butterworth filter with a high cut off frequency of 1.35 kHz.

This optimal set of  $\gamma$  data values is interpolated by a stable transfer function  $\gamma(j\omega)$  using the Nevanlinna Pick interpolation algorithm. A controller is implemented in terms of the identified design parameter transfer function which is then used to compute the kinetic energy spectrum of the beam.

The total kinetic energy of the beam with no control is calculated from the modal mobility excitation vector due to only the primary excitation [Fuller et al., 1997] as

$$E_{OL}(\omega) = \frac{1}{4}m\mathbf{a}_p^H(\omega)\mathbf{a}_p(\omega) \quad (6.6)$$

where  $m$  is the total mass of the beam and  $\mathbf{a}_p(\omega)$  is the column vector of modal mobility excitations of the flexural modes of the beam due to the primary force excitation. Its elements are calculated according to

$$a_p(\omega) = \frac{2\psi_{pk}}{m_k[-\omega^2 + j2\zeta_k\omega_k\omega + \omega_k^2]} \quad (6.7)$$

where  $\psi_{pk}$  is the  $p$ th element in the mode shape vector  $\boldsymbol{\psi}_k$ ,  $\zeta_k$  is the modal damping ratio,  $m_k$  is the modal mass and  $\omega_k$  is the natural frequency of the  $k$ th mode. The total kinetic energy of the beam using a feedback controller  $k(\omega)$  is calculated as

$$E_{CL}(\omega) = \frac{1}{4}m \left[ \mathbf{a}_p^H(\omega) + \frac{k^*(\omega)\tilde{g}_{cp}^*(\omega)}{1 + k^*(\omega)\tilde{g}_{cc}^*(\omega)} \mathbf{a}_c^H(\omega) \right] \left[ \mathbf{a}_p(\omega) + \mathbf{a}_c(\omega) \frac{k(\omega)\tilde{g}_{cp}(\omega)}{1 + k(\omega)\tilde{g}_{cc}(\omega)} \right] \quad (6.8)$$

where  $\mathbf{a}_c(\omega)$  is the column vector of modal mobility excitations due to the control force which is computed as

$$a_c(\omega) = \frac{2\psi_{ck}}{m_k[-\omega^2 + j2\zeta_k\omega_k\omega + \omega_k^2]} \quad (6.9)$$

The superscript  $*$  denotes complex conjugate and  $^H$  denotes hermitian transpose of the vector and the notations have their usual meaning.

The geometric based control design achieves significant reduction in the kinetic energy of the beam as seen from its plot in figure 6.1. The direct velocity feedback con-

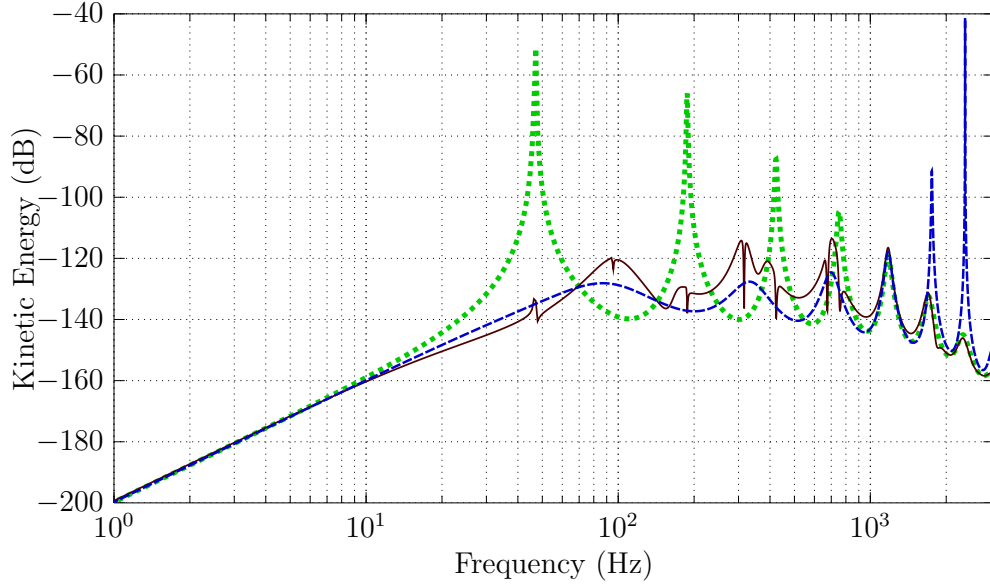


Figure 6.1: Kinetic energy spectrum of the beam with no control (green dotted), direct velocity feedback control with maximum stable gain (blue dashed) and geometric based control design (solid red)

troller is only conditionally stable for this high value of feedback gain. In practice, the actuator dynamics further restricts this amount of gain. The geometric control design, on the other hand, ensures closed loop stability even in the presence of unmodelled actuator dynamics.

The minimum value of kinetic energy can be calculated in terms of the vector of control force distributions [Fuller et al., 1997]. Using the relation between the control force and the design parameter, the kinetic energy in Eq(6.8) has a global minimum when the design parameter is given by

$$\gamma(\omega) = - [a_c^H(\omega)a_c(\omega)]^{-1} a_c^H(\omega)a_p(\omega) \frac{\hat{g}_{cc}(\omega)}{\hat{g}_{cp}(\omega)} \quad (6.10)$$

The value of the design parameter for this minimum kinetic energy is compared with the optimal selection of  $\gamma$  values for the first two resonant and the first two antiresonant frequencies in the  $\gamma$ -plane and plotted in figures 6.2 and 6.3, respectively. The value of the design parameter that corresponds to the minimum kinetic energy approaches near the origin for the frequency of the zeros, whereas for the resonant frequencies it approaches near the centre of local vibration reduction circle. This shows the validity of

### 6.3. KINETIC ENERGY REDUCTION

the design rules using  $\gamma$  values for designing a controller for kinetic energy reduction.

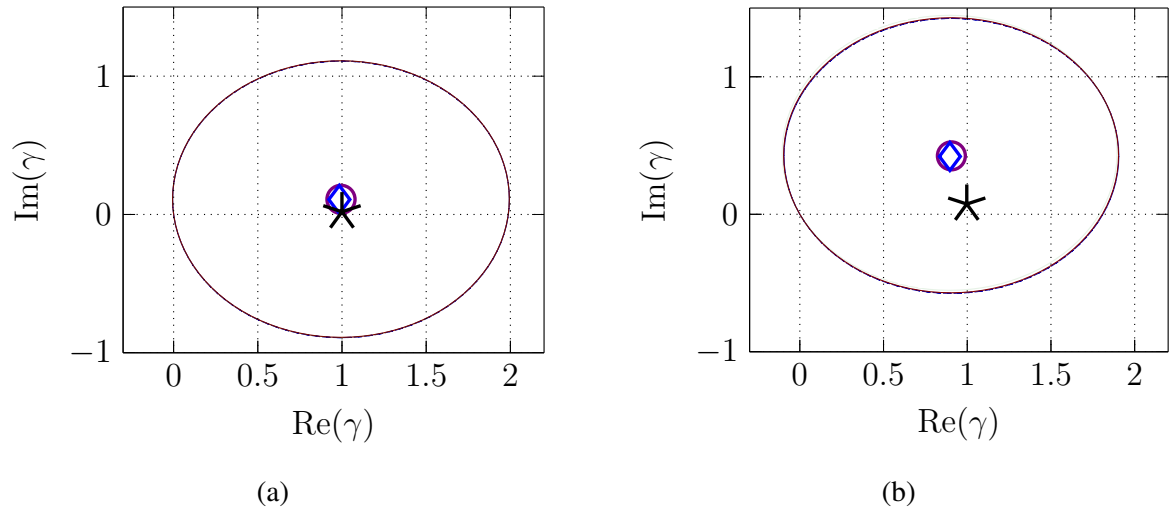


Figure 6.2: Value of  $\gamma$  that corresponds to minimum kinetic energy ( $\star$ ), the selected values for geometric control design ( $\diamond$ ) and the centre of circles for local vibration reduction ( $\circ$ ) plotted for (a) the first resonant frequency of 47 Hz and (b) second resonant frequency 187 Hz

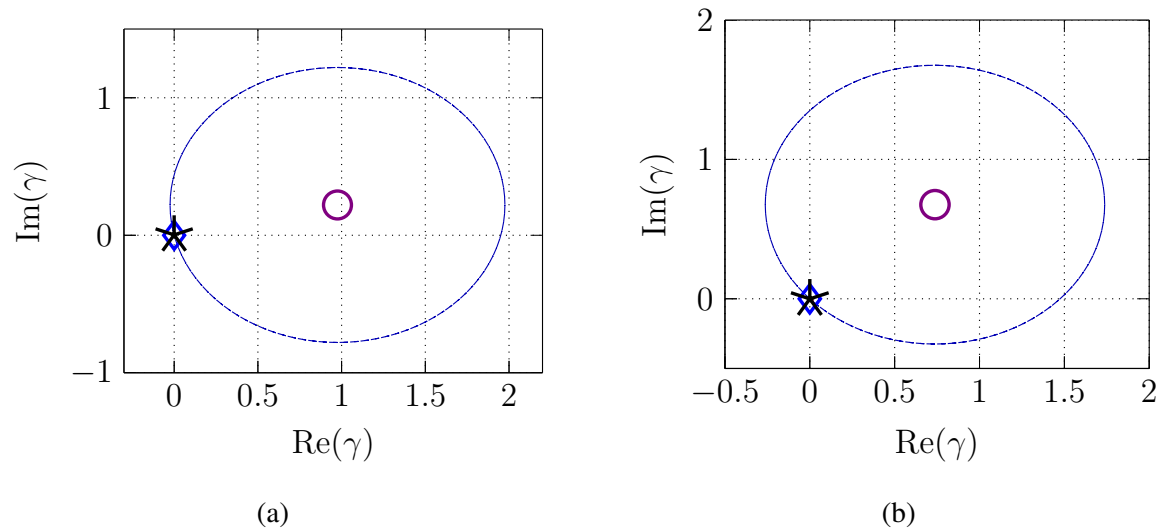


Figure 6.3: Value of  $\gamma$  that corresponds to minimum kinetic energy ( $\star$ ), the selected values for geometric control design ( $\diamond$ ) and the centre of circles for local vibration reduction ( $\circ$ ) plotted for the frequency of (a) the first complex zeros 95 Hz and (b) the second zeros 316 Hz

## 6.4 Summary

In this chapter the effect of increasing the gain in a direct velocity feedback configuration on the kinetic energy has been shown, using the evolution of the corresponding design parameter values in the complex plane. Kinetic energy reduction performance deteriorates due to a pinning action at the local control point for very large values of feedback gain and the new peaks appear at the frequencies of the lightly damped zeros of the local control path transfer function. A geometric based controller can be designed for kinetic energy reduction using the information at these frequencies. As the dissipation of energy using a controller thus implemented depends on the value of the design parameter in the  $\gamma$ -plane, the available design freedom for attenuation at the local and remote points can be specified for frequencies near resonance and antiresonance. This approach is compared with an ideal direct velocity feedback controller for its maximum stable gain using a numerical example. The geometric based controller achieves good broadband kinetic energy reduction for this lightly damped beam model.

# Chapter 7

## Multi-loop Sequential Loop Closing Control Design

### 7.1 Introduction

The geometric based approach for a stable feedback controller design is extended to the design of multiple local feedback loops in this chapter. Several error sensors and control actuators can then be incorporated on to a large structure for desired remote vibration attenuation. A theoretical formulation for the design of multiple control loops is provided, followed by an experimental implementation involving the design of two sequential loops. A controller for a SISO loop is implemented in terms of a single design parameter that defines the feasible vibration attenuation at multiple locations solely due to this control action. Distinct design parameters for each control loop are used to construct each local feedback controller. Values for these design freedom variables that parameterise feasible vibration attenuation are selected for each control loop separately from different complex planes. These variables can then be selected to achieve various control objectives, such as minimum interaction with other control loops at certain frequencies or to enhance vibration attenuation at additional locations where simultaneous attenuation is not possible using the available control action. The robustness of individual loops to failure will also be examined.

Although the geometric design method is not suitable for a centralised control approach, there are many other control design methods that can be used to design a

centralised control scheme for vibration attenuation using multiple sensors and actuators. Robust controller design methods for vibration attenuation using similar control schemes have been extensively presented in the literature, see for example [Gawronski, 2004; Liu and Hou, 2004]. A centralised control scheme requires the sensor measurement at any location for the computation of control action at some other or more than one location. This poses hardware limitations for many AVC applications when the sensor measurement and control actuation are separated by large distances. Mitigation of vibration on the hull of ships using a centralised controller, for example, would require long wiring between distantly located sensors, a centralised controller and actuators. Although the extra time delay does not significantly affect the control design, excessive wiring and hardware is also undesirable for the vibration mitigation of large span floors in buildings and stadia. Moreover, the stability and performance of a centralised scheme with multiple sensors and actuators is prone to several external factors. A single sensor or actuator failure could aggravate the performance at more than one location.

A de-centralised control scheme, on the other hand, uses only the local measurement as a feedback signal for the actuator. This avoids the need for extensive wiring to connect the controller with the sensor and actuator. Furthermore, the individual feedback loops are closed loop stable and can also be made unsusceptible to the failure of any other feedback loops. This allows for convenient testing and implementation of additional controllers on the structure. Therefore, a de-centralised scheme is more appropriate for active vibration control applications.

## 7.2 Sequential Loop Closing Control Design

In this section, a geometric approach for controller design is discussed for the vibration attenuation problem where control action is applied at more than one point. Since the design freedom parameterises feasible vibration attenuation only for a SISO local feedback loop, a decentralised control design technique is pursued for the design of control systems at multiple locations. This is a decentralised independent control design approach and can be made robust to instabilities due to the failure of individual control loops.

Sequential loop closing control design using the geometric technique is presented here for a system with two local feedback loops. The extension to three or more local

feedback loops is straightforward. The vibration measurement from the two error sensors are denoted as  $q_{e_1}$  and  $q_{e_2}$  while the control force acting at the respective locations are denoted as  $f_{c_1}$  and  $f_{c_2}$ . The error sensor and control actuator for both loops are assumed to be slightly non-collocated to admit the non-minimum phase characteristics encountered in practical situations. A primary excitation force denoted as  $f_p$  acts at a remote location and the vibration response at this point is denoted as  $q_p$ . The open loop transfer function matrix relating the various inputs and outputs is denoted as (7.1).

$$\begin{bmatrix} q_{e_1}(j\omega) \\ q_{e_2}(j\omega) \\ q_p(j\omega) \end{bmatrix} = \begin{bmatrix} g_{aa}(j\omega) & g_{ab}(j\omega) & g_{ac}(j\omega) \\ g_{ba}(j\omega) & g_{bb}(j\omega) & g_{bc}(j\omega) \\ g_{ca}(j\omega) & g_{cb}(j\omega) & g_{cc}(j\omega) \end{bmatrix} \begin{bmatrix} f_{c_1}(j\omega) \\ f_{c_2}(j\omega) \\ f_p(j\omega) \end{bmatrix} \quad (7.1)$$

### 7.2.1 Control system design for the first loop

Initially, a feedback control system only for the first loop is designed such that the control action is given as  $f_{c_1}(j\omega) = -k_1(j\omega)q_{e_1}(j\omega)$ . The control law for determining the second input is undefined at this stage and it will be expressed as  $f_{c_2}(j\omega)$ . The closed loop response due to the control action of the first loop is then given by

$$q_{e_1}(j\omega) = \frac{g_{ab}(j\omega)f_{c_2}(j\omega) + g_{ac}(j\omega)f_p(j\omega)}{1 + g_{aa}(j\omega)k_1(j\omega)} \quad (7.2)$$

$$\begin{aligned} q_{e_2}(j\omega) = & \left[ g_{bb}(j\omega) - \frac{g_{ba}(j\omega)k_1(j\omega)g_{ab}(j\omega)}{1 + g_{aa}(j\omega)k_1(j\omega)} \right] f_{c_2}(j\omega) \\ & + \left[ g_{bc}(j\omega) - \frac{g_{ba}(j\omega)k_1(j\omega)g_{ac}(j\omega)}{1 + g_{aa}(j\omega)k_1(j\omega)} \right] f_p(j\omega) \end{aligned} \quad (7.3)$$

$$\begin{aligned} q_p(j\omega) = & \left[ g_{cb}(j\omega) - \frac{g_{ca}(j\omega)k_1(j\omega)g_{ab}(j\omega)}{1 + g_{aa}(j\omega)k_1(j\omega)} \right] f_{c_2}(j\omega) \\ & + \left[ g_{cc}(j\omega) - \frac{g_{ca}(j\omega)k_1(j\omega)g_{ac}(j\omega)}{1 + g_{aa}(j\omega)k_1(j\omega)} \right] f_p(j\omega) \end{aligned} \quad (7.4)$$

The local closed loop transfer function at point 1 is denoted in terms of a design freedom parameter as

$$\gamma_{a_1}(j\omega)W_{a_1}(j\omega)B_{a_1}(j\omega) = -\frac{g_{aa}(j\omega)k_1(j\omega)}{1 + g_{aa}(j\omega)k_1(j\omega)} \quad (7.5)$$

where  $B_{a_1}(j\omega)$  is the all-pass transfer function formed from the RHP zeros of the non-minimum phase control path transfer function and  $W_{a_1}(j\omega)$  is a weighting filter to suppress spillover at out-of-bound frequencies.  $g_{aa}(j\omega)$  can be factorised as a minimum phase counterpart  $\hat{g}_{aa}(j\omega)$  with all its RHP zeros reflected into the LHP and an all pass transfer function as given in (7.6).

$$g_{aa}(j\omega) = \hat{g}_{aa}(j\omega)B_{a_1}(j\omega) \quad (7.6)$$

The numerical subscript with the design parameter and the Blaschke product denotes the numerical order of the current loop in the multi-loop sequential design. Substituting (7.5) in the equations for the closed loop transfer functions in (7.2), (7.3) and (7.4) gives

$$\begin{bmatrix} q_{e_1}(j\omega) \\ q_{e_2}(j\omega) \\ q_p(j\omega) \end{bmatrix} = \begin{bmatrix} h_{ab}(j\omega) & h_{ac}(j\omega) \\ h_{bb}(j\omega) & h_{bc}(j\omega) \\ h_{cb}(j\omega) & h_{cc}(j\omega) \end{bmatrix} \begin{bmatrix} f_{c_2}(j\omega) \\ f_p(j\omega) \end{bmatrix} \quad (7.7)$$

where

$$h_{ab}(j\omega) = [1 + \gamma_{a_1}(j\omega)W_{a_1}(j\omega)B_{a_1}(j\omega)] g_{ab}(j\omega) \quad (7.8)$$

$$h_{ac}(j\omega) = [1 + \gamma_{a_1}(j\omega)W_{a_1}(j\omega)B_{a_1}(j\omega)] g_{ac}(j\omega) \quad (7.9)$$

$$h_{bb}(j\omega) = \left[ 1 + \gamma_{a_1}(j\omega)W_{a_1}(j\omega)B_{a_1}(j\omega) \frac{g_{ba}(j\omega)g_{ab}(j\omega)}{g_{aa}(j\omega)g_{bb}(j\omega)} \right] g_{bb}(j\omega) \quad (7.10)$$

$$h_{bc}(j\omega) = \left[ 1 + \gamma_{a_1}(j\omega)W_{a_1}(j\omega)B_{a_1}(j\omega) \frac{g_{ba}(j\omega)g_{ac}(j\omega)}{g_{aa}(j\omega)g_{bc}(j\omega)} \right] g_{bc}(j\omega) \quad (7.11)$$

$$h_{cb}(j\omega) = \left[ 1 + \gamma_{a_1}(j\omega)W_{a_1}(j\omega)B_{a_1}(j\omega) \frac{g_{ca}(j\omega)g_{ab}(j\omega)}{g_{aa}(j\omega)g_{cb}(j\omega)} \right] g_{cb}(j\omega) \quad (7.12)$$

$$h_{cc}(j\omega) = \left[ 1 + \gamma_{a_1}(j\omega)W_{a_1}(j\omega)B_{a_1}(j\omega) \frac{g_{ca}(j\omega)g_{ac}(j\omega)}{g_{aa}(j\omega)g_{cc}(j\omega)} \right] g_{cc}(j\omega) \quad (7.13)$$

The attenuation in output  $q_p(j\omega)$  using control action  $f_{c_1}(j\omega)$  results from a reduction

## 7.2. DECENTRALISED MIMO DESIGN

in the magnitude of the partial closed loop transfer function  $h_{cc}(j\omega)$  relative to the open loop transfer function  $g_{cc}(j\omega)$ , which can be expressed as (7.14).

$$\left| \frac{h_{cc}(j\omega)}{g_{cc}(j\omega)} \right| < 1 \quad (7.14)$$

Substituting from (7.13) in (7.14) gives

$$\left| 1 + \gamma_{a_1}(j\omega)W_{a_1}(j\omega)B_{a_1}(j\omega)\frac{g_{ca}(j\omega)g_{ac}(j\omega)}{g_{aa}(j\omega)g_{cc}(j\omega)} \right| < 1 \quad (7.15)$$

or alternatively as

$$\left| \gamma_{a_1}(j\omega) + \frac{g_{aa}(j\omega)g_{cc}(j\omega)}{W_{a_1}(j\omega)B_{a_1}(j\omega)g_{ca}(j\omega)g_{ac}(j\omega)} \right| < \left| \frac{g_{aa}(j\omega)g_{cc}(j\omega)}{W_{a_1}(j\omega)B_{a_1}(j\omega)g_{ca}(j\omega)g_{ac}(j\omega)} \right| \quad (7.16)$$

Inequality (7.16) evaluated at a discrete frequency  $\omega_i$  represents the region inside a circle in a complex  $\gamma_{a_1}$  - plane with centre

$$-\frac{g_{aa}(j\omega_i)g_{cc}(j\omega_i)}{W_{a_1}(j\omega_i)B_{a_1}(j\omega_i)g_{ca}(j\omega_i)g_{ac}(j\omega_i)}$$

and radius

$$\left| \frac{g_{aa}(j\omega_i)g_{cc}(j\omega_i)}{W_{a_1}(j\omega_i)B_{a_1}(j\omega_i)g_{ca}(j\omega_i)g_{ac}(j\omega_i)} \right|$$

. Any value for  $\gamma_{a_1}$  from inside this circle used in the implementation of a controller as (7.17) will achieve attenuation in  $q_p$  at that frequency.

$$k_1(j\omega) = \frac{-\gamma_{a_1}(j\omega)W_{a_1}(j\omega)}{(1 + \gamma_{a_1}(j\omega)W_{a_1}(j\omega)B_{a_1}(j\omega))\hat{g}_{aa}(j\omega)} \quad (7.17)$$

Similarly, attenuation in outputs  $q_{e_1}$  and  $q_{e_2}$  can be represented as inequalities (7.18) and (7.19), respectively

$$\left| \gamma_{a_1}(j\omega) + \frac{1}{W_{a_1}(j\omega)B_{a_1}(j\omega)} \right| < \left| \frac{1}{W_{a_1}(j\omega)B_{a_1}(j\omega)} \right| \quad (7.18)$$

$$\left| \gamma_{a_1}(j\omega) + \frac{g_{aa}(j\omega)g_{bc}(j\omega)}{W_{a_1}(j\omega)B_{a_1}(j\omega)g_{ba}(j\omega)g_{ac}(j\omega)} \right| < \left| \frac{g_{aa}(j\omega)g_{bc}(j\omega)}{W_{a_1}(j\omega)B_{a_1}(j\omega)g_{ba}(j\omega)g_{ac}(j\omega)} \right| \quad (7.19)$$

If the region of these circles in the  $\gamma_{a_1}$  plane is such that simultaneous vibration attenuation at one or more point results in deterioration at any other point, then a value for  $\gamma_{a_1}$  used for controller implementation in (7.17) can be sought such that it augments design of the second control system for simultaneous attenuation at all the points.

### 7.2.2 Control system design for the second feedback loop

A control system for the second feedback loop is designed using the partially closed loop system in (7.7) and the performance of this closed loop system is denoted in terms of a second variable  $\gamma_{b_2}$  as

$$\gamma_{b_2}(j\omega)W_{b_2}(j\omega)B_{b_2}(j\omega) = -\frac{h_{bb}(j\omega)k_2(j\omega)}{1 + h_{bb}(j\omega)k_2(j\omega)} \quad (7.20)$$

where  $B_{b_2}(j\omega)$  is obtained from factorization of the second local control loop non-minimum phase transfer function as

$$h_{bb}(j\omega) = \hat{h}_{bb}(j\omega)B_{b_2}(j\omega)$$

The numerical subscript for the design parameter and the blaschke product is used to denote that this feedback loop is implemented after the first feedback loop is closed. It should be noted that  $B_{b_2}(j\omega)$  contains the RHP zeros of the second open loop control path transfer function, i.e. RHP zeros of  $g_{bb}(j\omega)$  and the additional RHP zeros introduced by the term  $\left(1 + \gamma_{a_1}(j\omega)W_{a_1}(j\omega)B_{a_1}(j\omega)\frac{g_{ba}(j\omega)g_{ab}(j\omega)}{g_{aa}(j\omega)g_{bb}(j\omega)}\right)$ , which is due to the first feedback loop.

The closed loop transfer function matrix after substitution of the second feedback con-

control action in terms of this design parameter in (7.7) gives

$$\begin{bmatrix} q_{e_1}(j\omega) \\ q_{e_2}(j\omega) \\ q_p(j\omega) \end{bmatrix} = \begin{bmatrix} \left(1 + \gamma_{b_2}(j\omega)W_{b_2}(j\omega)B_{b_2}(j\omega)\frac{h_{ab}(j\omega)h_{bc}(j\omega)}{h_{bb}(j\omega)h_{ac}(j\omega)}\right) h_{ac}(j\omega) \\ (1 + \gamma_{b_2}(j\omega)W_{b_2}(j\omega)B_{b_2}(j\omega)) h_{bc}(j\omega) \\ \left(1 + \gamma_{b_2}(j\omega)W_{b_2}(j\omega)B_{b_2}(j\omega)\frac{h_{cb}(j\omega)h_{bc}(j\omega)}{h_{bb}(j\omega)h_{cc}(j\omega)}\right) h_{cc}(j\omega) \end{bmatrix} \begin{bmatrix} f_p(j\omega) \end{bmatrix} \quad (7.21)$$

In a similar fashion to the vibration attenuation conditions postulated in terms of regions in the  $\gamma_{a_1}$ -plane for the first control loop, closed loop reduction in  $q_{e_1}$ ,  $q_{e_2}$  and  $q_p$  at a discrete frequency for the second control loop can be represented as regions inside circles in the  $\gamma_{b_2}$ -plane given by inequalities (7.22), (7.23) and (7.24), respectively

$$\left| \gamma_{b_2}(j\omega) + \frac{h_{bb}(j\omega)h_{ac}(j\omega)}{W_{b_2}(j\omega)B_{b_2}(j\omega)h_{ab}(j\omega)h_{bc}(j\omega)} \right| < \left| \frac{h_{bb}(j\omega)h_{ac}(j\omega)}{W_{b_2}(j\omega)B_{b_2}(j\omega)h_{ab}(j\omega)h_{bc}(j\omega)} \right| \quad (7.22)$$

$$\left| \gamma_{b_2}(j\omega) + \frac{1}{W_{b_2}(j\omega)B_{b_2}(j\omega)} \right| < \left| \frac{1}{W_{b_2}(j\omega)B_{b_2}(j\omega)} \right| \quad (7.23)$$

$$\left| \gamma_{b_2}(j\omega) + \frac{h_{bb}(j\omega)h_{cc}(j\omega)}{W_{b_2}(j\omega)B_{b_2}(j\omega)h_{cb}(j\omega)h_{bc}(j\omega)} \right| < \left| \frac{h_{bb}(j\omega)h_{cc}(j\omega)}{W_{b_2}(j\omega)B_{b_2}(j\omega)h_{cb}(j\omega)h_{bc}(j\omega)} \right| \quad (7.24)$$

A controller for the second control loop is then implemented in terms of the optimally selected and interpolated  $\gamma_{b_2}(j\omega)$  transfer function as (7.25)

$$k_2(j\omega) = \frac{-\gamma_{b_2}(j\omega)W_{b_2}(j\omega)}{(1 + \gamma_{b_2}(j\omega)W_{b_2}(j\omega)B_{b_2}(j\omega)) \hat{h}_{bb}(j\omega)} \quad (7.25)$$

### 7.2.3 Integrity when inner feedback loop fails

One of the disadvantages of sequential loop closing design is that the stability of individual control loops is not guaranteed when other feedback loops fail. This is termed as integrity in the literature [Skogestad and Postlethwaite, 2005]. In this section, taking the example case of the  $3 \times 3$  system in (7.1), conditions are formulated such that when an inner feedback loop breaks then subject to certain conditions being met, individual control loops will be tolerant to this failure.

The controller for loop 2 is designed for the partial closed loop transfer function in (7.7) assuming that a stable feedback controller is already implemented for the first feedback loop. For the second control loop  $\gamma_{b_2}(j\omega)$  is first determined and then a controller  $k_2(j\omega)$  is implemented in terms of this  $\gamma_{b_2}(j\omega)$  transfer function as (7.25). The closed loop stability and controller stability conditions for the second control loop are satisfied by appropriate selection and interpolation of  $\gamma_{b_2}(j\omega)$  which is related to the closed loop transfer function as (7.20). Now if the first feedback loop breaks, then closed loop stability of the second local feedback loop is determined by the stability of the term  $\gamma_{b_1}(j\omega)$ , which is the design parameter for the second feedback loop had the first feedback loop not been implemented, given as

$$\gamma_{b_1}(j\omega)W_{b_1}(j\omega)B_{b_1}(j\omega) = \frac{-g_{bb}(j\omega)k_2(j\omega)}{1 + g_{bb}(j\omega)k_2(j\omega)} \quad (7.26)$$

Substituting  $k_2(j\omega)$  from (7.25) in (7.26) gives

$$\begin{aligned} & \gamma_{b_1}(j\omega)W_{b_1}(j\omega)B_{b_1}(j\omega) \\ &= \frac{-g_{bb}(j\omega) \frac{-\gamma_{b_2}(j\omega)W_{b_2}(j\omega)}{[1 + \gamma_{b_2}(j\omega)W_{b_2}(j\omega)B_{b_2}(j\omega)] \hat{h}_{bb}(j\omega)}}{1 + g_{bb}(j\omega) \frac{-\gamma_{b_2}(j\omega)W_{b_2}(j\omega)}{(1 + \gamma_{b_2}(j\omega)W_{b_2}(j\omega)B_{b_2}(j\omega)) \hat{h}_{bb}(j\omega)}}} \end{aligned} \quad (7.27)$$

After simplification, (7.27) can be written as

$$\gamma_{b_1}(j\omega)W_{b_1}(j\omega)B_{b_1}(j\omega) = \frac{\gamma_{b_2}(j\omega)W_{b_2}(j\omega)B_{b_2}(j\omega)\frac{g_{bb}(j\omega)}{h_{bb}(j\omega)}}{1 + \gamma_{b_2}(j\omega)W_{b_2}(j\omega)B_{b_2}(j\omega)\left[1 - \frac{g_{bb}(j\omega)}{h_{bb}(j\omega)}\right]} \quad (7.28)$$

The second control loop will be robust to a failure of the first control loop if  $\gamma_{b_2}(j\omega)$  is determined such that the denominator of (7.28) given by the term

$$1 + \gamma_{b_2}(j\omega)W_{b_2}(j\omega)B_{b_2}(j\omega)\left[1 - \frac{g_{bb}(j\omega)}{h_{bb}(j\omega)}\right] \quad (7.29)$$

does not have any RHP zeros. This is satisfied if the nyquist contour of

$$\gamma_{b_2}(j\omega)W_{b_2}(j\omega)B_{b_2}(j\omega)\left[1 - \frac{g_{bb}(j\omega)}{h_{bb}(j\omega)}\right] \quad (7.30)$$

does not enclose the  $(-1+j0)$  point. It should be noted that for a stable controller  $\gamma_{b_2}(j\omega)$  is determined such that the nyquist contour of  $\gamma_{b_2}(j\omega)W_{b_2}(j\omega)B_{b_2}(j\omega)$  does not enclose the critical point. The maximum peak magnitude of this term across all frequencies can be denoted as

$$\|\gamma_{b_2}(j\omega)W_{b_2}(j\omega)B_{b_2}(j\omega)\|_{\infty} = \|\gamma_{b_2}(j\omega)\|_{\infty} = M_{b_2} \quad (7.31)$$

As per the small gain theorem, the nyquist contour of  $\gamma_{b_2}(j\omega)W_{b_2}(j\omega)B_{b_2}(j\omega)\left[1 - \frac{g_{bb}(j\omega)}{h_{bb}(j\omega)}\right]$  will not enclose the critical point if

$$\left\|\gamma_{b_2}(j\omega)W_{b_2}(j\omega)B_{b_2}(j\omega)\left[1 - \frac{g_{bb}(j\omega)}{h_{bb}(j\omega)}\right]\right\|_{\infty} \leq 1 \quad (7.32)$$

Substituting from (7.31) in (7.32) gives

$$M_{b_2}\left\|\left[1 - \frac{g_{bb}(j\omega)}{h_{bb}(j\omega)}\right]\right\|_{\infty} \leq 1 \quad (7.33)$$

Dividing both sides of inequality by  $M_{b_2}$

$$\left\| \left[ 1 - \frac{g_{bb}(j\omega)}{h_{bb}(j\omega)} \right] \right\|_{\infty} \leq \frac{1}{M_{b_2}} \quad (7.34)$$

It can be seen from (7.34) that if the maximum peak magnitude of the term in the brackets in (7.30), i.e.

$$\left[ 1 - \frac{g_{bb}(j\omega)}{h_{bb}(j\omega)} \right] \quad (7.35)$$

is less than or equal to  $M_{b_2}^{-1}$  at all frequencies then (7.29) does not have any RHP zeros and the second loop will be stable. A less conservative statement would be to ensure that frequencies at which (7.35) has low gain and low phase margins,  $\gamma_{b_2}(j\omega)W_{b_2}(j\omega)B_{b_2}(j\omega)$  has large gain and large phase margins. Substituting  $h_{bb}(j\omega)$  from (7.10) in (7.35) gives

$$1 - \frac{g_{bb}(j\omega)}{h_{bb}(j\omega)} = 1 - \frac{1}{1 + \gamma_{a_1}(j\omega)W_{a_1}(j\omega)B_{a_1}(j\omega) \frac{g_{ba}(j\omega)g_{ab}(j\omega)}{g_{aa}(j\omega)g_{bb}(j\omega)}}} \quad (7.36)$$

also simplified as

$$1 - \frac{g_{bb}(j\omega)}{h_{bb}(j\omega)} = \left[ 1 + \frac{g_{aa}(j\omega)g_{bb}(j\omega)}{\gamma_{a_1}(j\omega)W_{a_1}(j\omega)B_{a_1}(j\omega)g_{ba}(j\omega)g_{ab}(j\omega)} \right]^{-1} \quad (7.37)$$

Substituting (7.37) in (7.34) gives

$$\left\| \left[ 1 + \frac{g_{aa}(j\omega)g_{bb}(j\omega)}{\gamma_{a_1}(j\omega)W_{a_1}(j\omega)B_{a_1}(j\omega)g_{ba}(j\omega)g_{ab}(j\omega)} \right]^{-1} \right\|_{\infty} \leq \frac{1}{M_{b_2}}$$

or alternatively as

$$\left| \left[ 1 + \frac{g_{aa}(j\omega)g_{bb}(j\omega)}{\gamma_{a_1}(j\omega)W_{a_1}(j\omega)B_{a_1}(j\omega)g_{ba}(j\omega)g_{ab}(j\omega)} \right]^{-1} \right| \leq \frac{1}{M_{b_2}} \quad \forall \omega$$

As both sides of inequality are positive, inversion leads to

$$\left| 1 + \frac{g_{aa}(j\omega)g_{bb}(j\omega)}{\gamma_{a_1}(j\omega)W_{a_1}(j\omega)B_{a_1}(j\omega)g_{ba}(j\omega)g_{ab}(j\omega)} \right| \geq M_{b_2} \quad \forall \omega$$

which can also be rearranged as

$$\left| \gamma_{a_1}(j\omega) + \frac{g_{aa}(j\omega)g_{bb}(j\omega)}{W_{a_1}(j\omega)B_{a_1}(j\omega)g_{ba}(j\omega)g_{ab}(j\omega)} \right| \geq M_{b_2} |\gamma_{a_1}(j\omega)| \quad \forall \omega \quad (7.38)$$

**Proposition 1.** For any value of  $M_{b_2}$  such that  $M_{b_2} \neq 1$ , (7.38) for a discrete frequency  $\omega_i$  is the equation of an Apollonius circle in the  $\gamma_{a_1}$ -plane which gives the locus of all points whose distances from  $\frac{-g_{aa}(j\omega_i)g_{bb}(j\omega_i)}{W_{a_1}(j\omega_i)B_{a_1}(j\omega_i)g_{ba}(j\omega_i)g_{ab}(j\omega_i)}$  to 0 are in the ratio  $M_{b_2}$ . The centre  $c$  and radius  $r$  of this circle are given as

$$c = \left( \frac{1}{1 - M_{b_2}^2} \right) \left[ \frac{-g_{aa}(j\omega_i)g_{bb}(j\omega_i)}{W_{a_1}(j\omega_i)B_{a_1}(j\omega_i)g_{ba}(j\omega_i)g_{ab}(j\omega_i)} \right]$$

$$r = \frac{M_{b_2}}{(M_{b_2}^2 - 1)} \left| \frac{g_{aa}(j\omega_i)g_{bb}(j\omega_i)}{W_{a_1}(j\omega_i)B_{a_1}(j\omega_i)g_{ba}(j\omega_i)g_{ab}(j\omega_i)} \right|$$

*Proof.* See Appendix A □

The equation (7.38) can also be stated as (7.39) which describes the region inside a circle for a discrete frequency  $\omega_i$

$$\left| \gamma_{a_1}(j\omega_i) + \left( \frac{1}{1 - M_{b_2}^2} \right) \frac{g_{aa}(j\omega_i)g_{bb}(j\omega_i)}{W_{a_1}(j\omega_i)B_{a_1}(j\omega_i)g_{ab}(j\omega_i)g_{ba}(j\omega_i)} \right| \leq \frac{M_{b_2}}{(M_{b_2}^2 - 1)} \left| \frac{g_{aa}(j\omega_i)g_{bb}(j\omega_i)}{W_{a_1}(j\omega_i)B_{a_1}(j\omega_i)g_{ab}(j\omega_i)g_{ba}(j\omega_i)} \right| \quad (7.39)$$

The condition for robustness to failure of individual loops can be deduced for different values of  $M_{b_2}$  from this equation which represents different regions in the design

freedom plane. For simplicity, let the term

$$A(j\omega) = \frac{g_{aa}(j\omega)g_{bb}(j\omega)}{W_{a_1}(j\omega)B_{a_1}(j\omega)g_{ba}(j\omega)g_{ab}(j\omega)} \quad (7.40)$$

From (7.7),

$$q_{e_2} = h_{bb}(j\omega)f_{c_2}(j\omega) + h_{bc}(j\omega)f_p(j\omega)$$

The partial closed loop transfer function  $h_{bb}(j\omega)$  is related to the open loop transfer function  $g_{bb}(j\omega)$  as

$$\frac{h_{bb}(j\omega)}{g_{bb}(j\omega)} = 1 + \gamma_{a_1}(j\omega)W_{a_1}(j\omega)B_{a_1}(j\omega)\frac{g_{ab}(j\omega)g_{ba}(j\omega)}{g_{aa}(j\omega)g_{bb}(j\omega)}$$

The region inside a circle centred on  $A(j\omega_i)$  corresponds to a reduction in magnitude of FRF

$$\left| \frac{h_{bb}(j\omega_i)}{g_{bb}(j\omega_i)} \right| < 1$$

$A(j\omega)$  at any arbitrary discrete frequency  $\omega_i$  is the centre of the circle that corresponds to attenuation in output at the second control loop error sensor resulting from control action in the first feedback loop for any primary excitation collocated with this error sensor. The robustness to failure for different values of  $M_{b_2}$  is depicted in the  $\gamma_{a_1}$ -plane as follows

**Case 1:** The special case when  $M_{b_2} = 1$  results in a perpendicular bisector of the line segment joining the point  $A(j\omega_i)$  with the origin. Substituting  $M_{b_2} = 1$  in (7.38) yields

$$\left| \gamma_{a_1}(j\omega) + \frac{g_{aa}(j\omega)g_{bb}(j\omega)}{W_{a_1}(j\omega)B_{a_1}(j\omega)g_{ba}(j\omega)g_{ab}(j\omega)} \right| \geq |\gamma_{a_1}(j\omega)| \quad \forall \omega \quad (7.41)$$

For a discrete frequency  $\omega_i$  substituting in terms of  $A(j\omega_i)$  from (7.40) gives

$$|\gamma_{a_1}(j\omega_i) + A(j\omega_i)| \geq |\gamma_{a_1}(j\omega_i)| \quad (7.42)$$

which is the equation of a perpendicular bisector of the line joining the points 0 and  $A(j\omega_i)$  in the  $\gamma_{a_1}$ -plane. The condition to guarantee integrity of the decentralised multivariable control system is that the controller  $k_1(j\omega)$  is implemented

using values for  $\gamma_{a_1}$  selected from only one half of the  $\gamma_{a_1}$ -plane divided by this line segment. This is the portion of the plane which encompasses the origin as shown in figure 7.1. The red dashed circle in the  $\gamma_{a_1}$ -plane represents reduction in output at the second error sensor for any excitation that occurs at the same point.

**Case 2:** Substituting (7.40) in (7.39) gives

$$\left| \gamma_{a_1}(j\omega_i) + \left( \frac{1}{1 - M_{b_2}^2} \right) A(j\omega_i) \right| \leq \frac{M_{b_2}}{M_{b_2}^2 - 1} |A(j\omega_i)| \quad (7.43)$$

If  $M_{b_2} > 1$ , then the circle (7.43) surrounds the origin and  $A(j\omega_i)$  lies outside this circle. For increasing values of  $M_{b_2}$ , the centre of this circle approaches 0, and the size of the circle becomes smaller as seen in figure 7.2. For robust stability of both control loops, a value for  $\gamma_{a_1}$  will have to be selected at this frequency from a region that lies inside this circle. The position and size of this region depends on the terms  $A(j\omega_i)$  and  $M_{b_2}$ , but for very large values of  $M_{b_2}$  the size of this region reduces. Therefore, as the peak magnitude of  $\gamma_{b_2}(j\omega)$  increases, the region in the  $\gamma_{a_1}$ -plane available for controller implementation reduces and this imposes an additional constraint on the implementation of the controller for first loop. Predictably, selection of  $\gamma_{a_1}$  from inside these circles for increasing values of  $M_{b_2}$  results in very low controller gain at these frequencies.

The peak magnitude  $M_{b_2}$  gives the worst case condition for selection of  $\gamma_{a_1}$  such that the second control loop is robust to failure of the first control loop. A less conservative approach would be to use the actual magnitude of  $\gamma_{b_2}(j\omega)$  instead of its peak magnitude to determine the feasible regions in the  $\gamma_{a_1}$ -plane for robust stability. This would allow selection of  $\gamma_{a_1}$  from a larger region as compared to the more conservative approach.

**Remark** The robust stability condition to ensure stability of feedback loop 2 when feedback loop 1 fails can be summarized from the foregoing treatment in the  $\gamma_{a_1}$ -plane. It can be stated as follows:

*The effect of feedback control at loop 1 should not cause attenuation of the open loop response between the output at error sensor 2 and the excitation input at the point*

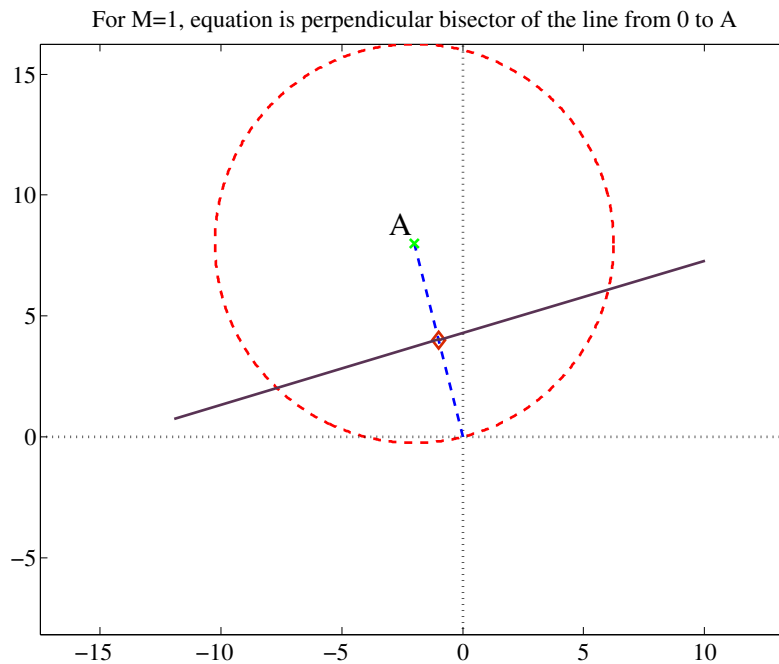


Figure 7.1: The perpendicular bisector in  $\gamma_{a_1}$ -plane for  $M_{b_2} = 1$

*of application of second loop control force.*

This would ensure that when loop 1 fails then the ‘closed’ loop response to point excitation at the second control loop does not get amplified thereby ensuring closed loop stability.

## 7.3 Summary

A sequential loop closing control design technique has been demonstrated using the geometric design approach. The robustness to failure of inner feedback loops can be formulated in terms of the design parameter. The conditions that guarantee integrity of additional loops is described in the design freedom plane. It predicts robustness of the second feedback loop to failure of the first loop if the control action due to the first loop does not attenuate the driving point transfer function of the second. This can be defined in terms of additional constraints on the selection and interpolation of the design parameter transfer function.

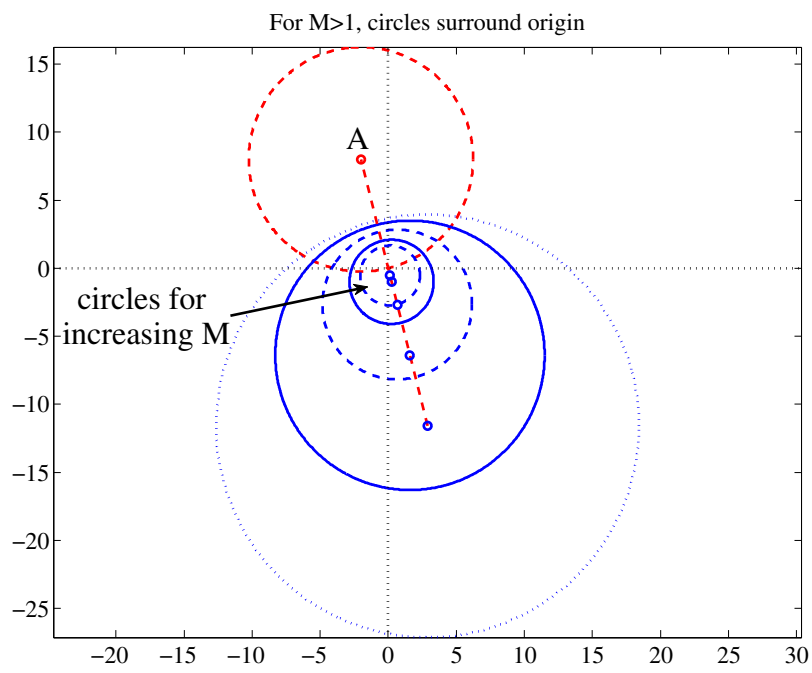


Figure 7.2: Circles for increasing value of  $M_{b_2}$  in  $\gamma_{a_1}$ -plane

# Chapter 8

## Experimental Verification of Sequential Loop Closing Control Design

### 8.1 Introduction

The decentralised multivariable control design for remote vibration attenuation presented in chapter 7 is experimentally validated in this chapter<sup>1</sup>. The full-scale laboratory set-up is a simply supported in situ cast post-tensioned slab strip that is representative of many floor structures used in building construction. A schematic of the concrete slab is shown in figure 8.1. The total length of the slab strip is 11.2 m which includes 200 mm overhangs over each edge support. It is 2.0 m wide, 275 mm thick and weighs approximately 15 tonnes. The first mode of vibration has a natural frequency around 4.4 Hz, the second bending mode occurs around 16.7 Hz while the third mode is a torsional mode which occurs around 26.2 Hz. These low frequency resonant modes are prone to excitation by human-induced motion.

This slab structure is used for the study of vibration mitigation in floor structures due to excitations characterised by human body motions such as walking, running, skipping, jumping, etc. Vibration due to human induced excitation is problematic in office floors, footbridges, stadia and other large buildings [Bachmann and Ammann, 1987]. The development of newer materials which are stronger but lighter has allowed the possibility

---

<sup>1</sup>This work was carried out at the Department of Civil and Structural Engineering, University of Sheffield, during July-August 2012

of constructing open plan structures inexpensively and with ease. The use of lighter materials has unfortunately led to lesser damping and lower natural frequencies of the floors which can be easily excited by periodic human motions or operation of indoor equipment. Although this is not a safety concern, vibration mitigation is an ongoing area of research amongst the civil and structural engineering community due to the vibration serviceability requirements. Traditionally, passive techniques have been employed to this end but lately AVC technologies have gained acceptance in this field [Nyawako and Reynolds, 2009, 2011].

However, a major area of concern is the dynamics and nonlinearities of the actuators that are typically used on civil engineering structures, which adversely affects the AVC system performance and stability margins. Ideally, the actuator dynamics should not influence the open loop system dynamics but in practice this would still be acceptable if the resonance due to the inertial mass of the actuator is considerably less than the structural resonance [Benassi et al., 2004; Elliott et al., 2001]. The actuators used in this study are four electrodynamic inertial shakers as shown in figure 8.2, two of which are APS Electro-Seis Dynamics Model 113 used for primary excitation, and larger APS Electro-Seis Dynamics Model 400 used as control actuators. The FRF between the output of the control shaker, which is the force applied by the inertial mass, and the input voltage that drives the shaker is shown in figure 8.4. The acceleration of the inertial mass is measured using Endevco accelerometers mounted on the armature of the shaker as shown in figure 8.3. A low frequency resonance is evident which will affect the performance of the control system at the first structural resonant frequency. The vertical acceleration is measured using QA accelerometers (shown in figure 8.3) mounted at certain test points of interest on the structure.

## 8.2 Experimental Implementation

### 8.2.1 Selection of suitable measurement and performance test points

The first bending mode of the slab can be excited by a suitable force applied near its mid-span. This is achieved using a primary excitation shaker at test point 11 (TP11),  $f_{p_2}$  in figure 8.1. The second bending and torsional modes are excited using a disturbance shaker placed at TP02, denoted as  $f_{p_1}$  in figure 8.1. The first feedback loop

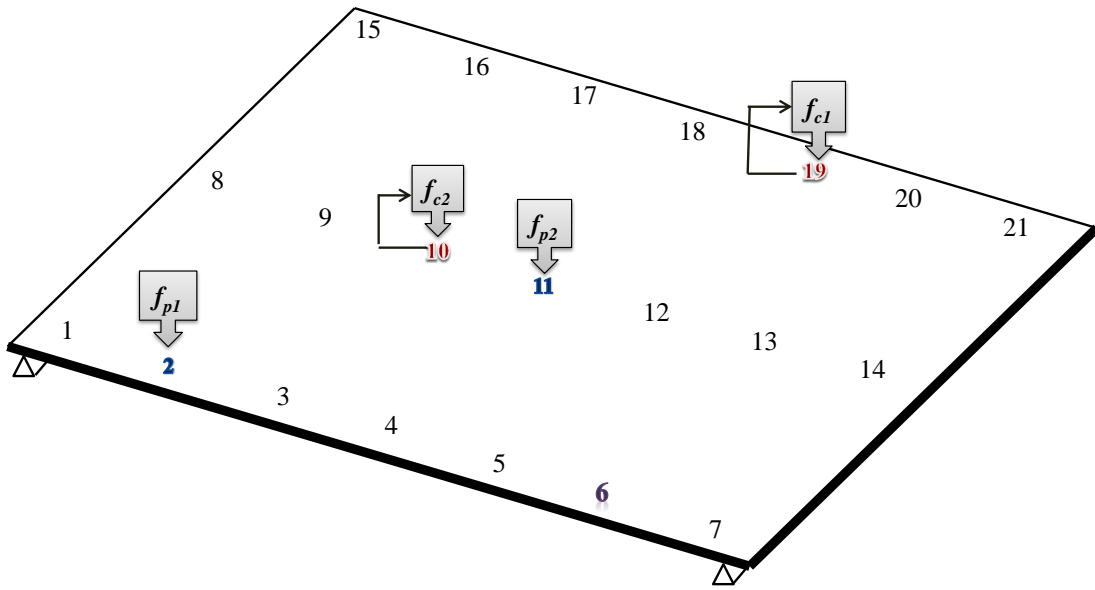


Figure 8.1: Schematic of the concrete slab showing location of excitation shakers ( $f_{p1}$  and  $f_{p2}$ ) and control shakers ( $f_{c1}$  and  $f_{c2}$ ) on the structure, acceleration is also measured at test point 6 (TP06) for remote performance evaluation

is designed for a control shaker at TP19 as it can attenuate the torsional mode effectively from this location. A suitable location for the second control shaker is chosen as TP10 because it can affect the first and second bending mode of the slab appropriately. An additional remote point at TP06 is chosen for performance evaluation of a remote vibration controller since all the three modes are readily visible at this location. The magnitude of FRF between acceleration measurement at all test points of interest to the excitation input signal for both disturbance shakers at TP02 and TP11 upto 100 Hz is shown in figure 8.5 and figure 8.6, respectively. This was obtained by feeding uncorrelated random excitation to both the disturbance shakers and taking measurements of the QA accelerometers. A transfer function model approximation for both the local control path FRFs has non-minimum phase characteristics.

### 8.2.2 Control Design for first feedback loop at TP19

A controller is designed for the shaker at TP19 for attenuation around the torsional mode frequency of the structure. A weighting filter,  $W_{a1}(j\omega)$ , has to be selected for



Figure 8.2: View of the laboratory set-up from one end

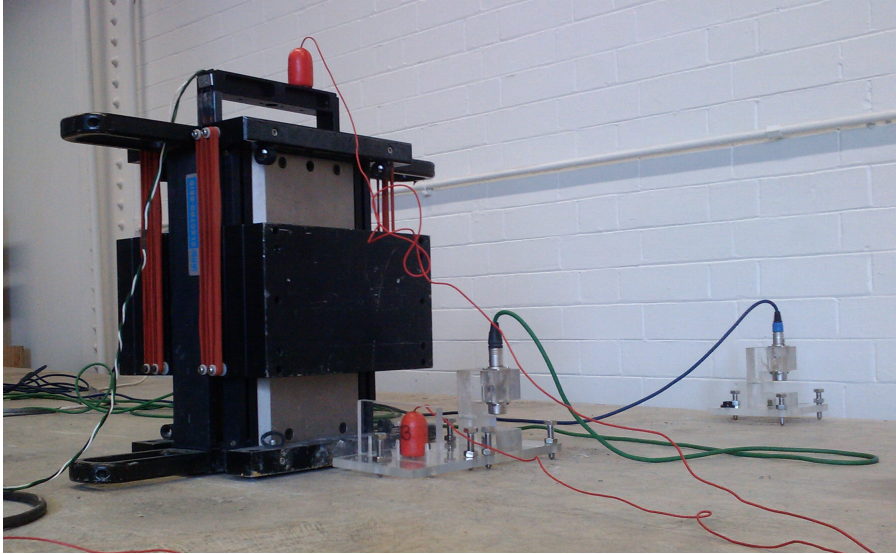


Figure 8.3: Control Shaker, piezo-electric Endevco accelerometer used to capture shaker dynamics, and QA accelerometer used for feedback measurement

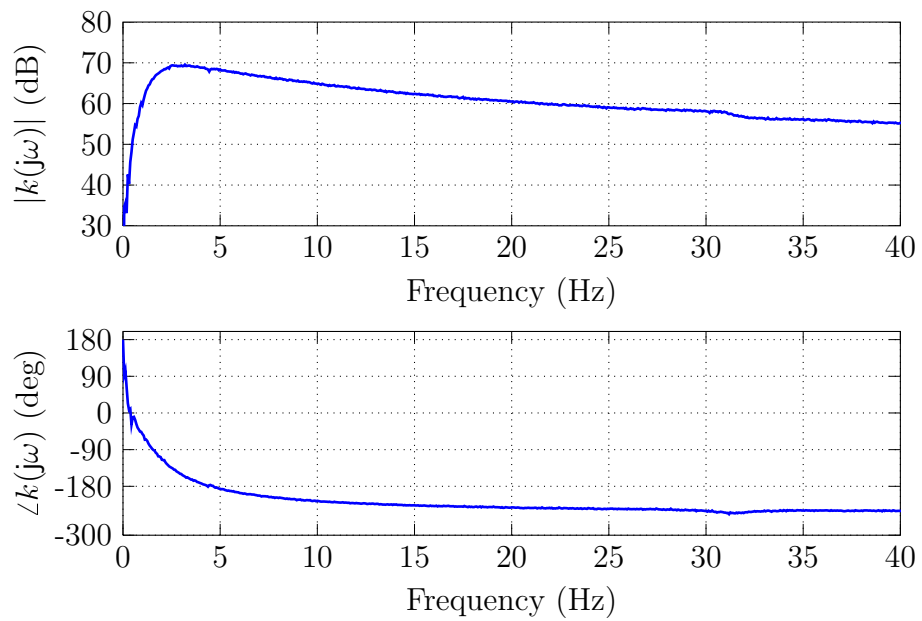


Figure 8.4: Magnitude and Phase of the actuator dynamics

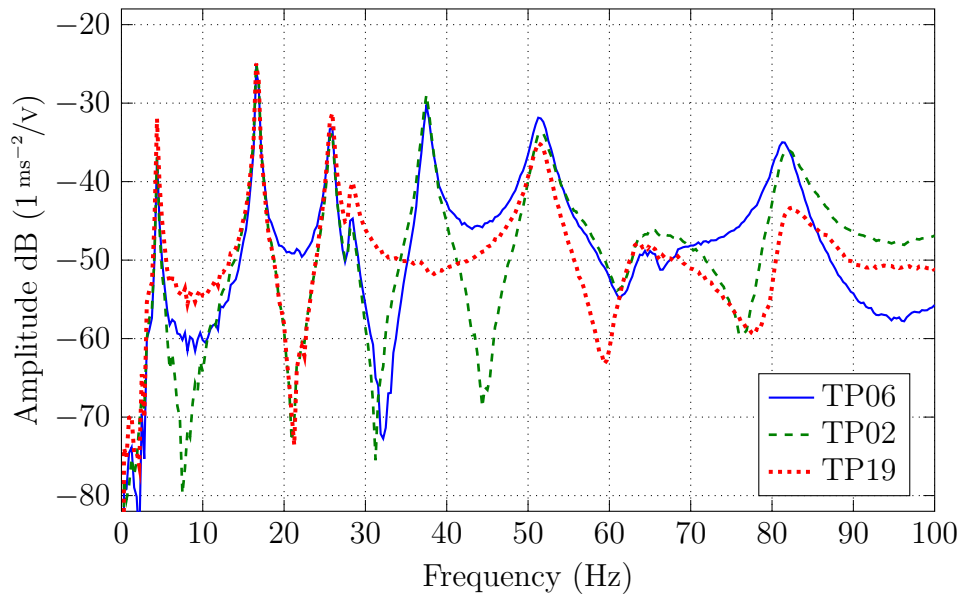


Figure 8.5: Magnitude of the FRF between the acceleration output at TP06, TP02, TP19 and the primary excitation at TP02

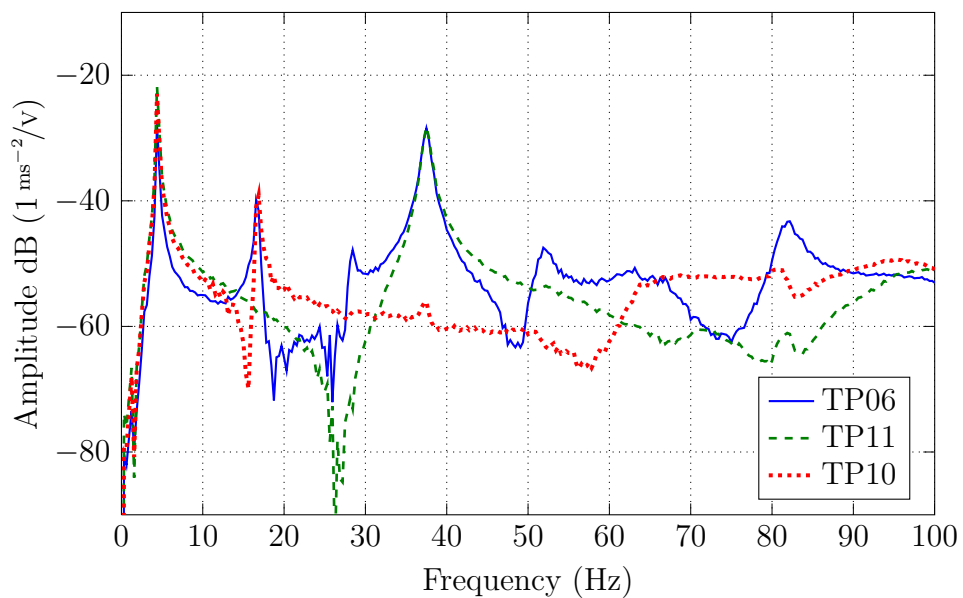


Figure 8.6: Magnitude of the FRF between the acceleration output at TP06, TP11, TP10 and the primary excitation at TP11

suppression of spillover at problematic frequencies. It is chosen as an 8th order band-pass butterworth filter with low cut-off frequency 19.9 Hz and high cut-off frequency 39.4 Hz. The regions describing attenuation at various test points of interest is then determined in the design freedom plane. The circles enclosing the regions describing attenuation at TP19, TP02 and TP06 for discrete frequencies between 25.5 Hz to 27 Hz is shown in figure 8.7. It can be seen that the regions almost completely overlap which indicates that spatially global reduction is possible in this frequency band. The optimal values for the design parameter is selected near the centre of these circles at discrete frequencies. This set of optimal values for design parameter is then interpolated at the design frequencies using the Nevanlinna Pick interpolation algorithm as was previously demonstrated for the beam example in section 3.5. A controller is then realised in terms of this design parameter transfer function which is then used to compute the theoretical reduction in output at the desired locations. The magnitude of the FRF between output at TP19, TP02 and TP06 and disturbance input at TP02 predicts reduction around the frequency of interest using this designed feedback controller as shown in figures 8.8, 8.9 and 8.10. The weighting filter used with this design parameter ensures that the controller for the first loop does not have energy in the same frequency band as the controller for the second feedback loop. The system dynamics of this partially closed loop system is then utilised in the design of a feedback control system at TP10. The actual FRF measurements of the open loop system as shown in figures 8.5 and 8.6 is used for the computation of partial closed loop system dynamics.

### 8.2.3 Control Design for second feedback loop at TP10

The partial closed loop system dynamics with the first control loop closed is used for estimating a local control path model of the second loop. The design of the control system for the second loop does not necessitate identification of a model for the other FRFs and so the inaccuracies due to model approximation can be avoided compared to a centralised MIMO control design.

The control shaker for the second feedback loop at TP10 targets reduction around the first and second natural frequency of the structure. Therefore, the test points of interest for this control design are TP11, TP10 and TP06; the last one is chosen to evaluate the performance of the remote vibration controller. A suitable weighting filter to

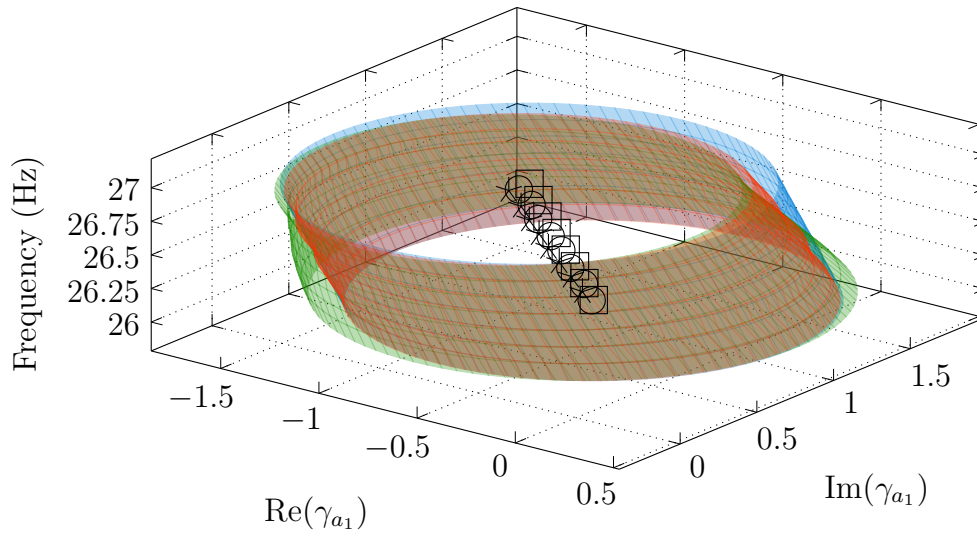


Figure 8.7: Regions in  $\gamma_a$ -plane in the design frequency band describing the reduction in output at TP06 (centre of circle ○), TP02 (centre of circle ★) and TP19 (centre of circle □)

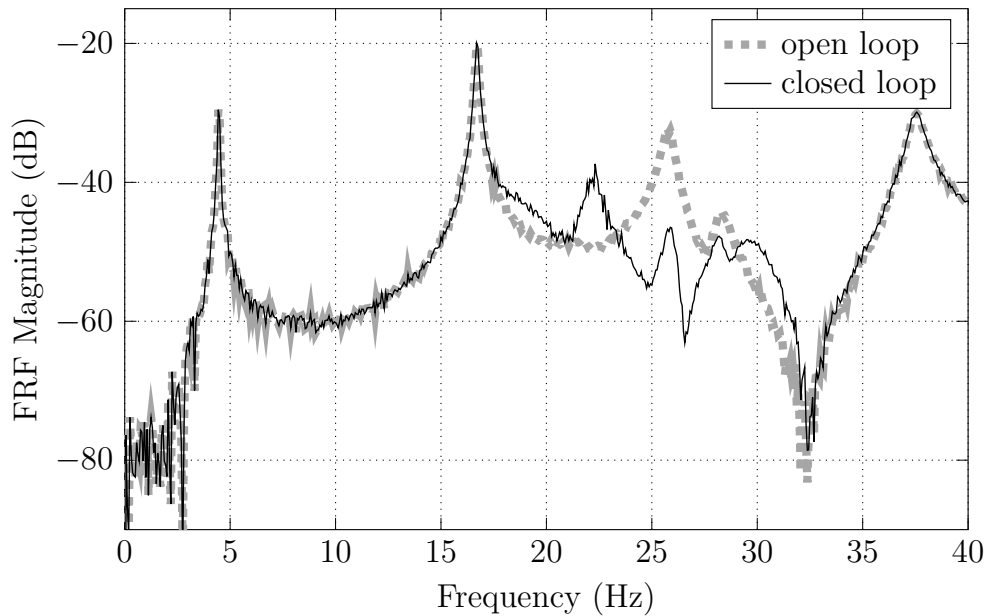


Figure 8.8: Comparison of the predicted magnitude of FRF between output at TP06 and disturbance excitation at TP02, with and without (dashed) feedback control at TP19

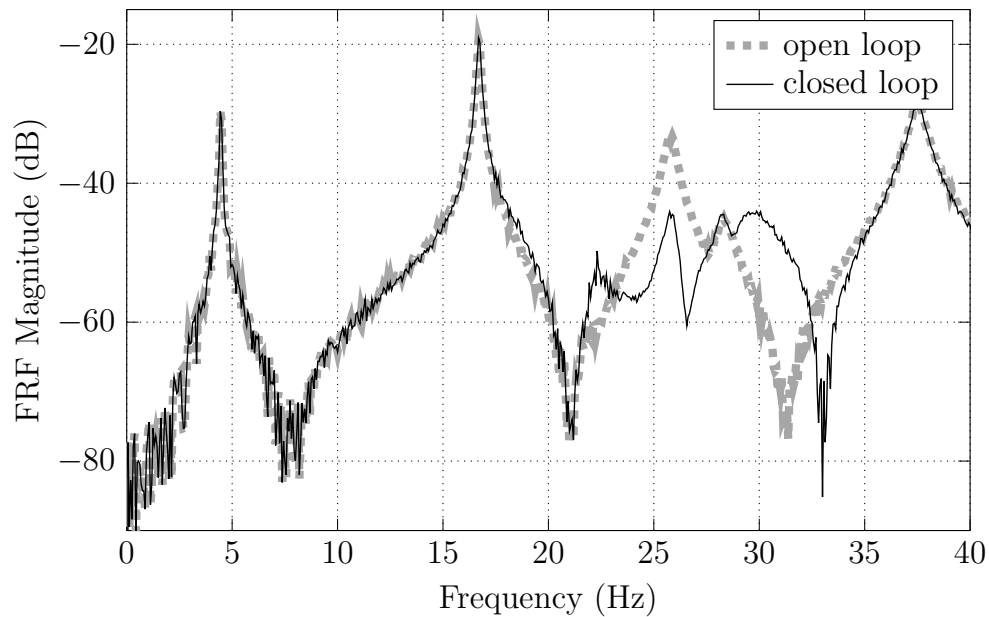


Figure 8.9: Comparison of the predicted magnitude of FRF between output at TP02 and disturbance excitation at TP02, with and without (dashed) feedback control at TP19

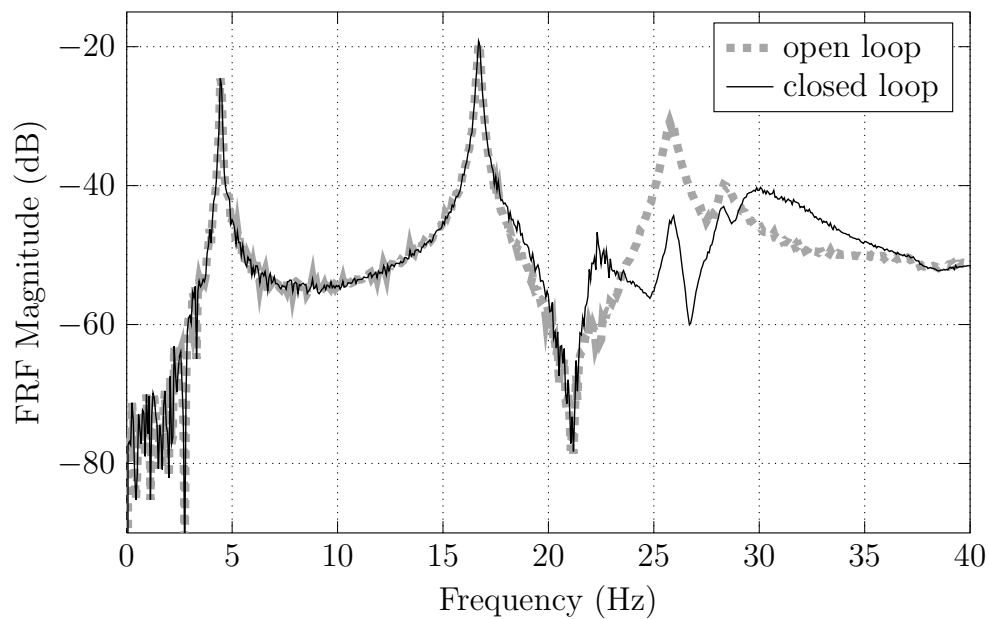


Figure 8.10: Comparison of the predicted magnitude of FRF between output at TP19 and disturbance excitation at TP02, with and without (dashed) feedback control at TP19

suppress excitation due to spillover at undesired frequencies is initially selected. Significant energy in the control input below 2.0 Hz will cause instabilities due to the shaker dynamics as illustrated in figure 8.4. Therefore, an 8th order bandpass butterworth filter, with low and high cut-off frequencies of 2.0 Hz and 25.7 Hz respectively, is selected.

The design freedom parameter for the second loop,  $\gamma_{b_2}$ , is selected based on the partial closed loop transfer function at this location. The regions in  $\gamma_{b_2}$ –plane for reduction in vibration at TP06, TP10 and TP11 for frequencies near the first resonant frequency in figure 8.11 almost overlap indicating the possibility of spatially global reduction for this bending mode. However, for frequencies near the second resonance the centre of circles representing attenuation at TP11 denoted as  $\square$  lie outside the circles that represent attenuation at TP06 and TP10 as seen in figure 8.12. This is because for the second bending mode, there is a node at the location of TP11. So, further attenuation at TP11 near the second resonant frequency is not a concern but it should be ensured that the output does not deteriorate at TP11. Therefore the optimal values for design freedom is selected as the centre of the circle representing attenuation at TP10 as this would lie inside the regions representing attenuation at the other test points of interest. It is interpolated using the Nevanlinna Pick interpolation algorithm and a controller is implemented in terms of the design parameter transfer function. The maximum singular value of  $\gamma_{b_2}(j\omega)$  is less than 1 which simplifies robustness to failure of the first feedback loop as shown by Eq.(7.32).

The closed loop stability of the feedback loop depends on the stability of the design parameter transfer function as given in Eq.(7.20). Now if the first loop fails then the stability of the second feedback loop, with the designed controller in operation, depends on the stability of the term given by Eq.(7.26). As is shown in section 7.2.3, this condition can be satisfied if the nyquist contour of Eq.(7.30) does not enclose the critical point. The nyquist diagram of this term for the identified design parameter transfer function obtained using NP interpolation is plotted in figure 8.13. The contour does not enclose the critical point which signifies robustness of this controller to failure of the first feedback loop.

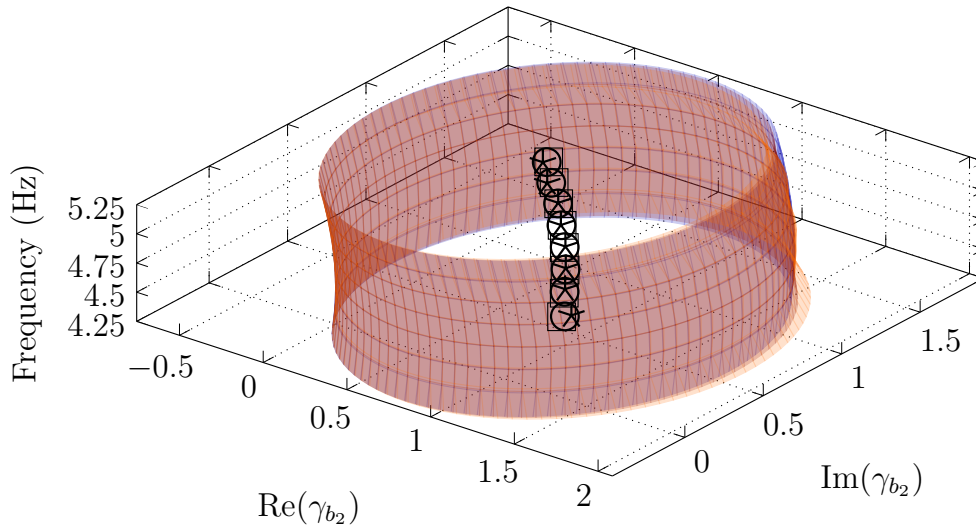


Figure 8.11: Regions in  $\gamma_{b_2}$ -plane in the frequency band near first natural frequency describing the reduction in output at TP06 (centre ☆), TP11 (centre ○) and TP10 (centre □)

### 8.2.4 Experimental Results

The controllers developed in section 8.2.2 and section 8.2.3 for the first and second feedback loop has to be implemented in the laboratory through Simulink using an dSPACE real time interface hardware. Prior to that it is converted to a discrete-time function using the first order hold method with a sampling frequency of 2 kHz. The FRF of the discretised compensator matches accurately with the continuous time domain compensator especially in the design frequency bandwidth.

Random excitation is fed to both the disturbance shakers at TP02 and TP11 which is driven by the power amplifiers in voltage control mode. The control shakers at TP19 and TP10 are also operated in voltage control mode. The power spectral density of the QA accelerometer measurements at the relevant test points are plotted in figures 8.14, 8.15, 8.16, 8.17 and 8.18 for three different runs of experiments. In the first run of experiment, control at TP10 is switched off and only control shaker at TP19 is operational. It can be seen from the plots that when the control is switched on at TP19 only, there is a reduction of approximately 10 dB in the response levels at TP06, TP02 and TP19 around the torsional mode frequency. In the second run of experiments control at TP19 is switched off and only control shaker at TP10 is operational. It can be seen

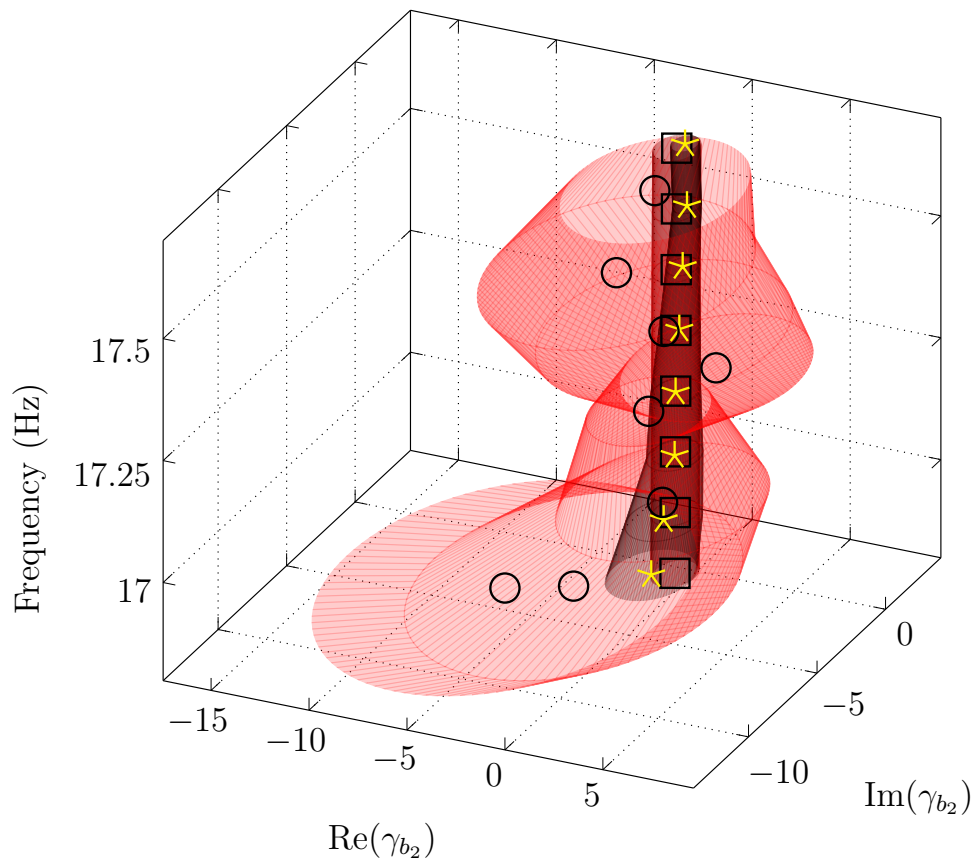


Figure 8.12: Regions in  $\gamma_{b_2}$ -plane in the frequency band near second natural frequency describing the reduction in output at TP06 (centre ★), TP11 (centre ○) and TP10 (centre □)

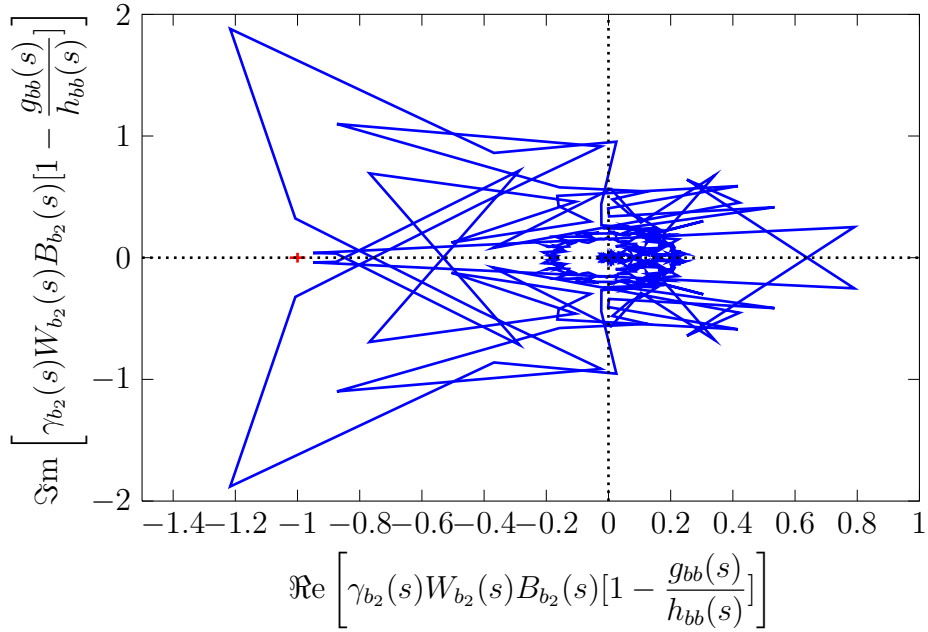


Figure 8.13: Nyquist plot of the term (7.30) which determines robustness of second loop when inner loop fails

from the plots of PSD that the response levels at TP06, TP02, TP19 and TP10 reduces by around 15 dB near the frequency of the second bending mode. There is also a reduction of more than 10 dB in response levels at all the test points around the frequency of the first bending mode which shows the predicted attenuation in the design frequency band is achieved. In the third run of experiments, control shaker at TP19 is switched on followed by the control shaker at TP10. The closed loop system remains stable for this configuration even when one of the controllers is switched off. This demonstrates the robustness of both control loops to the failure of individual loops. The PSD of the outputs at all the test points for both controllers switched on shows more than 10 dB reduction close to the frequencies of the first bending mode and torsional mode whereas the response levels reduce by around 15 dB near the frequency of the second bending mode.

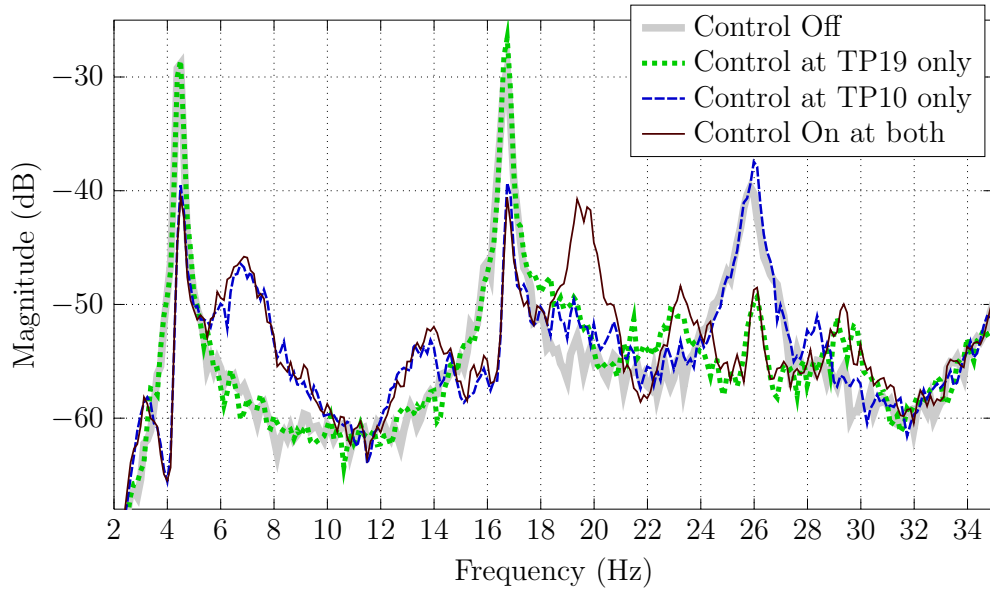


Figure 8.14: Power spectral density of the output at TP06, open loop (thick shaded), partial closed loop with control action at only TP19 (dotted) and only TP10 (dashed), and both loops closed (thin solid)

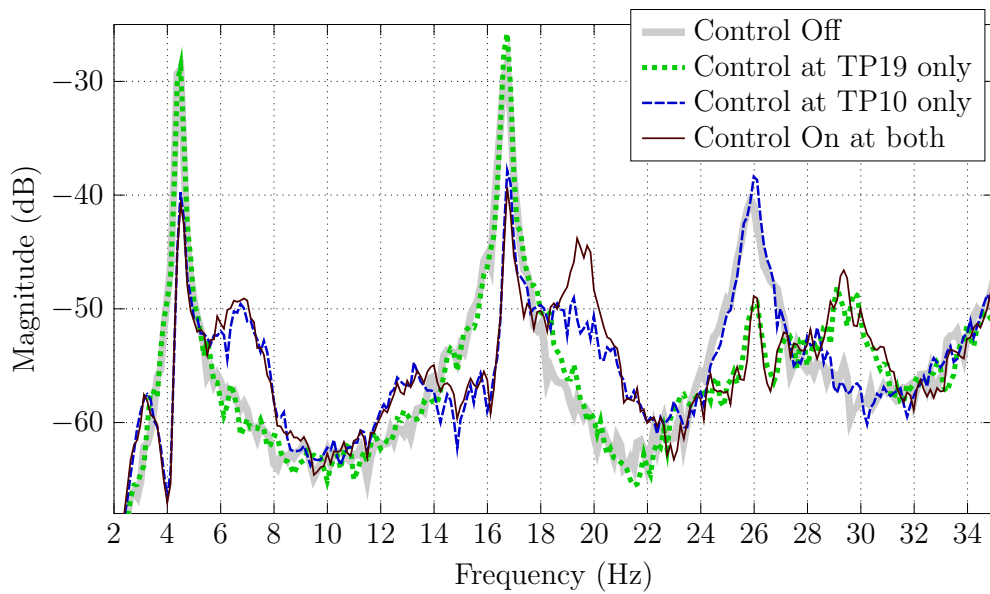


Figure 8.15: Power spectral density of the output at TP02, open loop (dotted), partial closed loop with control action at only TP19 (dash-dotted) and only TP10 (dashed), and both loops closed (solid)

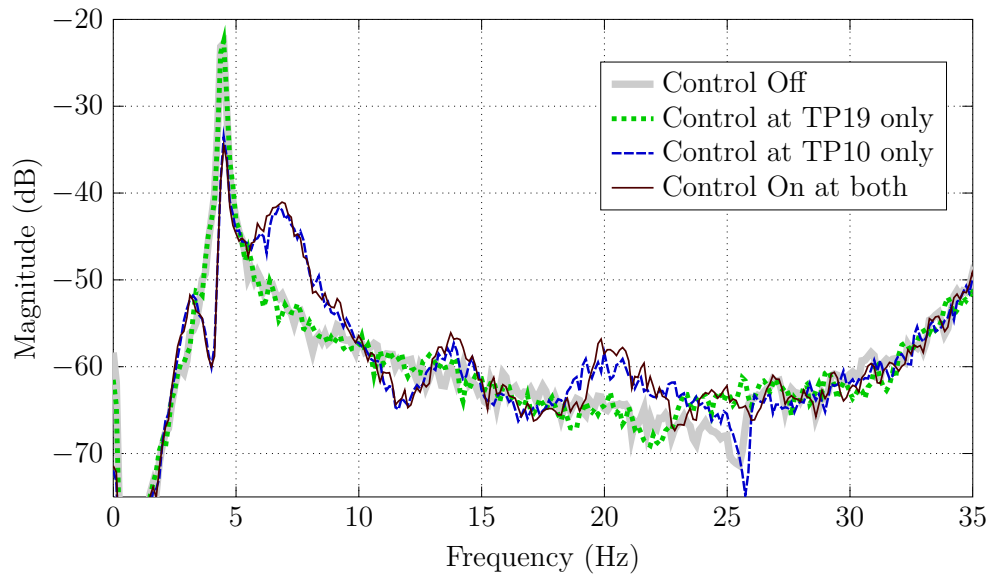


Figure 8.16: Power spectral density of the output at TP11, open loop (dotted), partial closed loop with control action at only TP19 (dash-dotted) and only TP10 (dashed), and both loops closed (solid)

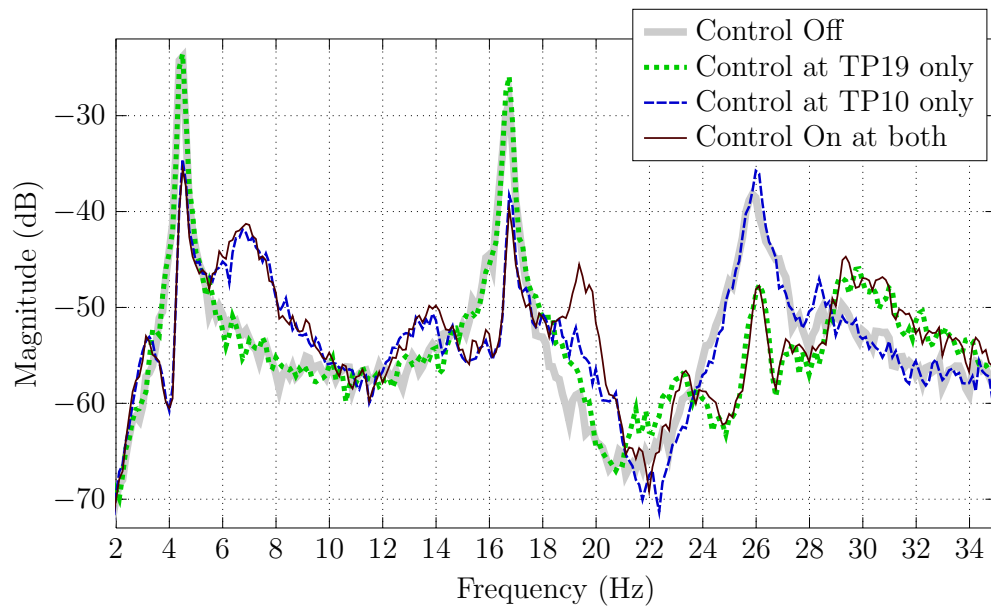


Figure 8.17: Power spectral density of the output at TP19, open loop (dotted), partial closed loop with control action at only TP19 (dash-dotted) and only TP10 (dashed), and both loops closed (solid)

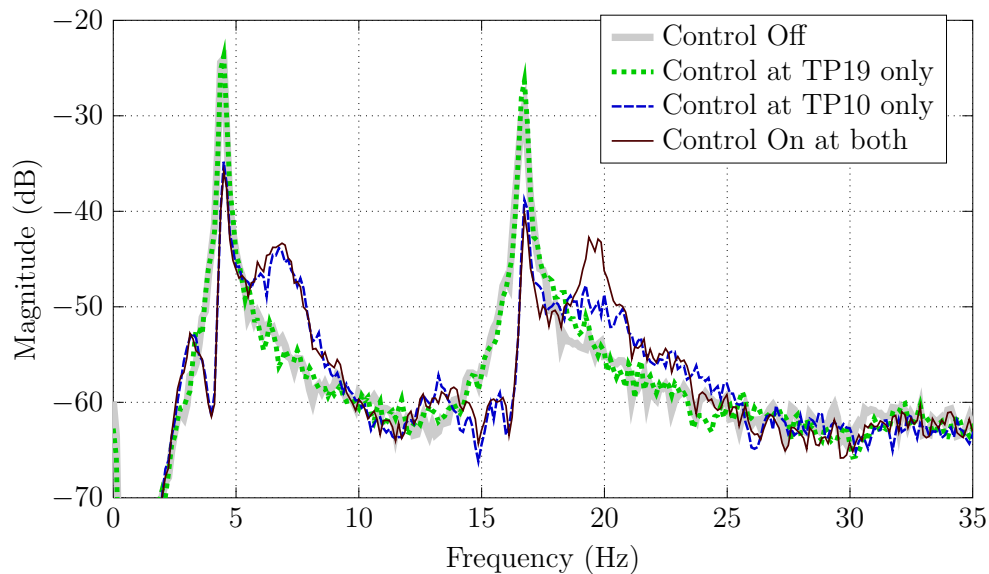


Figure 8.18: Power spectral density of the output at TP10, open loop (dotted), partial closed loop with control action at only TP19 (dash-dotted) and only TP10 (dashed), and both loops closed (solid)

### 8.3 Summary

The geometric-based decentralised multivariable feedback controller design approach has been experimentally validated using a laboratory set-up. The first control loop at a test point on a floor slab structure is used to attenuate vibration output at frequencies close to the torsional mode. The second control loop at a different test point attenuates vibration output close to the first and second bending mode frequencies. The interaction between both control loops can cause instabilities in the system. This is addressed with the help of the design parameter, so that both control loops are robust to the failure of each other. The results demonstrate the validity of the aforementioned method for the design of two feedback loops that can be operated individually or concurrently for remote vibration attenuation.

# Chapter 9

## Conclusions

A remote vibration control design technique for the attenuation of broadband disturbance at more than one location, subject to achievability, is detailed in this thesis. This is motivated from the practical problems associated with sensor and actuator dynamics for remote vibration attenuation and the undesirable consequences of locally optimal control actions. For example, in marine vessels and rotor aircraft, the excitation generated due to propulsion systems gets transmitted to other vibration sensitive regions. The attenuation of this vibration at easily accessible locations may then lead to an enhanced response at other locations.

The developed methodology provides the control designer with a systematic procedure to evaluate and then generate an optimal controller based on the required performance. The restrictions on the controller stability in the previously related works, when the local control path transfer function is non-minimum phase, is solved in the work presented here. According to this method, a single design variable allows the parameterisation of feasible attenuation at the local and remote points. A single sensor and actuator pair can then be used to achieve desired vibration mitigation performance at the local and remote points. The value of this design activity lies in the uncomplicated rendering of the achievable attenuation at the remote and local points and then exploiting this information to realise a suitable strongly stabilising controller.

Robustness to uncertainties and unmodelled dynamics is also tackled within the framework of this geometric approach. The available design freedom shapes the controller FRF to suppress the excitation of dynamics at out of band frequencies. The circles in the  $\gamma$ -plane can also be visualised in a three dimensional plot. The contour

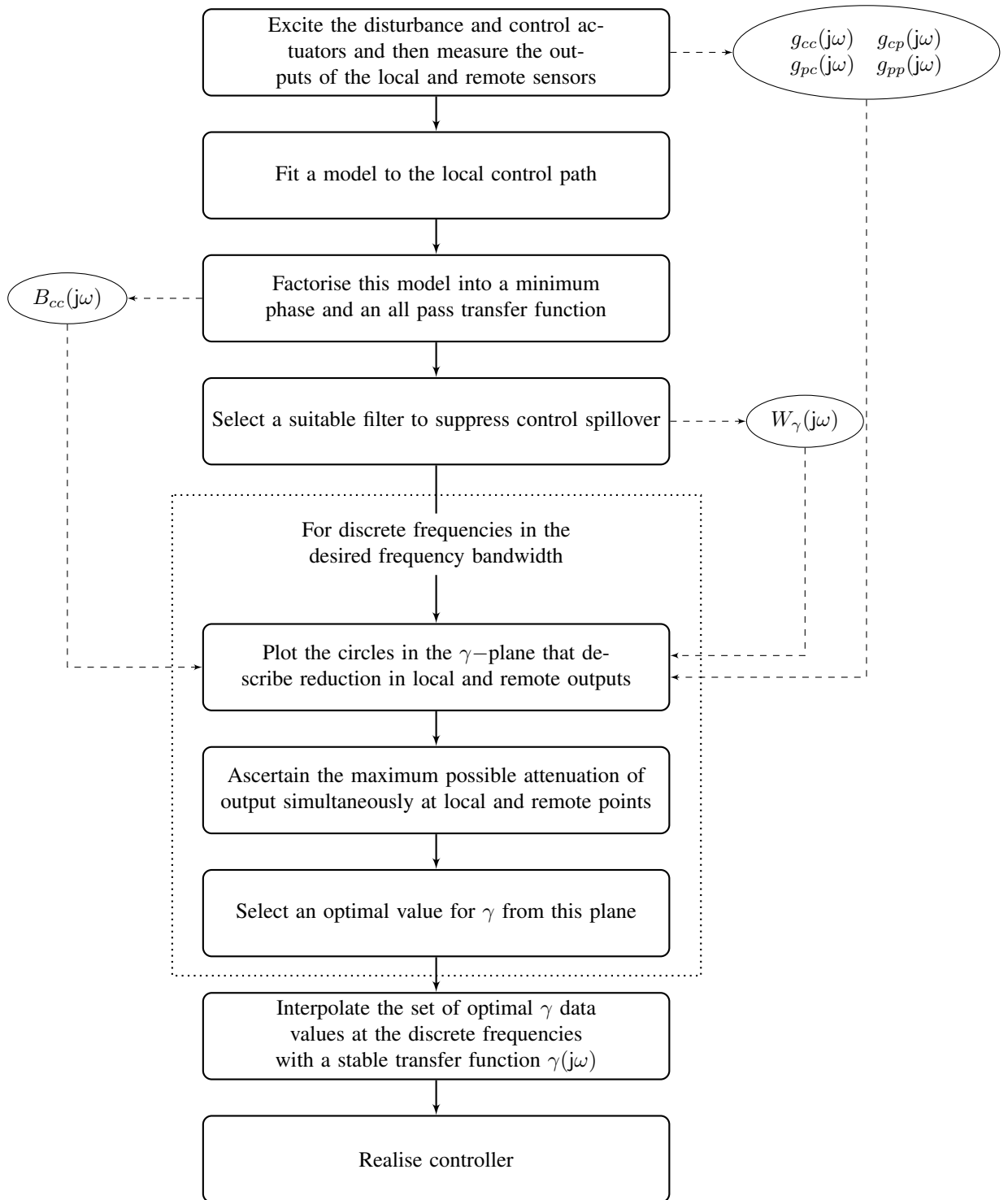


Figure 9.1: Flow chart showing the main steps of the geometric based control design

---

of the final operating values of the design parameter, which is obtained from the FRF of the identified design parameter transfer function, allows for a simplistic interpretation of the controller performance in a certain frequency band. The main steps of the control design are summarised in figure 9.1.

The proposed control design was also experimentally validated using a propeller blade test rig. The sharp peaks in the controller FRF due to the inversion of lightly damped zeros in the minimum phase counterpart of the local path transfer function is also addressed using a notch filter. Alternatively, this peak can be suppressed by selecting small values for the design parameter from near the origin in the complex plane.

The effect of local control on the response level at remote points for frequencies close to resonance can also be proven with the help of this design parameter. It shows that active damping of the local control path FRF using control on the resonating structure achieves satisfactory global response. This result is extended for the reduction of kinetic energy of a beam model and compared with the ideal performance using a direct velocity feedback control.

Finally, an extension for the design of a multivariable controller using the geometric technique is also presented. A sequential loop closing approach is used for the design of de-centralised multiple feedback controllers. Due to the interactions between the individual loops it is important to consider the stability of each loop to the failure of other loops. Robustness to failure of individual loops is also demonstrated with the help of an experimental implementation.

## 9.1 Contributions

The main achievements of the work presented in this thesis are briefly summarised below:

1. A systematic procedure is developed in chapter 3 for the design of a stable and broadband controller based on the previous geometric approach. This method relaxes the requirement for a truly collocated sensor and actuator pair.
2. The conditions for avoiding control spillover can be incorporated in this design

procedure itself, so that the final compensator is robust to the uncertainties of unmodelled system dynamics. This allows the practical implementation of controller for the broadband mitigation of vibration.

3. This control system design is experimentally validated for a laboratory rig, that replicates the vibration problem in propeller blade systems, in chapter 4. It is demonstrated that due to the nature of vibration excitation and transmission in this system, it is not feasible to achieve reasonable remote vibration attenuation.
4. In chapter 5, it is proven analytically in terms of this design parameter that optimal control at the local point results in good global response for frequencies near resonance.
5. A control system design is proposed for kinetic energy reduction based on its optimal values for frequencies near resonance and antiresonance. This can potentially be used to overcome the limitations of direct velocity feedback control for kinetic energy reduction.
6. In chapter 7, a decentralised sequential loop closing technique for the design of multivariable controllers is also presented. This method provides conditions on the design parameter that ensures the robustness of individual loops to the failure of other feedback loops.
7. The multivariable control design is experimentally validated on a laboratory scale slab structure. It provides good vibration reduction performance and the design of individual feedback loops is made robust to the failure of other loop using this method.

## 9.2 Scope for further work

The geometric approach in its present form is a very convenient tool for the evaluation of any remote vibration controller performance. It can be used to extract meaningful information regarding the feasibility of simultaneous attenuation at the local and remote points. This functionality is demonstrated in figure 4.4, which clearly shows the limited

influence of any control action on the remote output. However, the calculation of a suitable controller from the optimal design parameter using the procedure in its current form results in many shortcomings. This can cause significant performance degradation depending on the dynamics of the system. Some of the drawbacks and recommendations to improve this design methodology is presented below:

### 9.2.1 Lower Order Compensator

The main drawback is the high order of the final controller LTI model. The optimal set of values for the design parameter at the discrete frequencies is interpolated using the Nevanlinna Pick interpolation algorithm. The order of the final controller using this method increases by four for every additional data value. One way to reduce the order of the controller is to minimise the size of the optimal design parameter data set. This can be achieved for lightly damped structures by selecting only very few optimal values close to the resonant frequencies, since the region of overlap is maximum at these frequencies and the feasible data values would tolerate considerable deviation from the optimal data values. But for heavily damped structures, the region of overlap depicting feasible attenuation at several locations decreases in the design freedom plane, thus necessitating interpolation at many discrete frequencies. Furthermore, the gradient of  $\kappa$ , defined in Eq.(3.38), for the optimal values of the design parameter can be large for some control problems, as shown in figure 4.5. Therefore in this case, it requires more interpolation data values in the frequencies from 220 to 250 Hz to obtain simultaneous attenuation at the local and remote points. The filter,  $W_\gamma(j\omega)$ , also affects the selection of optimal values for the design parameter which is explained in section 3.5.3.1, based on its effect on the gradient of  $\kappa$ . The requirement for filters with a high order or with cut-off frequencies close to the design frequency bandwidth increases the gradient of  $\kappa$ , thus necessitating more interpolation data values.

### 9.2.2 Computational complexity

Also, the processing power required for NP interpolation increases as the number of data values increase. This computational complexity can be determined by the number of arithmetic operations for the calculation of the Fenyves array, as given in (3.36), and

the recursive evaluation of a function, as given in (3.37). The calculation of Fenyves array requires  $O(n^2)$  operations and the subsequent computation of the function requires  $O(n)$  steps. Therefore, it is recommended that an algorithm be developed such that the discrete frequencies for which the values of the design parameter are considered for interpolation is optimised. Based on this, a reduced set of discrete frequencies can be determined such that any redundant data values are avoided. Furthermore, order reduction techniques can be employed that results in a lower order controller with the same performance in the desired bandwidth, however this may require extra computation power. This computational requirement and the need to realise a high order controller also hampers the attenuation of a larger frequency bandwidth.

### **9.2.3 Interpolation of design parameter**

The main steps in the interpolation of the optimal values of the design parameter is shown in figure 9.2. This procedure is applicable for many of the commonly occurring vibration control problems and the whole process can be automated. However, it still requires judicious user input to satisfy the controller stability conditions by manually tuning the  $\sigma$  and  $M$  values. The criteria for determination of sensible values for  $\sigma$  and  $M$  is illustrated with the help of an example in section 3.5.3. It may not always be possible to follow the guidelines listed therein due to the nature of the contour formed by the optimal values of the design parameter. A large value of  $M$  will increase the positive definiteness of the Pick matrix given by Eq.(3.35), which determines the closed loop stability. However, for controller stability, the term given by

$$\frac{1}{1 + \gamma(j\omega)B_{cc}(j\omega)W_{\gamma}(j\omega)}$$

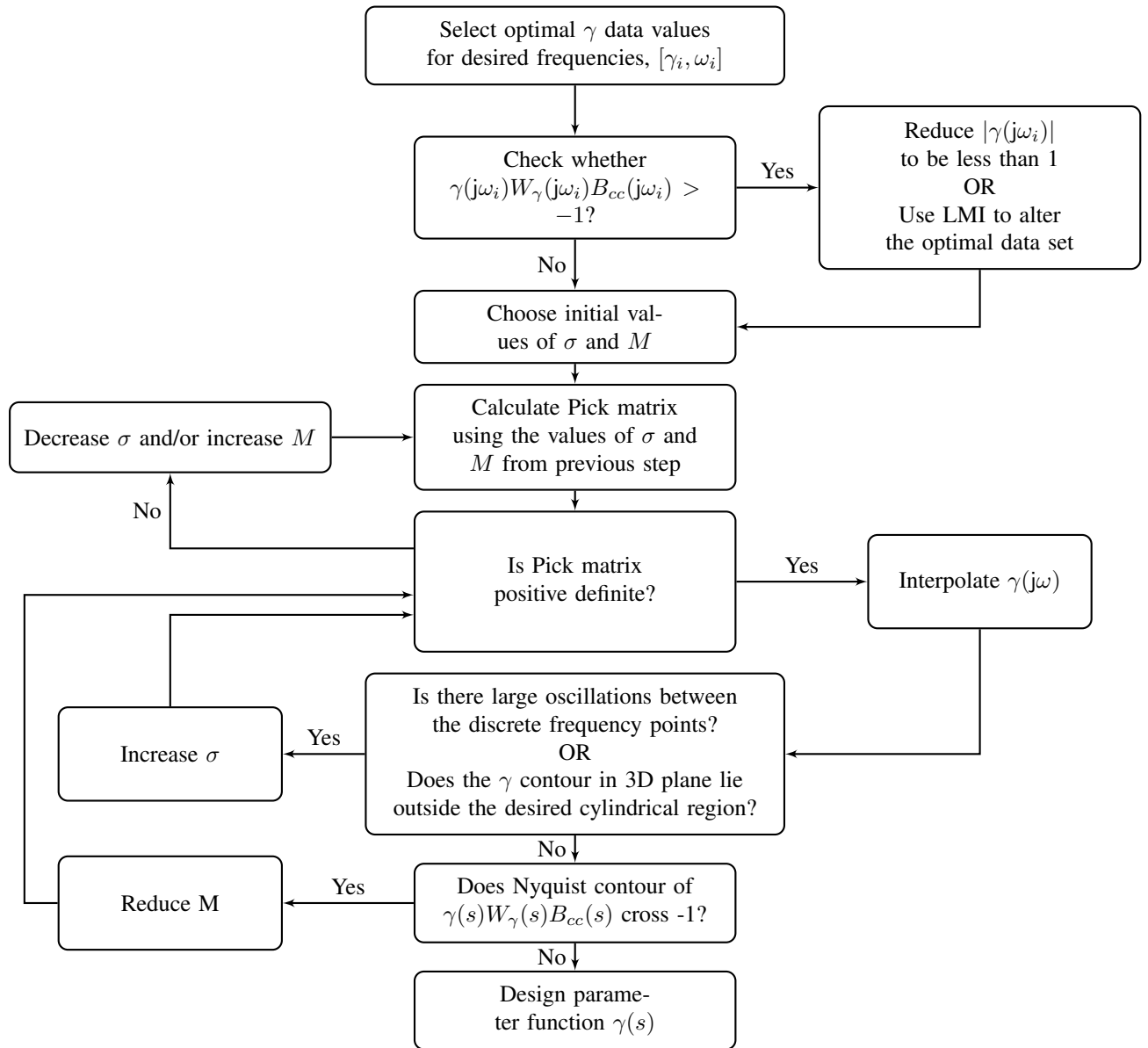


Figure 9.2: Flow chart showing the steps of the Nevanlinna Pick interpolation

should also be stable. A Pick matrix  $P_s$  for this term can be defined based on the selections of  $M$  and  $\sigma$  as

$$P_s = \left[ \begin{array}{c} 1 - \frac{1}{\left(1 + \frac{\gamma_k}{M} B_{cc}(j\omega_k) W_\gamma(j\omega_k)\right) \left(1 + \frac{\bar{\gamma}_l}{M} \bar{B}_{cc}(j\omega_l) \bar{W}_\gamma(j\omega_l)\right)} \\ \frac{1}{\sigma + j\omega_k + (\sigma - j\omega_l)} \end{array} \right]_{k,l=1}^n \quad (9.1)$$

Multiplying the terms inside the brackets and substituting  $B_{cc}(j\omega_k) \bar{B}_{cc}(j\omega_l) W_\gamma(j\omega_k) \bar{W}_\gamma(j\omega_l) = 1$  gives

$$P_s = \left[ \begin{array}{c} 1 - \frac{1}{1 + \frac{\gamma_k}{M} B_{cc}(j\omega_k) W_\gamma(j\omega_k) + \frac{\bar{\gamma}_l}{M} \bar{B}_{cc}(j\omega_l) \bar{W}_\gamma(j\omega_l) + \frac{\gamma_k \bar{\gamma}_l}{M^2}} \\ \frac{1}{j(\omega_k - \omega_l) + 2\sigma} \end{array} \right]_{k,l=1}^n \quad (9.2)$$

It can be seen from Eq.(9.2) that the positive definiteness of  $P_s$  reduces as  $M$  increases which proves the difficulty in obtaining a stable controller if a small value of  $M$  also does not ensure closed loop stability. Therefore, in some cases the optimal values of  $\gamma$  needs to be manually adjusted so that the closed loop stability is satisfied for a small value of  $M$ .

# Appendix A

A generalized form of (7.38) is written as

$$|z - A| \geq c |z - B|$$

Squaring both sides

$$(z - A)(\bar{z} - \bar{A}) \geq c^2(z - B)(\bar{z} - \bar{B})$$

$$z\bar{z} - c^2z\bar{z} - z\bar{A} + c^2z\bar{B} - \bar{z}A + c^2\bar{z}B \geq c^2B\bar{B} - A\bar{A}$$

$$[1 - c^2]z\bar{z} + [c^2\bar{B} - \bar{A}]z + [c^2B - A]\bar{z} \geq c^2B\bar{B} - A\bar{A}$$

$$[c^2 - 1]z\bar{z} - [c^2\bar{B} - \bar{A}]z - [c^2B - A]\bar{z} \leq A\bar{A} - c^2B\bar{B}$$

$$z\bar{z} - \frac{[c^2\bar{B} - \bar{A}]}{[c^2 - 1]}z - \frac{[c^2B - A]}{[c^2 - 1]}\bar{z} \leq \frac{A\bar{A} - c^2B\bar{B}}{[c^2 - 1]}$$

$$z\bar{z} - \frac{[c^2\bar{B} - \bar{A}]}{[c^2 - 1]}z - \frac{[c^2B - A]}{[c^2 - 1]}\bar{z} + \frac{|c^2B - A|^2}{[c^2 - 1]^2} \leq \frac{A\bar{A} - c^2B\bar{B}}{[c^2 - 1]} + \frac{|c^2B - A|^2}{[c^2 - 1]^2}$$

---


$$\left| z - \left( \frac{c^2 B - A}{c^2 - 1} \right) \right|^2 \leq \frac{[A\bar{A} - c^2 B\bar{B}] [c^2 - 1] + (c^2 B - A) (c^2 \bar{B} - \bar{A})}{[c^2 - 1]^2}$$

$$\left| z - \left( \frac{A - c^2 B}{1 - c^2} \right) \right|^2 \leq \frac{c^2 A\bar{A} - A\bar{A} - c^4 B\bar{B} + c^2 B\bar{B} + c^4 B\bar{B} - c^2 \bar{A}B - c^2 A\bar{B} + A\bar{A}}{[c^2 - 1]^2}$$

$$\left| z - \left( \frac{c^2 B - A}{c^2 - 1} \right) \right|^2 \leq \frac{c^2 |B - A|^2}{[1 - c^2]^2}$$

$$\left| z - \left( \frac{c^2 B - A}{c^2 - 1} \right) \right| \leq \frac{c |B - A|}{[c^2 - 1]}$$

Substituting

$$z = \gamma_{a_1}$$

$$A = \frac{-g_{aa}(j\omega)g_{bb}(j\omega)}{B_{a_1}(j\omega)g_{ab}(j\omega)g_{ba}(j\omega)}$$

$$c = M_{b_2}, \quad B = 0$$

gives

$$\left| \gamma_{a_1}(j\omega) + \left( \frac{1}{1 - M_{b_2}^2} \right) \frac{g_{aa}(j\omega)g_{bb}(j\omega)}{B_{a_1}(j\omega)g_{ab}(j\omega)g_{ba}(j\omega)} \right| \leq \frac{M_{b_2}}{(M_{b_2}^2 - 1)} \left| \frac{g_{aa}(j\omega)g_{bb}(j\omega)}{B_{a_1}(j\omega)g_{ab}(j\omega)g_{ba}(j\omega)} \right|$$

## Appendix B

The mass matrix of the finite element model of the beam in section 3.5 is

$$\mathbf{M}_{\text{beam}} = 10^{-3} \times \begin{bmatrix} 0.03 & \mathbf{M}_1 & 0_{1 \times 2} & 0_{1 \times 1} \\ \mathbf{M}'_1 & \mathbf{M}_2 & \mathbf{M}_3 & 0_{2 \times 2} & 0_{2 \times 1} \\ 0_{2 \times 1} & \mathbf{M}'_3 & \mathbf{M}_2 & \mathbf{M}_3 & 0_{2 \times 2} & 0_{2 \times 1} \\ 0_{2 \times 1} & 0_{2 \times 2} & \mathbf{M}'_3 & \mathbf{M}_2 & \mathbf{M}_3 & 0_{2 \times 2} & 0_{2 \times 1} \\ 0_{2 \times 1} & 0_{2 \times 2} & 0_{2 \times 2} & \mathbf{M}'_3 & \mathbf{M}_2 & \mathbf{M}_3 & 0_{2 \times 2} & 0_{2 \times 2} & 0_{2 \times 2} & 0_{2 \times 2} & 0_{2 \times 1} \\ 0_{2 \times 1} & 0_{2 \times 2} & 0_{2 \times 2} & 0_{2 \times 2} & \mathbf{M}'_3 & \mathbf{M}_2 & \mathbf{M}_3 & 0_{2 \times 2} & 0_{2 \times 2} & 0_{2 \times 2} & 0_{2 \times 1} \\ 0_{2 \times 1} & 0_{2 \times 2} & 0_{2 \times 2} & 0_{2 \times 2} & 0_{2 \times 2} & \mathbf{M}'_3 & \mathbf{M}_2 & \mathbf{M}_3 & 0_{2 \times 2} & 0_{2 \times 2} & 0_{2 \times 1} \\ 0_{2 \times 1} & 0_{2 \times 2} & \mathbf{M}'_3 & \mathbf{M}_2 & \mathbf{M}_3 & 0_{2 \times 2} & 0_{2 \times 1} \\ 0_{2 \times 1} & 0_{2 \times 2} & \mathbf{M}'_3 & \mathbf{M}_2 & \mathbf{M}_3 & 0_{2 \times 1} \\ 0_{2 \times 1} & 0_{2 \times 2} & \mathbf{M}'_3 & \mathbf{M}_2 & \mathbf{M}'_4 \\ 0_{1 \times 1} & 0_{1 \times 2} & \mathbf{M}_4 & 0.03 \end{bmatrix}$$

where

$$\mathbf{M}_1 = \begin{bmatrix} 1.0 & -0.02 \end{bmatrix}$$

$$\mathbf{M}_2 = \begin{bmatrix} 233.3 & 0 \\ 0 & 0.1 \end{bmatrix}$$

$$\mathbf{M}_3 = \begin{bmatrix} 40.4 & -1 \\ 1.0 & -0.02 \end{bmatrix}$$

---


$$\mathbf{M}_4 = \begin{bmatrix} -1.0 & -0.02 \end{bmatrix}$$

and  $0_{p \times q}$  is an  $p$  rows and  $q$  columns matrix of zeros.

The stiffness matrix is

$$\mathbf{K}_{\text{beam}} = 10^{-2} \times \begin{bmatrix} 1.12 & \mathbf{K}_1 & 0_{1 \times 2} & 0_{1 \times 1} \\ \mathbf{K}'_1 & \mathbf{K}_2 & \mathbf{K}_3 & 0_{2 \times 2} & 0_{2 \times 1} \\ 0_{2 \times 1} & \mathbf{K}'_3 & \mathbf{K}_2 & \mathbf{K}_3 & 0_{2 \times 2} & 0_{2 \times 1} \\ 0_{2 \times 1} & 0_{2 \times 2} & \mathbf{K}'_3 & \mathbf{K}_2 & \mathbf{K}_3 & 0_{2 \times 2} & 0_{2 \times 1} \\ 0_{2 \times 1} & 0_{2 \times 2} & 0_{2 \times 2} & \mathbf{K}'_3 & \mathbf{K}_2 & \mathbf{K}_3 & 0_{2 \times 2} & 0_{2 \times 2} & 0_{2 \times 2} & 0_{2 \times 2} & 0_{2 \times 1} \\ 0_{2 \times 1} & 0_{2 \times 2} & 0_{2 \times 2} & 0_{2 \times 2} & \mathbf{K}'_3 & \mathbf{K}_2 & \mathbf{K}_3 & 0_{2 \times 2} & 0_{2 \times 2} & 0_{2 \times 2} & 0_{2 \times 1} \\ 0_{2 \times 1} & 0_{2 \times 2} & 0_{2 \times 2} & 0_{2 \times 2} & 0_{2 \times 2} & \mathbf{K}'_3 & \mathbf{K}_2 & \mathbf{K}_3 & 0_{2 \times 2} & 0_{2 \times 2} & 0_{2 \times 1} \\ 0_{2 \times 1} & 0_{2 \times 2} & \mathbf{K}'_3 & \mathbf{K}_2 & \mathbf{K}_3 & 0_{2 \times 2} & 0_{2 \times 1} \\ 0_{2 \times 1} & 0_{2 \times 2} & \mathbf{K}'_3 & \mathbf{K}_2 & \mathbf{K}_3 & 0_{2 \times 1} \\ 0_{2 \times 1} & 0_{2 \times 2} & \mathbf{K}'_3 & \mathbf{K}_2 & \mathbf{K}'_4 \\ 0_{1 \times 1} & 0_{1 \times 2} & \mathbf{K}_4 & 1.12 \end{bmatrix}$$

where

$$\mathbf{K}_1 = \begin{bmatrix} -16.80 & 0.56 \end{bmatrix}$$

$$\mathbf{K}_2 = \begin{bmatrix} 672 & 0 \\ 0 & 2.224 \end{bmatrix}$$

$$\mathbf{K}_3 = \begin{bmatrix} -336 & 16.8 \\ -16.80 & 0.56 \end{bmatrix}$$

$$\mathbf{K}_4 = \begin{bmatrix} -16.80 & -0.56 \end{bmatrix}$$

The damping matrix is

$$\mathbf{C}_{\text{beam}} = 8 \times 10^{-2} \times \mathbf{M}_{\text{beam}} + 8 \times 10^{-6} \times \mathbf{K}_{\text{beam}}$$

# References

- R. Alkhatib and MF Golnaraghi. Active structural vibration control: a review. *Shock and Vibration Digest*, 35(5):367, 2003. 2
- DK Anthony and SJ Elliott. Comparison of the effectiveness of minimizing cost function parameters for active control of vibrational energy transmission in a lightly damped structure. *Journal of sound and vibration*, 237(2):223–244, 2000. 3
- Y. Aoki, P. Gardonio, and SJ Elliott. Modelling of a piezoceramic patch actuator for velocity feedback control. *Smart Materials and Structures*, 17:015052, 2008. 25
- H. Bachmann and W. Ammann. *Vibrations in structures: induced by man and machines*. Iabse, 1987. 116
- KH Baek and SJ Elliott. The effects of plant and disturbance uncertainties in active control systems on the placement of transducers. *Journal of sound and vibration*, 230(2):261–289, 2000. 4
- M.J. Balas. Direct velocity feedback control of large space structures. *Journal of Guidance and Control*, 2:252, 1979. 5, 24
- H. Balini, C.W. Scherer, and J. Witte. Performance enhancement for amb systems using unstable  $h_\infty$  controllers. *Control Systems Technology, IEEE Transactions on*, 19(6):1479–1492, 2011. 29
- O. Bardou, P. Gardonio, SJ Elliott, and RJ Pinnington. Active power minimization and power absorption in a plate with force and moment excitation. *Journal of sound and vibration*, 208(1):111–151, 1997. 3

- W.T. Baumann, F.S. Ho, and H.H. Robertshaw. Active structural acoustic control of broadband disturbances. *Acoustical Society of America Journal*, 92:1998–2005, 1992. 4
- L. Benassi, SJ Elliott, and P. Gardonio. Active vibration isolation using an inertial actuator with local force feedback control. *Journal of sound and vibration*, 276(1): 157–179, 2004. 117
- P. Bhattacharya, H. Suhail, and P.K. Sinha. Finite element analysis and distributed control of laminated composite shells using lqr/imsc approach. *Aerospace science and technology*, 6(4):273–281, 2002. 3
- I.U. Borchers, U. Emborg, A. Sollo, E.H. Waterman, J. Paillard, P.N. Larsen, G. Venet, P. Goeransson, and V. Martin. Advanced study for active noise control in aircraft (asanca). In *Fourth Aircraft Interior Noise Workshop*, volume 1, pages 129–141, 1992. 2
- MJ Brennan, SJ Elliott, and RJ Pinnington. Strategies for the active control of flexural vibration on a beam. *Journal of Sound and Vibration*, 186(4):657–688, 1995. 76
- J.C. Burgess. Active adaptive sound control in a duct: A computer simulation. *The Journal of the Acoustical Society of America*, 70:715, 1981. 2
- S.E. Burke, J.E. Hubbard, and J.E. Meyer. Distributed transducers and colocation. *Mechanical Systems and Signal Processing*, 7(4):349–361, 1993. 25
- JR Canavin. The control of spacecraft vibrations using multivariable output feedback. In *Proc. AIAA/AAS Conf*, pages 1–11, 1978. 24
- I. Chopra. Status of application of smart structures technology to rotorcraft systems. *Journal of the American Helicopter Society*, 45(4):228–252, 2000. 7
- C.P. Coelho, J.R. Phillips, and L.M. Silveira. Passive constrained rational approximation algorithm using nevanlinna-pick interpolation. In *Design, Automation and Test in Europe Conference and Exhibition, 2002. Proceedings*, pages 923–930. IEEE, 2002. 45
- C.E. Crede. *Vibration and shock isolation*. Wiley, 1951. 8

- 
- S. Daley. Algorithm architecture for sound and vibration control. In *Proceedings of the Institution of Measurement and Control Mini-Symposium, UKACC International Conference on Control*, volume 98, pages 1–6, 1998. 8
- S. Daley and J. Wang. A geometric approach to the design of remotely located vibration control systems. *Journal of Sound and Vibration*, 318(4-5):702–714, 2008. ISSN 0022-460X. 11, 23, 31, 57
- S. Daley and I. Zazas. A recursive least squares based control algorithm for the suppression of tonal disturbances. *Journal of Sound and Vibration*, 331(6):1270–1290, 2012. 2
- S. Daley, FA Johnson, JB Pearson, and R. Dixon. Active vibration control for marine applications. *Control Engineering Practice*, 12(4):465–474, 2004. 8, 75
- S. Daley, J. Hätönen, and DH Owens. Active vibration isolation in a smart spring mount using a repetitive control approach. *Control Engineering Practice*, 14(9):991–997, 2006. 8
- S. Daley, I. Zazas, and J. Hatonen. Harmonic control of a smart spring machinery vibration isolation system. *Proceedings of the Institution of Mechanical Engineers, Part M: Journal of Engineering for the Maritime Environment*, 222(2):109–119, 2008. ISSN 1475-0902. 8
- Steve Daley and Jiqiang Wang. A geometric approach to the design of remotely located vibration control systems. In *ACTIVE 2006, Proceedings*, 2006. 17, 20
- EP Darbyshire and CJ Kerry. A multi-processor computer architecture for active control. *Control Engineering Practice*, 5(10):1429–1434, 1997. 8
- B.N. Datta, S. Elhay, and Y.M. Ram. Orthogonality and partial pole assignment for the symmetric definite quadratic pencil. *Linear algebra and its applications*, 257:29–48, 1997. 75
- P. Delsarte, Y. Genin, and Y. Kamp. On the role of the nevanlinna–pick problem in circuit and system theory. *International Journal of Circuit Theory and Applications*, 9(2):177–187, 1981. 44

- C.G. Díaz and P. Gardonio. Feedback control laws for proof-mass electrodynamic actuators. *Smart Materials and Structures*, 16(5):1766, 2007. 4
- I.M. Díaz and P. Reynolds. Acceleration feedback control of human-induced floor vibrations. *Engineering Structures*, 32(1):163–173, 2010. 26
- J.J. Dosch, D.J. Inman, and E. Garcia. A self-sensing piezoelectric actuator for collocated control. *Journal of Intelligent Material Systems and Structures*, 3(1):166–185, 1992. 25
- P.G. Dylejko and N. J. Kessissoglou. Reduction of the radiated noise from a submarine under excitation from the propeller-shafting system using a resonance changer. In *Proceedings of the 13th International Congress on Sound and Vibration*, 2006. 8, 23
- SJ Elliot, PA Nelson, IM Stothers, and CC Boucher. In-flight experiments on the active control of propeller-induced cabin noise. *Journal of Sound and Vibration*, 140(2): 219–238, 1990. 2
- S. Elliott, I. Stothers, and P. Nelson. A multiple error lms algorithm and its application to the active control of sound and vibration. *Acoustics, Speech and Signal Processing, IEEE Transactions on*, 35(10):1423–1434, 1987. 2
- SJ Elliott. Filtered reference and filtered error lms algorithms for adaptive feedforward control. *Mechanical systems and signal processing*, 12(6):769–781, 1998. 2
- SJ Elliott. *Signal Processing for Active Control*. Academic Press, 2001. 3
- SJ Elliott, M. Serrand, and P. Gardonio. Feedback stability limits for active isolation systems with reactive and inertial actuators. *Journal of vibration and acoustics*, 123(2):250–261, 2001. 117
- S.J. Elliott, P. Gardonio, T.C. Sors, and M.J. Brennan. Active vibroacoustic control with multiple local feedback loops. *The Journal of the Acoustical Society of America*, 111(2):908–915, 2002. 93
- W.P. Engels and S.J. Elliott. Optimal centralized and decentralized velocity feedback control on a beam. *Smart Materials and Structures*, 17:025009, 2008. 5

- L. Eriksson, M. Allie, and R. Greiner. The selection and application of an iir adaptive filter for use in active sound attenuation. *Acoustics, Speech and Signal Processing, IEEE Transactions on*, 35(4):433–437, 1987. 2
- D.J. Ewins. *Modal testing: theory, practice and application*. Research Studies Press, Ltd., 2000. 36, 76
- F. Fahy and P. Gardonio. *Sound and structural vibration: radiation, transmission and response*. Academic press, 2007. 25, 93
- G. Ferreres and G. Puyou. Feasibility of hinfy design specifications: an interpolation method. *International Journal of Control*, 78(12):927–936, 2005. 45
- J.S. Freudenberg, C. V. Hollot, R.H. Middleton, and V. Tsochinda. Fundamental design limitations of the general control configuration. *Automatic Control, IEEE Transactions on*, 48(8):1355–1370, 2003a. ISSN 0018-9286. 33
- JS Freudenberg, CV Hollot, and RH Middleton. A tradeoff between disturbance attenuation and stability robustness. In *American Control Conference, 2003. Proceedings of the 2003*, volume 6, pages 4816–4821. IEEE, 2003b. 33, 66
- M. Fu. Interpolation approach to  $h_\infty$  estimation and its interconnection to loop transfer recovery. *Systems & control letters*, 17(1):29–36, 1991. 45
- C.R. Fuller, SD Snyder, CH Hansen, and RJ Silcox. Active control of interior noise in model aircraft fuselages using piezoceramic actuators. *AIAA journal*, 30(11):2613–2617, 1992. 7
- CR Fuller, SJ Elliott, and PA Nelson. *Active Control of Vibration*. Academic Press, 1997. 35, 97, 98
- P. Gardonio. Review of active techniques for aerospace vibro-acoustic control. *Journal of aircraft*, 39(2):206–214, 2002. 4, 7
- P. Gardonio and S.J. Elliott. Modal response of a beam with a sensor-actuator pair for the implementation of velocity feedback control. *Journal of sound and vibration*, 284(1-2):1–22, 2005. 94

- P. Gardonio, E. Bianchi, and SJ Elliott. Smart panel with multiple decentralized units for the control of sound transmission. part i: theoretical predictions. *Journal of sound and vibration*, 274(1):163–192, 2004. 93
- G. Gatti, M.J. Brennan, and P. Gardonio. Active damping of a beam using a physically collocated accelerometer and piezoelectric patch actuator. *Journal of sound and vibration*, 303(3-5):798–813, 2007. 94
- W.K. Gawronski. *Advanced structural dynamics and active control of structures*. Springer Verlag, 2004. 1, 77, 102
- M. Ghandchi Tehrani, R.N.R. Elliott, and J.E. Mottershead. Partial pole placement in structures by the method of receptances: Theory and experiments. *Journal of Sound and Vibration*, 329(24):5017–5035, 2010. 75
- V. Giurgiutiu, CA Rogers, and Z. Chaudhry. Design of displacement-amplified induced-strain actuators for maximum energy output. *Journal of Mechanical Design*, 119:511, 1997. 7
- AE Glazounov, QM Zhang, and C. Kim. Torsional actuator based on mechanically amplified shear piezoelectric response. *Sensors and Actuators A: Physical*, 79(1):22–30, 2000. 2
- CJ Goh and TK Caughey. On the stability problem caused by finite actuator dynamics in the collocated control of large space structures. *International Journal of Control*, 41(3):787–802, 1985. 75
- AJH Goodwin. The design of a resonance changer to overcome excessive axial vibration of propeller shafting. *Institute of Marine Engineers Transactions*, 72:37–63, 1960. 8
- D. Halim and B.S. Cazzolato. A multiple-sensor method for control of structural vibration with spatial objectives. *Journal of sound and vibration*, 296(1):226–242, 2006. 9
- D. Halim, G. Barrault, and B.S. Cazzolato. Active control experiments on a panel structure using a spatially weighted objective method with multiple sensors. *Journal of Sound and Vibration*, 315(1):1–21, 2008. 9

- S.R. Hall and E.F. Prechtl. Preliminary testing of a mach-scaled active rotor blade with a trailing edge servo-flap. In *SPIE Smart Structures and Materials Symposium*, pages 3668–03, 1999. 7
- C.H. Hansen and S.D. Snyder. Active control of noise and vibration. 1997. 3
- W. Heylen, S. Lammens, and P. Sas. *Modal analysis theory and testing*. Katholieke Universteit Leuven, Departement Werktuigkunde, 2006. 25, 54
- C. Hong, P. Gardonio, and S.J. Elliott. Active control of resiliently mounted beams using triangular actuators. *Journal of sound and vibration*, 301(1):297–318, 2007. 94
- J. Hong and D.S. Bernstein. Bode integral constraints, collocation, and spillover in active noise and vibration control. *Control Systems Technology, IEEE Transactions on*, 6(1):111–120, 1998. 5, 76
- M.E. Hoque, T. Mizuno, D. Kishita, M. Takasaki, and Y. Ishino. Development of an active vibration isolation system using linearized zero-power control with weight support springs. *Journal of Vibration and Acoustics*, 132:041006, 2010. 8
- RA Ibrahim and CL Pettit. Uncertainties and dynamic problems of bolted joints and other fasteners. *Journal of sound and Vibration*, 279(3):857–936, 2005. 23
- T. Inoue, A. Takahashi, H. Sano, M. Onishi, and Y. Nakamura. Nv countermeasure technology for a cylinder-on-demand engine-development of active booming noise control system applying adaptive notch filter. *SAE Technical Paper*, pages 01–0411, 2004. 3
- H. Jalali, H. Ahmadian, and J.E. Mottershead. Identification of nonlinear bolted lap-joint parameters by force-state mapping. *International Journal of Solids and Structures*, 44(25):8087–8105, 2007. 23
- J. Jiang and D. Li. Decentralized guaranteed cost static output feedback vibration control for piezoelectric smart structures. *Smart Materials and Structures*, 19:015018, 2010. 4
- S. Johansson, T. Lagö, S. Nordebo, and I. Claesson. Control approaches for active noise control of propeller-induced cabin noise evaluated from data from a dornier

- 328 aircraft. In *Proceedings of International Congress on Sound and Vibration*, pages 1611–1618, Copenhagen, 1999. 2
- FA Johnson and MA Swinbanks. Electromagnetic control of machinery rafts. *Journal of Defence Science*, 1(4):493–497, 1996. 8
- M.E. Johnson, L.P. Nascimento, M. Kasarda, and C.R. Fuller. The effect of actuator and sensor placement on the active control of rotor unbalance. *Journal of vibration and acoustics*, 125(3):365–373, 2003. 5, 79
- J. Kautsky, N.K. Nichols, and P. Van Dooren. Robust pole assignment in linear state feedback. *International Journal of Control*, 41(5):1129–1155, 1985. 75
- S.M. Kuo and D.R. Morgan. *Active noise control systems: algorithms and DSP implementations*, volume 31. Wiley-Interscience, 1996. 3
- GP Liu and S. Daley. Output-model-based predictive control of unstable combustion systems using neural networks. *Control Engineering Practice*, 7(5):591–600, 1999. 57
- GP Liu, GR Duan, and S. Daley. Stable observer-based controller design for robust state-feedback pole assignment. *Proceedings of the Institution of Mechanical Engineers, Part I: Journal of Systems and Control Engineering*, 214(4):313–318, 2000. 28
- GP Liu, R. Dixon, and S. Daley. Design of stable proportional-integral-plus controllers. *International Journal of Control*, 74(16):1581–1587, 2001. 28
- W. Liu and Z. Hou. A new approach to suppress spillover instability in structural vibration control. *Structural Control and Health Monitoring*, 11(1):37–53, 2004. 102
- L. Ljung. Recursive identification algorithms. *Circuits, systems, and signal processing*, 21(1):57–68, 2002. 57
- A. F. Mazoni, A. L. Serpa, and E. G. Nobrega. A decentralized and spatial approach to the robust vibration control of structures. In Prof. Andrzej Bartoszewicz, editor, *Challenges and Paradigms in Applied Robust Control*. InTech, 2011. URL <http://www.intechopen.com/>

- books/challenges-and-paradigms-in-applied-robust-control/  
a-decentralized-andspatial-approach-to-the-robust-vibration-control-of-structure  
9
- D.J. Mead and DJ Meador. *Passive vibration control*. Wiley, 1998. 1
- L. Meirovitch. *Dynamics and control of structures*. Wiley-Interscience, 1990. 1
- S. Merz, N. Kessissoglou, R. Kinns, and S. Marburg. Minimisation of the sound power radiated by a submarine through optimisation of its resonance changer. *Journal of Sound and Vibration*, 329(8):980–993, 2010. 23
- T. Meurers and S.M. Veres. Online iterative design for periodic vibration attenuation. In *Proceedings of Seventh International Congress of Sound and Vibration (ICSV7)*, volume 1, pages 359–366. International Institute of Acoustics and Vibration, 2000. URL <http://eprints.soton.ac.uk/21662/>. 3
- T. Meurers, S.M. Veres, and SJ Elliot. Frequency selective feedback for active noise control. *Control Systems, IEEE*, 22(4):32–41, 2002. 3
- SA Motahari, M. Ghassemieh, and SA Abolmaali. Implementation of shape memory alloy dampers for passive control of structures subjected to seismic excitations. *Journal of Constructional Steel Research*, 63(12):1570–1579, 2007. 1
- J.E. Mottershead, M.G. Tehrani, S. James, and Y.M. Ram. Active vibration suppression by pole-zero placement using measured receptances. *Journal of Sound and Vibration*, 311(3):1391–1408, 2008. 75
- BC Nakra. Vibration control in machines and structures using viscoelastic damping. *Journal of sound and vibration*, 211(3):449–465, 1998. 1
- PA Nelson and SJ Elliott. *Active control of sound*. Academic Pr, 1993. 3, 5
- PA Nelson, ARD Curtis, and SJ Elliott. Quadratic optimisation problems in the active control of free and enclosed sound fields. *Proceedings of the Institute of Acoustics*, 7 (Part 2):45–54, 1985. 3

- Khanh Q. Nguyen. *Higher harmonic control analysis for vibration reduction of helicopter rotor systems*. PhD thesis, University of Maryland, 1994. 7
- D. Nyawako and P. Reynolds. Response-dependent velocity feedback control for mitigation of human-induced floor vibrations. *Smart Materials and Structures*, 18:075002, 2009. 117
- D.S. Nyawako and P. Reynolds. Lqr controller for an in-service floor. In *Dynamics of Civil Structures, Volume 4: Proceedings of the 28th IMAC, A Conference on Structural Dynamics, 2010*, volume 13, pages 227–237. Springer, 2011. 117
- T. Oomen, E. Grassens, F. Hendriks, R. van Herpen, and O. Bosgra. Inferential motion control: Identification and robust control with unmeasured performance variables. In *Decision and Control and European Control Conference, CDC/ECC 2011. Proceedings of the 50th IEEE Conference on*, pages 964–969. IEEE, 2011. 9
- H. Ouyang, MJ Oldfield, and JE Mottershead. Experimental and theoretical studies of a bolted joint excited by a torsional dynamic load. *International journal of mechanical sciences*, 48(12):1447–1455, 2006. 23
- C. Paulitsch, P. Gardonio, and SJ Elliott. Active vibration damping using self-sensing, electrodynamic actuators. *Smart materials and structures*, 15(2):499, 2006a. 25
- C. Paulitsch, P. Gardonio, and S.J. Elliott. Active vibration control using an inertial actuator with internal damping. *The Journal of the Acoustical Society of America*, 119:2131, 2006b. 4
- J.B. Pearson and P.A. Emery. Damping of vibrations, January 24 2003. US Patent App. 10/502,589. 23, 59
- JT Pearson, RM Goodall, and I. Lyndon. Active control of helicopter vibration. *Computing & Control Engineering Journal*, 5(6):277–284, 1994. 7
- B. Peeters, G. Lowet, H. Van der Auweraer, and J. Leuridan. A new procedure for modal parameter estimation. *Sound and Vibration*, 38(1):24–29, 2004. 23

- I.R. Petersen. Robust  $h_\infty$  control of an uncertain system via a strict bounded real output feedback controller. *Optimal Control Applications and Methods*, 30(3):247–266, 2009. 28
- M. Petyt. *Introduction to finite element vibration analysis*. Cambridge Univ Pr, 2010. 42
- S. Pope and S. Daley. Redistribution of the energy in a vibration isolation system under the action of discrete frequency active control. In *Proceedings of Active 2009*, pages 149–159, 20-22 August 2009. 76
- J.T. Post and R.J. Silcox. Active control of the forced response of a finite beam. *Noise Control Engineering Journal*, 1:197–202, 1990. 5, 76
- A. Preumont. *Vibration control of active structures: an introduction*, volume 96. Springer, 2002. 1, 24
- M.D. Rao. Recent applications of viscoelastic damping for noise control in automobiles and commercial airplanes. *Journal of Sound and Vibration*, 262(3):457–474, 2003. 1
- MZ Ren, K. Seto, and F. Doi. Feedback structure-borne sound control of a flexible plate with an electromagnetic actuator: the phase lag problem. *Journal of sound and vibration*, 205(1):57–80, 1997. 25
- J. Rohlfig, P. Gardonio, and SJ Elliott. Base impedance of velocity feedback control units with proof-mass electrodynamic actuators. *Journal of Sound and Vibration*, 330(20):4661–4675, 2011a. 25
- J. Rohlfig, P. Gardonio, and DJ Thompson. Comparison of decentralized velocity feedback control for thin homogeneous and stiff sandwich panels using electrodynamic proof-mass actuators. *Journal of Sound and Vibration*, 330(5):843–867, 2011b. 93
- J. Shaw, N. Albion, E.J. Hanker, and R.S. Teal. Higher harmonic control: wind tunnel demonstration of fully effective vibratory hub force suppression. *Journal of the American Helicopter Society*, 34(1):14–25, 1989. 7

- MA Simpson, TM Luong, CR Fuller, and JD Jones. Full-scale demonstration tests of cabin noise reduction using active vibration control. *Journal of Aircraft*, 28(3): 208–215, 1991. 7
- R.E. Skelton, T. Iwasaki, and D.E. Grigoriadis. *A unified algebraic approach to control design*. CRC, 1997. 9
- S Skogestad and I Postlethwaite. *Multivariable Feedback Control. Analysis and Design*. John Wiley & Sons, 2005. 37, 108
- TT Soong. State-of-the-art review:: Active structural control in civil engineering. *Engineering Structures*, 10(2):74–84, 1988. 1
- J. Stoustrup and H. Niemann. Starting up unstable multivariable controllers safely. In *Decision and Control, 1997., Proceedings of the 36th IEEE Conference on*, volume 2, pages 1437–1438. IEEE, 1997. 29
- MO Tokhi and MA Hossain. A unified adaptive active control mechanism for noise cancellation and vibration suppression. *Mechanical systems and signal processing*, 10(6):667–682, 1996. 1
- U. Ubaid, S. Daley, and S. Pope. Broadband design of remotely located vibration control systems: A stable solution for non-minimum phase dynamics. In *INTER-NOISE and NOISE-CON Congress and Conference Proceedings*, volume 2011, pages 835–840. Institute of Noise Control Engineering, 2011a. 13
- U. Ubaid, S. Daley, and S. Pope. Design of remotely located stable vibration controllers for non-minimum phase systems. In *14th Asia Pacific Vibration Conference*, Hong Kong, December 5-8 2011b. 13
- U. Ubaid, S. Daley, S. Pope, and I. Zazas. Experimental validation of a geometric method for the design of stable and broadband vibration controllers using a propeller blade test rig. In *Control (CONTROL), 2012 UKACC International Conference on*, pages 369–374. IEEE, 2012. 14, 23
- S.R. Viswamurthy and R. Ganguli. An optimization approach to vibration reduction in helicopter rotors with multiple active trailing edge flaps. *Aerospace science and technology*, 8(3):185–194, 2004. 1

- 
- J. Wang and S. Daley. A geometric approach to the optimal design of remotely located broadband vibration control systems. In *Proceedings of the 14th International Congress on Sound and Vibration*, pages 9–12, 2007a. 19, 24
- J. Wang and S. Daley. A geometric design approach to the broadband control of remotely located vibration. In *Control & Automation, 2007. MED'07. Mediterranean Conference on*, pages 1–6. IEEE, 2007b. 19
- J. Wang and S. Daley. Broad band controller design for remote vibration using a geometric approach. *Journal of Sound and Vibration*, 329(19):3888–3897, 2010. ISSN 0022-460X. 11, 39, 40, 65
- J. Wang, N. Min, T. Zhang, and L. Ma. A new parameterization of all stabilizing controllers in a siso setup. In *Control Conference (CCC), 2010 29th Chinese*, pages 3441–3446. IEEE, 2010. 31
- B. Widrow and S.D. Stearns. Adaptive signal processing. *Englewood Cliffs, NJ, Prentice-Hall, Inc., 1985, 491 p.*, 1, 1985. 2
- M. Zilletti, S.J. Elliott, and P. Gardonio. Self-tuning control systems of decentralised velocity feedback. *Journal of Sound and Vibration*, 329(14):2738–2750, 2010. 94
- M. Zilletti, S.J. Elliott, and E. Rustighi. Optimisation of dynamic vibration absorbers to minimise kinetic energy and maximise internal power dissipation. *Journal of Sound and Vibration*, 331(18):4093–4100, 2012. 4